ADAPTISPECT: A PRECLINICAL IMAGING SYSTEM

by

Cécile Chaix

A Dissertation Submitted to the Faculty of the

COLLEGE OF OPTICAL SCIENCES

In Partial Fulfillment of the Requirements
For the Degree of

DOCTOR OF PHILOSOPHY

In the Graduate College

THE UNIVERSITY OF ARIZONA

2015

THE UNIVERSITY OF ARIZONA
GRADUATE COLLEGE

As members of the Dissertation Committee, we certify that we have read the dissertation prepared by Cécile Chaix
entitled AdaptiSPECT: a preclinical imaging system
and recommend that it be accepted as fulfilling the dissertation requirement for the Degree of Doctor of Philosophy.

Date: November 13th 2015
Dr. Lars R. Furenlid

Date: November 13th 2015
Dr. Matthew A. Kupinski

Date: November 13th 2015
Dr. Arthur F. Gmitro

Date: November 13th 2015
Dr. Harrison H. Barrett

Final approval and acceptance of this dissertation is contingent upon the candidate's submission of the final copies of the dissertation to the Graduate College.
I hereby certify that I have read this dissertation prepared under my direction and recommend that it be accepted as fulfilling the dissertation requirement.

Date: November 13th 2015
Dissertation Director: Dr. Lars R. Furenlid

STATEMENT BY AUTHOR

This dissertation has been submitted in partial fulfillment of requirements for an advanced degree at the University of Arizona and is deposited in the University Library to be made available to borrowers under rules of the Library.

Brief quotations from this dissertation are allowable without special permission, provided that accurate acknowledgment of source is made. Requests for permission for extended quotation from or reproduction of this manuscript in whole or in part may be granted by the head of the major department or the Dean of the Graduate College when in his or her judgment the proposed use of the material is in the interests of scholarship. In all other instances, however, permission must be obtained from the author.

SIGNED: Cécile Chaix

ACKNOWLEDGEMENTS

I would like to thank my parents, Florence and Gérald Chaix, for encouraging all their children to pursue higher education and for never doubting that any of us could become scientists and engineers.

I would like to thank my advisor Dr. Lars R. Furenlid for his guidance throughout the entire development process of AdaptiSPECT, and Dr. Harrison H. Barrett for first inviting me to join the Center for Gamma-Ray Imaging and constantly pushing me to improve my writing and presentation skills. I would also like to thank Dr. Matthew A. Kupinski for his enthusiasm on seeing AdaptiSPECT completed and for the many insightful discussions we had. I am also grateful to Dr. Arthur F. Gmitro for serving on my committee and for his input in improving this manuscript.

I would like to thank Dr. Eric Clarkson for his help with all the mathematical aspects of this dissertation, Dr. Luca Caucci for his help with the computing aspects of this work, and Dr. Roel Van Holen and Dr. Jared Moore for entrusting me with AdaptiSPECT when they left CGRI. I would also like to thank Dr. Brian Miller, Dr. Heather Durko, and Dr. Stephen Moore for showing me around the labs in the first few years.

This project could not have been completed without the exquisite machining work performed by Larry Acedo, Russell Cole and Ryan Willwater from the University Research Instrumentation Center at the University of Arizona. They spent many patient hours making the individual parts of the system and providing helpful feedback on the design.

I am also grateful for the two undergraduate students that helped integrate the system, Matt Kosminder, who soldered most of the acquisition electronics over a semester, and Stephen Kovalsky, who worked at CGRI for five semester and was an immense help in cabling the system, testing the electronics, and finishing lots of small details in the system integration.

I would like to thank our program administrators, Merry Warner, Liz Hague, Gail Varin, and Mark Rodriguez, for their valuable help in filling out forms and placing orders.

I would like to thank my labmates Esen, Vaibhav, Helen, Joseph, Joy, Xin, Ling, and Maria for all the good times, as well as the many friends I have made in Tucson.

Last but not least, I am thankful for my husband David Carlson, who had to hear me talk constantly about AdaptiSPECT for years and carefully proofread this dissertation.

This work was supported by the NIH/NIBIB grant P41-EB002035 “The Center for Gamma-Ray Imaging.”

DEDICATION

I dedicate this work to my great-grand-mother, Dr. Soueix.

Nous fuirons le repos nous fuirons le sommeil
Nous prendrons de vitesse l'aube et le printemps
Et nous préparerons des jours et des saisons
À la mesure de nos rêves.
Paul Éluard — Le Visage de la Paix (1951)

TABLE OF CONTENTS

TABLE OF CONTENTS – *Continued*

TABLE OF CONTENTS – *Continued*

LIST OF FIGURES

LIST OF FIGURES – *Continued*

LIST OF FIGURES – *Continued*

LIST OF FIGURES – *Continued*

LIST OF FIGURES – *Continued*

LIST OF FIGURES – *Continued*

LIST OF FIGURES – *Continued*

LIST OF FIGURES – *Continued*

LIST OF FIGURES – *Continued*

LIST OF FIGURES – *Continued*

LIST OF TABLES

ABSTRACT

This dissertation addresses the design, development, calibration and performance evaluation of a pre-clinical imaging system called AdaptiSPECT. Single-Photon Emission Computed Tomography (SPECT) systems are powerful tools for multiple applications in small-animal research, ranging from drug discovery to fundamental biology. Traditionally, pinhole SPECT systems are designed with fixed imaging characteristics in terms of sensitivity, resolution and size of the field of view, that are dictated by the hardware configuration of the system. The SPECT system described in this dissertation can change its hardware configuration in response to the subject data it is acquiring in order to improve the imaging performance.

We employed 16 modular gamma-ray detectors, each of which consists of a NaI:Tl scintillation crystal, a fused silica lightguide, and an array of 9 PMTs. The camera is designed to work with maximum-likelihood position-estimation methods. These detectors are arranged into 2 rings of 8 detectors around an adjustable pinhole aperture. The aperture itself comprises three cylinders of different diameters, each with pinholes of different diameters. The three aperture cylinders are stacked together along the imager axis, and selection of the appropriate ring of pinholes is carried out by translating the entire aperture assembly. In addition, some sections of the aperture are fitted with shutters to open or close additional pinholes that increase sensitivity.

We reviewed the method used to calibrate AdaptiSPECT, and proposed a new interpolation scheme specific to adaptive SPECT imaging systems where the detectors can move to multiple locations, that yields system matrices for any configuration employed during adaptive imaging.

We evaluated the performances of AdaptiSPECT for various configurations. The magnification of the system ranges from 1.2 to 11.1. The corresponding resolution

ranges from 3.2 mm to 0.6 mm, and the corresponding transaxial field-of-view ranges from 84 mm to 10 mm. The sensitivity of the system varies from 220 cps/MBq to 340 cps/MBq for various configurations. Imaging of a mouse injected with a bone radiotracer revealed the finer structures that can be acquired at higher magnifications, and illustrated the ability to conveniently image with a variety of magnifications during the same study.

In summary, we have brought the concept of an adaptive SPECT imaging system as it was originally described by Barrett *et al.* [17] to life. We have engineered a system that can switch configurations with speed, precision, and repeatability suitable to carry out adaptive imaging studies on small animals, thus opening the door to a new research and medical imaging paradigm in which the imager hardware is adjusted on the fly to maximize task-performance for a specific patient, not, as currently, an ensemble of patients.

CHAPTER 1

Introduction

This dissertation addresses the design, development, and performance evaluation of a pre-clinical imaging system for small animals called AdaptiSPECT. *In vivo* imaging of small animals is a key component of biomedical research as it provides quantified knowledge of biological processes at the organ, tissue, cell, or even molecular level [88]. Of all small animals, rodents such as rats and mice have become the most common objects of study because they are relatively economical, can reproduce quickly, which enables studies over multiple generations, and they can be easily integrated into human disease models [171]. Imaging of small animals is currently carried out with a variety of technologies including X-ray CT, MRI, ultra-sound, optical imaging such as fluorescence and bioluminescence, and emission tomography, the latter which comprises both positron emission tomography (PET) and single photon emission tomography (SPECT). For all these modalities, imaging can be performed using clinical systems that have been adapted for the small animal under study or with dedicated imaging systems. The design of such a system that implements single-photon emission tomography is the purpose of this work.

1.1 Brief history of gamma-ray imaging

1.1.1 Discovery of x-rays and gamma-rays

The medical-imaging field is considered to have started at the end of the nineteenth century with the discovery of invisible radiation by Wilhelm Röntgen in 1895 [167]. This discovery is usually associated with the image of his wife's hand, shown in Figure 1.1. Despite the low quality of this image by today's standards, it is significant for being the first demonstration that it is possible to image an invisible object (the

bones in a hand) using invisible radiation. Röntgen was awarded the Nobel Prize in Physics for this discovery in 1901.

Only a few months after the discovery of X-rays Henry Becquerel accidentally discovered radioactive radiation in uranium in 1896 when he was investigating whether luminescent materials were also emitting X-rays. The first image Becquerel took using uranium is shown in Figure 1.1. During the years following his discovery of uranium radiation, Becquerel, along with Marie and Pierre Curie discovered other radioactive materials, namely radium, polonium and thorium. They shared the Nobel Prize in Physics in 1903.

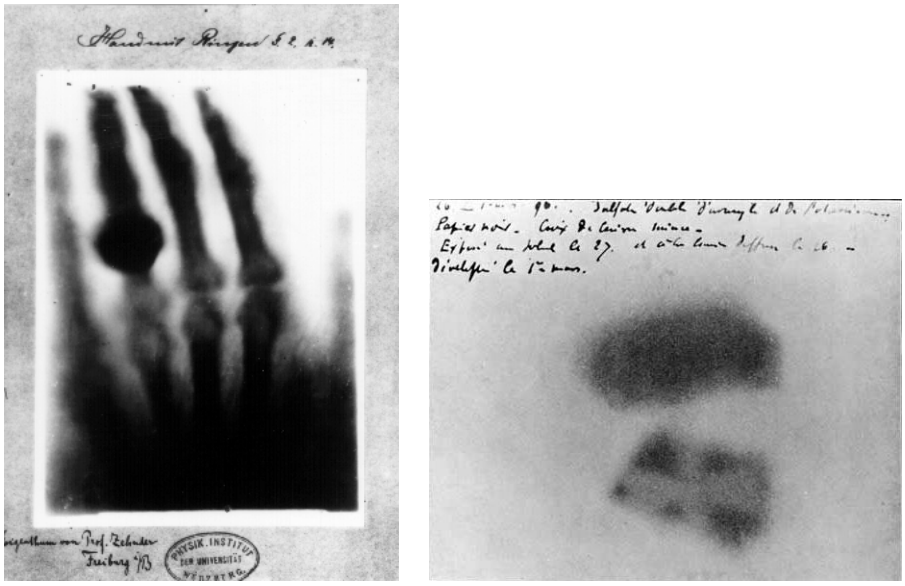

(a) (b)

Figure 1.1: (a) Reproduction of the first x-ray image of Röntgen's wife's hand. (b) Shadow image of a Maltese cross formed by radioactive decay of uranium, taken by Becquerel.

Around the same time, two other physicists got interested in the study of radioactive decay: Ernst Rutherford and Paul Villard. Ernst Rutherford discovered in 1899 that radioactive decay produced two different types of emission with different penetration abilities. He called the weakest of these radiations *alpha* particles and the strongest of these radiations *beta* emissions. A few years later, in 1903, Paul Villard discovered a third type of radiation that had much greater penetration

ability than either alpha or beta particles, and called these rays *gamma* rays. Ernst Rutherford was awarded the Nobel Prize in Chemistry in 1908.

1.1.2 The tracer principle

The tracer principle was developed in the early 1900s by George de Hevesy. De Hevesy had joined Rutherford's group in England in 1911, where he was tasked with separating so-called "radium D" from lead. After failing at this task and concluding that the radioactive material could not be separated from the lead, which was in fact ^{210}Pb, de Hevesy decided to use this heavy lead compound to track the distribution of non-radioactive lead in plants using a simple Geiger counter [49]. He was awarded the Nobel Prize in Chemistry for his work in 1943.

Using a radioactive compound that participates in the biological process in the same way as a non-radioactive compound is the foundation of emission tomography. In fact, as de Hevesy's early work shows, the tracer principle offers two powerful properties: (1) very small quantities of the tracer can be detected and quantified, and (2) measuring the distribution of the radioactive compound can be done in a non-invasive way. George de Hevesy had only access to natural tracers, such as radioactive lead, but today radioactive tracers can be synthesized and can be designed to target very specific processes in the body. One of the most popular tracers for example, ^{18}F-FDG, is a molecule designed to measure glucose transport. It comprises two components: (1) fluorodeoxyglucose (FDG), an analog to glucose, and (2) a fluorine-18 label (^{18}F) that emits gamma-rays. ^{18}F-FDG will enter a cell the same way glucose does, but as it is being metabolized, a radioactive intermediate remains trapped in the cell, thus enabling the measurement of the cell's transport rate for glucose (and thereby inferred metabolic rate). Using radiotracers in imaging enables the acquisition of *functional* information, such as metabolic rate, whereas imaging techniques that do not use a tracer that targets a biological process usually provide *structural* information. Although some modalities, such as MR spectroscopy for instance, allow access to functional information without the use of a radiotracer.

1.2 Pre-clinical SPECT imaging

1.2.1 Formation of a tomographic image

The production of an emission tomography image for an imaging task, as conventionally performed, can be separated into five steps [167]:

1. A radioactive tracer, called a radiotracer, or a radiopharmaceutical when used in humans, is designed and produced. The tracer is specific to the imaging task in question.

2. The tracer is introduced into the subject under study. Usually this is done by injection of the radiopharmaceutical into the blood stream or peritoneal cavity, though they can also be inhaled.

3. Data acquisition begins and is carried out using a tomographic imaging system (PET or SPECT).

4. After acquisition of the data, it is reconstructed to provide a 3D-tomographic image from the set of 2D planar projections acquired.

5. The tomographic image is analyzed to answer the imaging task.

In the case of SPECT, tomographic imaging systems usually consist of a detector or a set of detectors, matching imaging apertures, and a rotating gantry. The features of interest in small animals are typically mm-scale in size and thus the imaging aperture is usually a pinhole or a set of pinholes, as they allow for high magnification. We will review the imaging properties of pinhole SPECT in Section 1.3.

1.2.2 Key strength of SPECT for small-animal imaging

In a recent paper titled "Small-Animal SPECT and its place in the matrix of molecular imaging technology", Meikle *et al.* [102] extensively reviewed the advantages of SPECT for small-animal research with respect to other imaging modalities. Their findings are summarized below.

The key property of gamma-ray imaging techniques for pre-clinical research (PET and SPECT) is their high sensitivity, which is several orders of magnitude higher than other techniques such as MRI. This allows for imaging and quantifying very small concentrations of radiotracers. PET has much higher sensitivity than SPECT due to its "electronic collimation", but SPECT has some unique properties that make it a strong research tool. The main advantage of SPECT relative to PET is that the single-photon-emitting radioisotopes available have very long half-lives, which allows for imaging slow biological processes. PET on the other hand is better suited for fast kinetic processes. The main isotopes used for SPECT imaging, and their respective half-lives ranging from a few hours to several days, are listed in Table 1.1. Use of radionuclides with long half-lives enables the labeling of large molecules that diffuse slowly, such as peptides, antibodies, and hormones. The uptake and clearance times of these molecules can range from several hours to multiple days. With SPECT, observing processes over several days, such as cell division or stem-cell migration is possible *in vivo*. Another advantage of these nuclides is that they are easy to use as labeling agents (in particular iodine and technetium), which facilitates the creation of imaging tracers in comparison to the generally more complex process of creating synthetic molecules for PET. In both techniques it is possible to create very specific targeting agents.

In addition to its ability to image longer biological processes, SPECT also has the advantage of being able to image multiple isotopes that emit different gamma rays energy simultaneously. This allows for the study of multiple related biological processes at the same time, such as blood flow and receptor binding.

These characteristics have made SPECT systems a powerful tool for multiple applications in small-animal research, ranging from drug discovery to cardiovascular imaging, to study of inflammation. For example, pre-clinical SPECT has been used for cardiovascular imaging [48, 69, 97], imaging of gene expression [9], oncology [55, 67], bone metabolism [166], neuroimaging [7, 29], and inflammation [27].

Radionuclide	Half-life	Energy (keV)
^{99m}Tc	6.02 h	140
^{125}I	59 days	20-35
^{123}I	13.3 h	159
^{131}I	8.2 days	364
^{111}In	2.8 days	171,245

Table 1.1: Commonly used single photon emitting radionuclides, and their characteristics.

1.3 Properties of pre-clinical SPECT imaging systems

Small-animal SPECT systems comprise detectors, apertures, and reconstruction algorithms [19]. Most SPECT systems for small-animal imaging use pinholes as apertures. Systems can be clinical systems that have been converted to preclinical applications (for example U-SPECT-I [26]), or dedicated systems (for example FastSPECT II [66]. They can comprise one detector coupled to one or more pinholes with a rotating mechanism for angular sampling (either the object is rotated or the detector and pinholes are rotated), or multiple detectors that provide enough angular sampling of the field-of-view to not need any rotating mechanism. In that case, the pinhole aperture can have one pinhole per detector or multiple pinholes per detector. Systems comprising multiple detectors are usually more expensive than ones with a single detector, but they have the advantage of enabling temporal studies by acquiring views from multiple angles simultaneously.

1.3.1 Desirable properties of preclinical SPECT systems

The three properties that describe the performance of a preclinical SPECT system are resolution, sensitivity, and size of the field of view. The resolution determines the size of the features that are distinguishable in a reconstructed image. For small-animals, the features of interest are typically a few hundred microns in dimension for a mouse to a few millimeters for a rat. The sensitivity of the system determines the minimum concentration of radioactive material one is able to detect. The higher the sensitivity, the easier it will be to image features that do not uptake much activity.

Finally, the size of the field of view determines the volume of the object you can image at once. Some SPECT systems with very small fields-of-view have the ability to scan the object around. This increases the size of the field of view at the cost of longer acquisition times and loss of ability to do timing experiments. Another important parameter is the uniformity of the sensitivity across the field of view. A uniform sensitivity produces better results when using statistical reconstruction algorithms.

1.3.2 Design trade-offs

Designing a pinhole SPECT system involves choosing an appropriate tradeoff between resolution, sensitivity, and size of the field of view since these three properties vary in different directions with the adjustable parameters of pinhole SPECT systems. The system's intended task dictates what tradeoffs are appropriate. For example, the requirements in terms of size of the field of view will be different for cardiovascular imaging and whole-body skeletal studies. In Figure 1.2, we describe the parameters that have to be set during the design phase of a preclinical SPECT system: the pinhole-diameter d, the distance from the pinhole to the center of the field of view a, and the distance from the detector to the center of the field of view L. The size of the detector also influences the size of the possible field of view.

The intrinsic resolution of the detector will also determine the resolution achievable with pinhole SPECT. To resolve small features, one approach is to use SPECT detectors with very-high intrinsic resolution (such as strip detectors) and then use a design with low magnification to see small features. Alternatively, a detector with low intrinsic resolution can be used (such as NaI:Tl crystals with conventional PMTs) in a high-magnification configuration. Other parameters, such as the shape of the pinholes also influence the characteristics of the system, but for the sake of simplicity, these are not discussed here.

Using these parameters, the system sensitivity S is proportional to:

$$S \propto \frac{d^2}{a^2}. \tag{1.1}$$

The size of the field of view is proportional to:

$$D_{FOV} \propto \frac{a}{L}. \tag{1.2}$$

And finally, under the assumption that the size of the pinhole is smaller than the intrinsic resolution of the detector, a geometric resolution is approximately given by:

$$R = \sqrt{\left(2d\frac{a+L}{a}\right)^2 + R_i^2}, \tag{1.3}$$

where R_i is the intrinsic resolution of the detector.

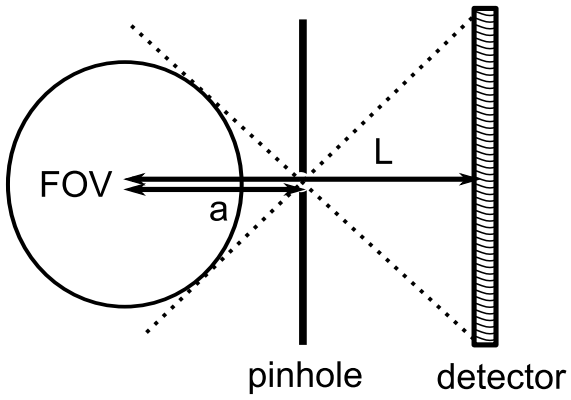

Figure 1.2: Geometry of a simple pinhole SPECT imaging system. The parameters that influence the properties of the system are the size of the pinhole d, the distance of the pinhole to the center of the field-of-view a, and the distance from the detector to the center of the field-of-view L.

To illustrate the tradeoffs between sensitivity, resolution, and field of view, we simulated the performances of SPECT systems using the equations above for various parameters. Three possible values for a, the distance from the pinhole to the center of the field of view, are used: 30mm, 50mm, and 80mm. Likewise, two possible values of L, the distance from the detector to the center of the field of view, are chosen: 160mm and 315mm. The pinhole size d is then varied from 0.1mm to 1.5mm. The results of the simulations are shown in Figure 1.3, where the sensitivity of each configuration is plotted versus its resolution. At each point, the size of the dot is

proportional to the size of the field of view. The simulations show that smaller pinholes lead to better resolution but have smaller sensitivities. Furthermore, bringing the pinhole closer to the object increases the sensitivity but reduces the size of the field of view. Moving the detector farther away from the object also reduces the size of the field of view, but leads to an increase in image resolution.

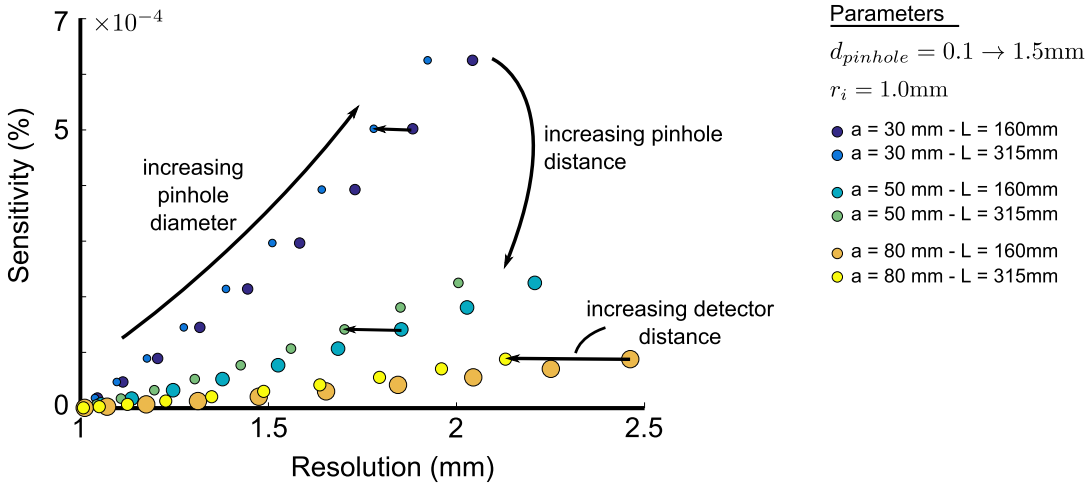

Figure 1.3: Scatter plot of pinhole SPECT properties for various parameters. The sensitivity is plotted versus the resolution of each system with the size of the dot being proportional to the size of the field of view. Three key trade-offs are observed: 1) smaller pinholes lead to better resolution but lower the sensitivity, 2) bringing the pinhole closer to the object increases the sensitivity but reduces the field-of-view, and 3) moving the detector farther away from the object increases the resolution but reduces the field of view.

1.3.3 Brief survey of current pre-clinical imaging systems

To evaluate the current state of the art, we performed a survey of preclinical SPECT systems and compared them to each other. The list we compiled is an update to the list created by Jacob Hesterman [75] and later modified by Benjamin McDonald at Vanderbilt University [101]. We have separated the systems into commercial and non-commercial systems and have also counted only the systems with multiple pinholes as they are more relevant to this work. The complete list with detector

description, system description, and performances can be found in Table 1.2 for non-commercial systems and Table 1.3 for commercial systems. We have also plotted the system performances in the same way as in Figure 1.3 while discussing trade-offs for system design. The performance of each system is shown in Figure 1.4 with sensitivity plotted versus resolution and a bubble size proportional to the size of the field of view as before.

When reviewing the literature, we noted a few things: (1) there is no standard in the type of detectors used, nor in the number of detectors or pinholes, and (2) there is also no standard way of reporting system performance. While some papers report theoretical values, others report measured values. Some report average sensitivities over the field of view, while others report maximum sensitivities. Additionally, some report a size of the field of view that can be achieved with only one acquisition whereas others report sizes which require the animal under study to be moved multiple times. A recent paper by Deleye *et al.* [52] tried to address this question by independently measuring the system performance of various commercial systems. The metrics they measured were spatial resolution, image uniformity, point-source sensitivity, and contrast recovery. Despite this non-uniform way of reporting performances, the characteristics of non-commercial systems are quite similar, with sensitivities varying from 50 cps/MBq to 150 cps/MBq for isotropic resolutions around 1mm, and from 250 cps/MBq to 500 cps/MBq for resolutions around 2mm.

References	System Description	FOV (mm)	Res. (mm)	Sens. (cps/MBq)
Kastis *et al*, 1998 [85]	FastSPECT I: 24 1.5mm pinholes, 24 NaI(Tl) modcams (4PMTs)	20	2.0	359
Meikle *et al*, 2003 [105]	CoALA-SPECT: 4 0.5mm pinholes, 4 NaI(Tl) PSPMT cameras	50	1	146
Schramm *et al*, 2003 [142]	Multiplexing, 1 clinical camera			
	7 1.5mm pinholes	50	2.0	330
	10 1.5mm pinholes	50	2.0	490
	14 1.5mm pinholes	50	2.1	707
Furenlid *et al*, 2004 [66]	FastSPECT II: 16 1.0mm pinholes 16 NaI(Tl) ModCams	40	2.2	243
Beekman *et al*, 2005 [26]	U-SPECT I: 75 0.6mm pinholes, 3 clinical cameras, no multiplexing	10.5	0.5	2200
Kim *et al*, 2006 [89]	SemiSPECT: 8 0.5mm pinholes, 8 27mm^3 CZT detectors	32	1.45	0.5e-4
Hesterman *et al*, 2007 [78]	M^{3}R: 4 ModCams			
	1 0.5mm-pinhole per detector	16	1.3	50
	4 0.5mm-pinholes per detector	16	-	159
	1 1mm-pinhole per detector	16	1.18	111
	4 1mm-pinholes per detector	16	-	315
Accorsi *et al*, 2007 [3]	MediSPECT 1 CdTe detector - varying dist. coded aperture or pinholes			
	0.4mm pinhole, 0.9 mag.	32	2.1	-
Meng *et al*, 2009 [108]	CsI(Tl) crystal, DM tube with EMCCD			
	3 apertures : 25 pinholes 200μm	20	-	150
	36 pinholes 150μm	20	0.2	110
	25 pinholes 300μm	20	-	180
Cai *et al*, 2010 [31]	ERPC detectors (2 or 4) [106] 9 pinholes/detector (200-400μm) multiple angular sampling	20	0.5	-
Miller *et al* 2011 [114]	FastSPECT III : 20 iQID detectors [115]	-		
	ap. 1: 20 pinholes 250μm	15	0.33	-
	ap. 2: 20 pinholes 500μm	15	0.65	-
	ap. 3: 20 pinholes 1mm	15	1	-
Havelin *et al*, 2013 [72]	Synthetic collimation 46 pinholes of 1mm diameter 1 iQID detector	25.4	1.6	-

Table 1.2: Survey of non-comercial small-animal SPECT systems using multiple pinholes

References	System Description	FOV (mm)	Res. (mm)	Sens. (cps/MBq)
Schramm	NanoSPECT			
et al, 2007 [141, 143]	4 rotating NaI(Tl) detectors			
	7 apertures, 9-16 pinholes/det.			
	Mouse high sensitivity	30	1.4	2098
	Mouse standard	30	1.0	1200
	Mouse high resolution	30	0.7	723
	Mouse UHR	20	0.4	412
	Rat standard	60	2.5	1267
	Rat high resolution	60	2.0	952
	Rat UHR	60	1.5	599
GM-Ideas	X-SPECT			
2007 [51]	2 rotating NaI detectors			
	4 1mm-pinholes per detector	22	0.6	620
van der Have	U-SPECT-II : 75 pinholes			
et al,2009 [157]	aperture 1: 0.35mm pinholes	12	0.35	700
	aperture 2: 0.6mm pinholes	12	0.45	1800
	aperture 3: 1mm pinholes	27	0.8	900

Table 1.3: Survey of comercial small-animal SPECT systems using multiple pinholes

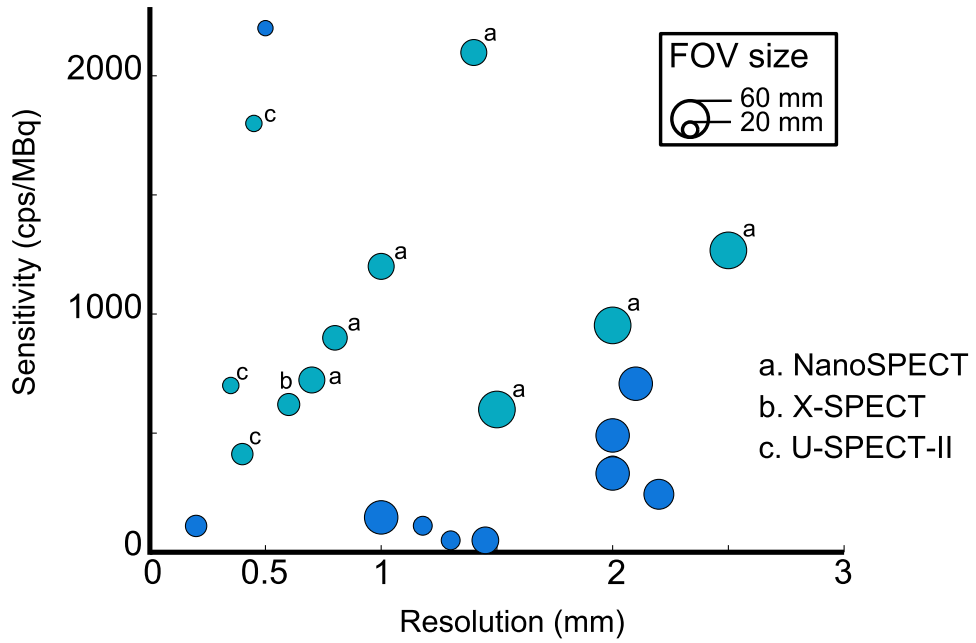

(a)

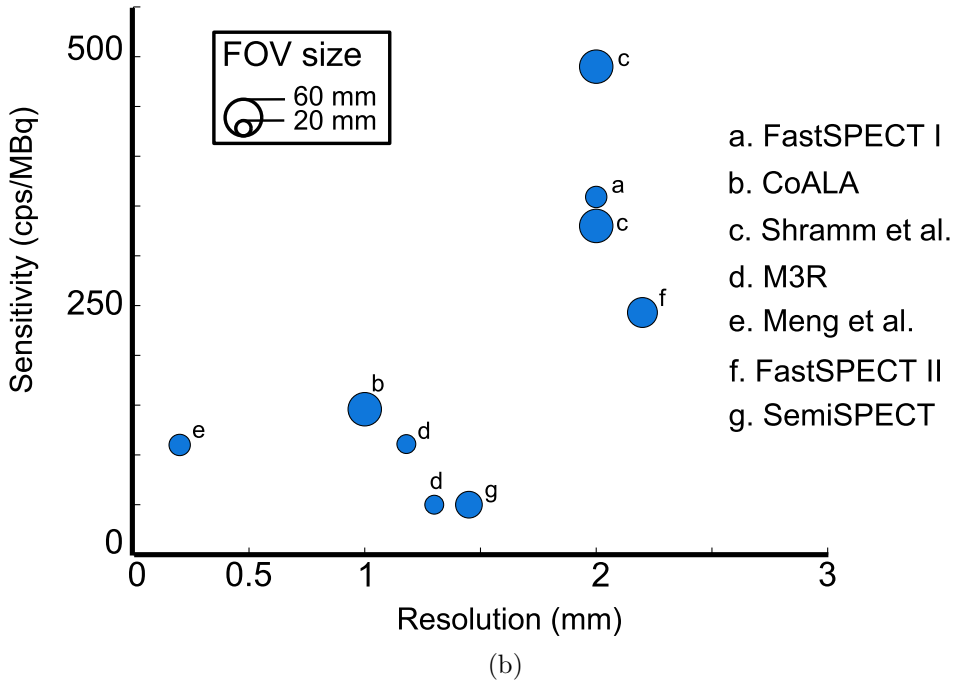

(b)

Figure 1.4: (a) Scatter plot of system performances of commercial (grey) and non-commercial (blue) systems. (b) More detailed view of non commercial SPECT imaging systems.

1.4 Objective assessment of image quality

While we have so far discussed system performances only through three values that can be measured (sensitivity, resolution, and size of the field of view), there is another approach to assessing the performance of a system that consists of quantitatively evaluating how good a system is at performing a specific task. The argument for this approach is that it does not matter if the system has exquisite resolution and sensitivity if it cannot perform the task it was designed for. The most common tasks for SPECT can be separated into two categories: detection of lesions and estimation of parameters (size, activity uptake, etc.). Numerical observers have been developed to test the performance of a particular systems for various tasks. A review of this framework is provided in references [13–15, 33].

Various efforts have been made to include numerical observers into the design of SPECT systems and collimators. In 1985, Wagner and Brown [165] derived the ideal-observer signal-to-noise ratio for various imaging modalities, including SPECT. Optimization of the collimation design can then be done by computing the SNR for the specific task. Based on this approach, Myers *et al.* investigated the optimal pinhole diameter for both a detection task and a Rayleigh task, using both the Hotelling observer and the non-prewhitening matched-filter observer [129]. More recently, Meng and Clinthorne [107] used the Cramér-Rao bound to optimize a multiple-pinhole collimator. Vunckx *et al.* [162] also used a method based on the Fisher Information Matrix to optimize a single pinhole and a multiple-pinhole collimator for use on small-animal SPECT.

1.5 Adaptive imaging

In previous sections, we have stated that the design and optimization of a SPECT system depends on the imaging task to be performed as well as on the properties of the chosen detectors. The small-animal imaging systems we reviewed generally approach the design problem of optimizing for a task in three different ways. Some systems are designed to perform well at one specific anatomical application, such

as FastSPECT III, which is strictly a mouse-brain imager. On the other hand, some are designed with multiple apertures that can be swapped as needed, such as FastSPECT II or the commercial U-SPECT system. The third, more common, approach uses a design methodology that is more generic and has the ability to cover various tasks without necessarily being optimal for any task or any specific imaging subject.

To address this optimization problem, SPECT systems that can change their configuration to accommodate various tasks and objects have been proposed. In particular, these systems should have the capacity to change their configuration autonomously during an acquisition. The development of such an adaptive SPECT system for small-animal imaging is the purpose of this dissertation. Various systems and adaptation schemes have already been proposed. Barrett *et al.* first introduced the concept of an initial scout acquisition and then adapting the hardware for optimized task performance on a particular subject [17]. This approach drew on the initial work of by Hesterman *et al.* who investigated the advantage of simultaneous acquisition with multiple configurations with the M^3R system [77, 78]. A second test-bed system was developed by Freed *et al.* who demonstrated a prototype adaptive SPECT system with one detector, a ladder with four pinhole choices, and stages to independently control the pinhole-to-object and pinhole-to-detector distances [62]. This system was the first to have the potential for fully autonomous adaptation. M^3R and the Adaptive Prototype share the same type of detectors as AdaptiSPECT. A few years ago, the concept of adaptive imaging was also carried out to X-ray imaging when Moore *et al.* built an adaptive X-ray CT system for preclinical imaging [125, 126]. More recently, Durko *et al.* built an adaptive anamorphic SPECT system with crossed-slit collimation [57, 58]. Metzler *et al.* [127] have developed an imaging system with dual resolution for mice imaging. Another approach to adaptive SPECT, described by Li and Meng [94], consists of optimizing the trajectory of a non-stationary system by adjusting the time spent at different acquisition angles.

1.6 This work

The imaging system described in this dissertation, AdaptiSPECT, can be considered an adaptive version of FastSPECT II and therefore has many similarities. Both systems comprise 16 gamma-ray cameras arranged into two rings of 8 and each adopts the single-pinhole-per-detector approach for the default imaging configuration. The fundamental advance in the new system lies in the adaptive functionality of AdaptiSPECT. In AdaptiSPECT, the distance from the detector to the center of the field of view can be adjusted for each detector, the size and number of the pinholes illuminating each camera can be changed, and the distance from the pinholes to the center of the field of view can also be adjusted.

The remainder of this dissertation will present the details of the design and fabrication of AdaptiSPECT. Chapter 2 describes the detectors used on AdaptiSPECT. Chapter 3 is dedicated to the design and fabrication of the adaptive imaging apertures. Chapter 4 describes the integration of the system as well as the controllers designed and manufactured to enable autonomous adaptation. Chapter 5 reviews the calibration technique developed to calibrate AdaptiSPECT. Chapter 6 evaluates the performance of the system and Chapter 7 introduces different schemes for autonomous adaptation.

CHAPTER 2

Detectors

Gamma ray emitted by an unstable nuclide are detected through their interaction with matter. The most common gamma-ray detector used in nuclear medicine is the Anger camera [8], which consists of a scintillation crystal coupled to an optical window and an array of photomultiplier tubes (PMTs). The large clinical Anger cameras are not always well suited for small-animal imaging, and a lot of effort has been devoted to developing better detectors for pre-clinical imaging in the last few decades. A complete discussion of recent advances in detector instrumentation can be found in Peterson and Furenlid (2011) [134]. Another complete discussion of different types of detectors can be found in Barrett and Hunter (2005) [19].

Gamma-ray detector development has been a core project for the Center for Gamma-Ray Imaging (CGRI) since its creation. The standard Modular Camera (ModCam), which can be considered a pre-clinical version of the clinical Anger camera, was first developed by John Aarsvold [2] and Tom Milster [119, 120], and later improved by Sain [139] and Furenlid [63, 64, 66]. This camera has been successfully used in multiple pre-clinical SPECT and PET imaging systems developed at CGRI, both in its small version (4 PMTs) and its large version (9 PMTs). This work uses the large version of the ModCam. Bill Hunter investigated the use of multi-anode photomultiplier tubes (MAPMTs) [81]. Semiconductor detectors have also been investigated, and in particular cadmium telluride (CdTe) and cadmium zinc telluride (CdZnTe) detectors have been of interest for nuclear imaging [11, 30, 31, 73, 122, 161]. CGRI has contributed to developing semiconductor detectors for nuclear imaging, and a complete review of the history can be found in Barber and Woolfenden [10]. These contributions include the discovery of small pixel effect [16], as well as the production of a 64 by 64 CZT pixel array detector [12, 100] that was used in two pre-clinical SPECT imaging systems with high

resolution : the dual modality system [86] and SemiSPECT [89]. Silicon detectors have been used successfully by Shokouhi and Peterson at Vanderbilt University, in a system called SiliSPECT [145, 146]. More recently, Brian Miller developed a new detector technology based on coupling the light emitted by a scintillator through and optical gain stage to a conventional CMOS detector, called iQID [114, 116], and used 20 of these detectors in a SPECT imaging system dedicated to imaging the mouse brain [118]. Heather Durko investigated the properties of silicon double-sided strip detectors [57] and developed an adaptive anamorphic SPECT imaging system using one of them. Finally, Esen Salcin investigated the potential of strip detectors for SPECT imaging [140].

2.1 Interaction of gamma rays with matter

The typical gamma-ray photons used in SPECT imaging have an energy between 100 keV and 511 keV. The gamma-ray photons carry an electromagnetic field and will therefore interact with an electric charge. Compton scattering and the photoelectric effect are the only two significant interactions occurring in gamma-ray detectors at these energies.

2.1.1 Compton Scattering

Compton scattering, as illustrated in Figure 2.1a, is an inelastic scattering of the incident gamma-ray photon by a quasi-free electron in the absorbing material. The electron can be treated as a free electron because its binding energy ($\leq$ 100 eV) is much less than the energy of the incoming gamma-ray photon (100 - 500 keV). By applying conservation of energy and momentum and special relativity, the energy of the resulting Compton electron is

$$E_{\text{Compton}} = E_{\gamma} - E_{\gamma'}, \tag{2.1}$$

where $E_{\gamma'}$, the energy of the gamma-ray photon after scattering, is given by

$$E_{\gamma'} = \frac{E_{\gamma}}{1 + \frac{E_{\gamma}}{mc^2}(1 - \cos\theta)}. \tag{2.2}$$

The Compton electron can efficiently transfer its kinetic energy to the detector material, causing secondary ionizations. The scattered gamma ray can interact again in the detector, or escape, resulting in a partial energy deposition.

2.1.2 Photoelectric effect

When the incoming gamma-ray photon interacts with a bound electron it can transfer all of its energy to the electron. When this occurs,the atom is ionized, the gamma-ray photon disappears, and a photoelectron is ejected. This process is called the "photo-electric effect" and is illustrated in Figure 2.1b. The ejected photoelectron has the following kinetic energy:

$$E_{kinetic} = E_{\gamma} - E_{be}, \tag{2.3}$$

where E_{γ} is the energy of the gamma-ray photon, and E_{be} is the binding energy of the electron. The ejected photoelectron, like the Compton electron, can efficiently create secondary ionizations.

The ejection of the photoelectron also creates a vacancy in the electric shell of the atom, which will be filled by an electron from a higher atomic level, leading to the emission of a characteristic X-ray fluorescence photon and/or Auger electrons. The atomic reconfiguration will then lead to more vacancies, creating yet more reconfiguration transitions. All these events happen on a time scale of 10^{-13} to 10^{-15} seconds. The photoelectron is re-absorbed within a few millimeters of travel.

2.2 Inorganic scintillation detectors

We have described the two main initial interactions that can happen between a high energy gamma-ray photon and matter. Different detector technologies differ in how they respond to this initial interaction and its secondary processes. In gas detectors, the deposited energy creates electron-ion pairs that can migrate towards opposite electrodes under the influence of an applied electric field. An in-depth treatment of this kind of detector can be found in chapter 18 of [167]. In semiconductor

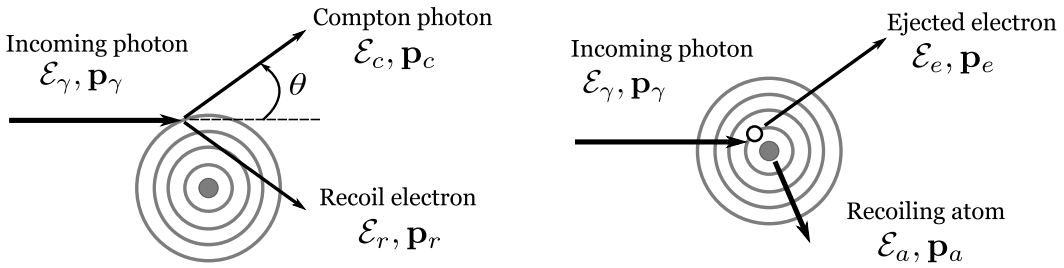

(a) Compton Scattering (b) Photoelectric Effect

Figure 2.1: Illustration of the gamma-ray interaction processes. (a) Compton scattering: a gamma-ray photon interacts with an outer shell electron creating a scattered photon and a recoil electron. (b) Photoelectric effect: a gamma-ray interacts with a bound electron ejecting an electron and leaving a hole in the valence band.

detectors, the deposited energy creates electron-hole pairs that also create small currents between electrodes under the influence of a field. Detailed treatment of this kind of detector can be found in chapter 15 of [167], as well as in [81] and [21]. The type of detector of interest in this dissertation is the scintillation detector in which the absorbed gamma-ray photon creates an ensemble of electron-hole pairs (in the case of an inorganic scintillation material), or excited valence electrons (in the case of an organic scintillation material), that return to their ground state *via* emission of visible-energy photons. The scintillation crystal used in the modular camera is a thallium-doped sodium iodide crystal, NaI:Tl.

2.2.1 Properties of inorganic scintillation crystals

Scintillation crystals have various properties that are important to consider when developing a gamma-ray detector [91]. For instance, it is desirable that the crystal has a high conversion rate of gamma-rays to scintillation photons. The emission wavelength of the scintillation photons should also match the spectral sensitivity of the photosensitive device to which the crystal will be coupled. The energy response of the detector should be linear and provide high energy resolution to allow for filtering out scattered photons, which is especially important in clinical applications. The scintillation crystal should also have a high stopping power so that a thin crystal

can be used in the detector especially when the depth of interaction will not be estimated. Finally, the crystal should have appropriate mechanical properties so that it will not break when mounted to a detector. Since NaI:Tl has very satisfying properties, it is commonly used in scintillation cameras [167]. It does, however, have the disadvantage of being highly moisture sensitive, such that highly effective hermetic seals are required.

Luminescence

A simple solid-state model can be used to describe the conversion of a gamma-ray photon to an ensemble of visible photons in a scintillation crystal, such as the one shown in Figure 2.2. The filled band corresponds to the energies of electrons bound in atomic-like orbitals. The valence band is the highest completely filled energy band at $T = 0$. The conduction band contains mobile electrons that can move freely through the crystal. The intermediate energies are forbidden; no electron can exist in a pure crystal with those energies. When a crystal is doped, by introducing a small amount of impurities, additional energy states are created in the forbidden bands. These impurities are called activation or luminescence centers because they enable the scintillation of visible light. The scintillation process can be described in the following steps [137, as cited in 42]:

1. The gamma-ray photon interacts with the scintillation crystal either through the photoelectric effect or Compton scattering.

2. In the case of the photoelectric effect, the traveling photoelectron will interact with multiple atoms in the crystal, creating secondary photoelectrons and matching holes with lower energy.

3. The lower-energy photoelectrons relax. The electrons move downward to the bottom of the conduction band and the holes move toward the top of the valence band. This process results in the creation of multiple electron-hole pairs with energy equal to the band gap energy E_g.

4. The electrons and holes travel, sometimes as loosely bound pairs known as excitons, to the activation centers where recombinations leading to the excitation of the activation center can happen :

$$Tl^+ + e^- + h^+ \rightarrow (Tl^+)^*$$

$(Tl^+)^*$ represents an excited thallium ion.

5. The excited thallium ion relaxes and emits optical an photon in the process:

$$(Tl^+)^* \rightarrow Tl^+ + h\nu$$

The de-excitation of the thallium ion takes place within about 250 ns, and the wavelength of the optical photons emitted is around 420 nm, or 3 eV.

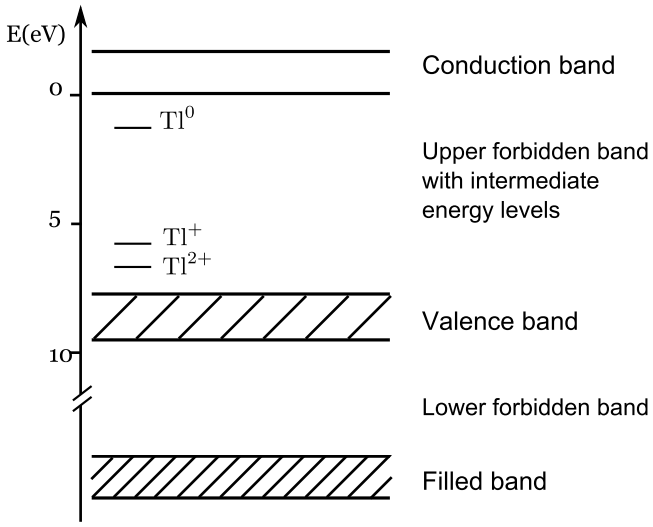

Figure 2.2: Transition diagram of a NaI:Tl crystal

Not all excited thallium ions will de-excite and emit visible light. Some de-excite without emission (non-radiative transitions) while some remain for a longer period of time in an excited state (metastable states). Indeed, many scintillators exhibit light yield with two or more characteristic time scales. However, the optical photons emitted during de-excitation will never be re-absorbed by the crystal because their

energy is less than the band-gap energy. The doped crystal is therefore transparent to its own scintillation light.

Conversion efficiency

One important parameter of a scintillation crystal is its conversion efficiency: the ability to convert the energy of a gamma-ray photon into as many visible photons as possible. Of all the energy a gamma-ray deposits in a scintillator material, only a fraction will be converted into useful optical photons while the rest will be lost to competing processes. The number of optical photons produced by each interaction obeys a statistical distribution with a mean value $\overline{N}_{opt}(\mathcal{E})$ for a given energy $\mathcal{E}$, given by:

$$\overline{N}_{opt}(\mathcal{E}) = \mathrm{Q}_{sc}\mathcal{E}, \tag{2.4}$$

where Q_{sc} is the scintillator efficiency, a net probability that includes the electron-hole production efficiency, the transport efficiency of electron-hole pairs to activator sites, and the quantum efficiency of the luminescent activator. Ideally, the scintillator efficiency will not depend on the energy of the incident photon, though in practice it often does, an effect termed non-proportionality. The conversion efficiency of NaI:Tl at room temperature was measured to be 11.3% [79, as cited in 42]. For a gamma ray of 140 keV energy at room temperature, there will be about 5000 visible photons produced traveling in random (isotropic) directions.

2.2.2 Properties of photomultiplier tubes (PMTs)

PMTs are used to convert the light emitted by the scintillation crystal into an electric signal. They have high gains and are able to convert low levels of light into detectable signals. Drawbacks of PMTs are that they have a low quantum efficiency and are sensitive to magnetic fields. This makes detectors based on PMTs impossible to be used in a simultaneous SPECT/MR configuration.

Figure 2.3 shows a schematic of a typical photomultiplier tube. When a photon hits the photocathode deposited on the inside of the PMT entrance window, it may

generate a single photoelectron in the tube vacuum *via* the photoelectric effect. The spectral response of a PMT is determined by the material used for the entrance window and photocathode. For PMTs designed to be coupled with a NaI:Tl crystal, the photocathode is usually a bialkali material because their spectral response ranges from 200nm to 600 nm and is peaked near the emission maximum of NaI:Tl scintillation crystals. The quantum efficiency of the PMT depends on the following factors: light reflection on the glass window, light reflection at the glass/photocathode interface, photoelectric cross-section of the photocathode material, and the thickness of the photocathode. The electrons produced at the photocathode that enter the vacuum are accelerated by the electric field inside the PMT and directed towards the first dynode by a focusing electrode or grid. At each dynode, the electrons will produce secondary electrons by depositing the kinetic energy picked up between dynode stages. Each set of secondary electrons are directed towards the next dynode until the final burst of electrons reach the anode. The anode output current can then be used in an external electronic circuit.

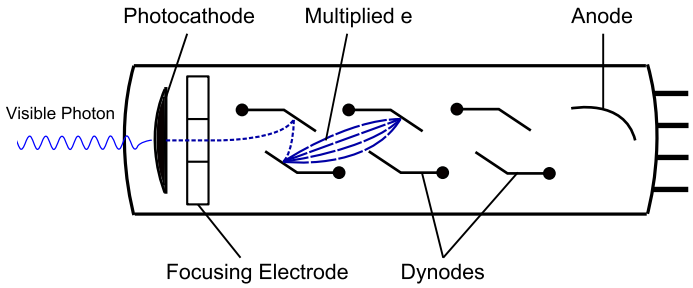

Figure 2.3: Schematic of a photomultiplier tube. A photon generates photoelectrons upon hitting the photocathode. The photoelectrons are then amplified through the dynodes until they hit the anode.

PMT gain

The number of photoelectrons produced in a PMT is a random variable. After a gamma-ray interaction happens at a location $\mathbf{r_d}$ in the scintillation crystal, a number of optical photons described by a probability distribution characteristic of

the scintillation material and the gamma-ray energy are emitted isotropically. Out of these photons, only a fraction $f_j(\mathbf{r_d})$ will reach the PMT number j. Some photons will reach this PMT directly while others will first bounce off various interfaces and edges. Once the optical photons hit PMT j, only a fraction η_j of these photons will be converted to photoelectrons while the rest are lost. Thus, the collection and detection of the optical photons produced in the scintillator crystal is a combination of two binomial processes: either the optical photon hits the PMT or it doesn't, and if it hits, it is either converted to a photoelectron or it isn't. The combination of two binomial selection processes is a binomial process [21] and, therefore, the mean number of photoelectrons that will be amplified by PMT j is

$$\overline{N}_j(\mathbf{r_d}, \mathcal{E}) = \eta_j f_j(\mathbf{r_d}) \overline{N}_{opt}(\mathcal{E}) \tag{2.5}$$

$$= \eta_j f_j(\mathbf{r_d}) \mathrm{Q}_{sc} \mathcal{E} \tag{2.6}$$

The PMT gain $\overline{G}_j^{PMT}$, in units of output electrons per input photoelectrons is a random variable that depends on applied high voltage and the dynode structure. There is currently no predictive model to describe it from first principle. The gain of the electronics associated with the PMT G_j^{elec}, which has units of volts per output electron, has much smaller randomness. One can assume that the photoelectrons produced on the PMT photocathode are amplified individually and that the total voltage V_j produced by the PMT and its read-out amplifier is the sum of statistically independent voltages produced by a large number of photoelectrons. Therefore, V_j will have a normal distribution with mean

$$\overline{V}_j = G_j^{elec} \overline{G}_j^{PMT} \overline{N}_j(\mathbf{r_d}, \mathcal{E}) \tag{2.7}$$

$$= G_j^{elec} \overline{G}_j^{PMT} \eta_j f_j(\mathbf{r_d}) \mathrm{Q}_{sc} \mathcal{E}. \tag{2.8}$$

The variance is given by (an expression due to Burgess)

$$\mathrm{Var}(V_j) = [(G_j^{elec})^2 \mathrm{Var}(\overline{G}_j^{PMT}) + (\overline{G}_j)^2] \eta_j f_j(\mathbf{r_d}) \mathrm{Q}_{sc} \mathcal{E}, \tag{2.9}$$

where $\overline{G}_j = G_j^{elec} \overline{G}_j^{PMT}$ [20].

Electronic noise

The read-out electronics associated with the PMT also have some noise that can be described by a zero-mean Gaussian, with variance σ_j^2 that adds to expression 2.9. The electronic noise is dependent on the actual electronics components used as well as on the sampling and amplifying of the analog pulses coming from the PMTs. The electronic noise variance in the circuit as well as any DC offsets can be measured by turning off the high-voltage supply of the PMT and sampling the output.

2.3 The modular camera (ModCam)

The compact modular camera used in this work was developed at CGRI in 2000 as a preclinical version of the Anger camera [8]. The electronics used in this work were first developed for FastSPECT II [64] and were designed to amplify and digitize the signal of each PMT independently of the others. This design permits the use of statistical positioning algorithms such as Maximum Likelihood [2, 71, 119, 121].

2.3.1 Modular camera design

The modular camera used in AdaptiSPECT (illustrated in Figure 2.4) consists of a 5-mm-thick monolithic NaI:Tl scintillation crystal coupled to an 8-mm-thick optical window and an array of 3x3 PMTs with 1.5 inch diameters. The modular camera was designed to be used with statistical methods for position estimation. The optical window, for example, is used to spread the scintillation light to multiple PMTs. This permits the estimation of an interaction position to have a much finer resolution than the photodetector pitch [81]. The material used for the optical window is fused quartz because it is transparent to visible light and its refraction index at 415nm (the peak emission of NaI:Tl) is smaller than the refraction index of NaI:Tl, which increases the light spread. A relatively thin window, such as the one used in the AdaptiSPECT cameras, leads to a high resolution but with the trade-off of having a variance that depends slightly on where in the crystal the gamma-ray interacts.

Another very important factor in the design of modular cameras is the treat-

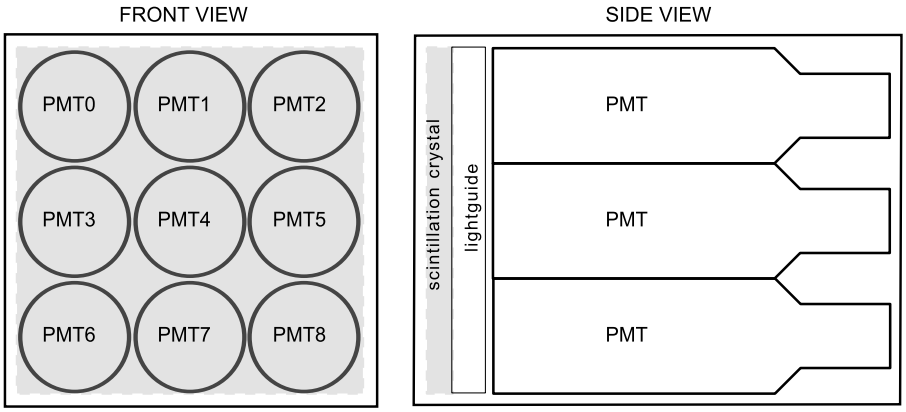

Figure 2.4: Design of the modular camera consisting of a scintillation crystal coupled to a lightguide connecting to an array of 3x3 PMTs.

ment of the optical interfaces in the detector. An in-depth review of various optical treatments and their consequences on the detector response can be found in Bill Hunter's dissertation [81] and in Stephen Moore's dissertation [128]. For the modular cameras used in this work, the scintillator entrance face comprises a Lambertian reflector that redirects optical photons emitted during the scintillation process towards the PMTs. The edges of the scintillator crystal are blackened and will absorb most of the optical photons that hit it. This treatment has been found to allow statistical positioning estimation methods to work out to the crystal edges.

The 16 detectors for AdaptiSPECT were manufactured by Radiation Sensors, Alabama [135].

2.3.2 List-Mode electronic acquisition

The data acquired by each camera is kept in a super-list-mode format. For each interaction, the full set of PMT voltages is recorded as well as the time of observation. This acquisition mode allows for conservation of all information for later processing [23, 33, 92, 132]. The electronics developed for the modular camera consist of both a front-end board that performs digital event detection and list-mode-entry generation and a back-end board that buffers the data transmitted by the front-end

board and communicates with the host computer through a PCI interface. Communication between the front-end and back-end boards is done through a standard ethernet cable, though the ethernet packet protocol is not used. This acquisition chain is shown in Figure 2.5.

Front-End electronics

Front-end electronics are designed to process and prepare the PMT signals. Each board consists of 9 amplifiers that amplify the signals sent from the PMTs. The signals are then shaped through analog filters and digitized using 12 bit analog-to-digital converters at 33 MHz. The front-end board can process 3.5 Gbits of data per second.

Back-End electronics

The back-end boards are designed to manage the list-mode data coming in. Each board can support two front-end boards in two independent channels. Each channel has a memory module associated with it that can hold 1 million 32-bit words before transferring them to the host computer through the PCI bus. Most of the electronics on the boards are dedicated to the PCI communication.

Communication Driver

AdaptiSPECT, like FastSPECT II [66], uses 16 detectors and consequently has a total of 16 front-end boards and 8 back-end boards. FastSPECT II originally needed two computers with 4 PCI slots each to acquire all the data. Since recently manufactured motherboards rarely come with 4 PCI slots, a new driver was developed for the list-mode electronics to accommodate motherboards lacking multiple PCI slots. The new driver enables the acquisition electronics to use either a PCI slot, if the motherboard has one, or with a PCI-to-PCIe expansion chassis. Furthermore it is compatible with the latest versions of the Windows operating system. For the rest of this work, we use two PCI-to-PCIe expansion chassis manufactured by

StarTech that enable 4 PCI cards to connect to a single PCIe slot with the additional advantage of needing just one computer to control the entire system. We have already implemented this transition on FastSPECT II, refitting it with a more recent computer and two expansion boxes. This configuration is successfully operating on FastSPECT II since January 2013. In Figure 2.6 we show the current StarTech expansion chassis, as well as the setup used on FastSPECT II.

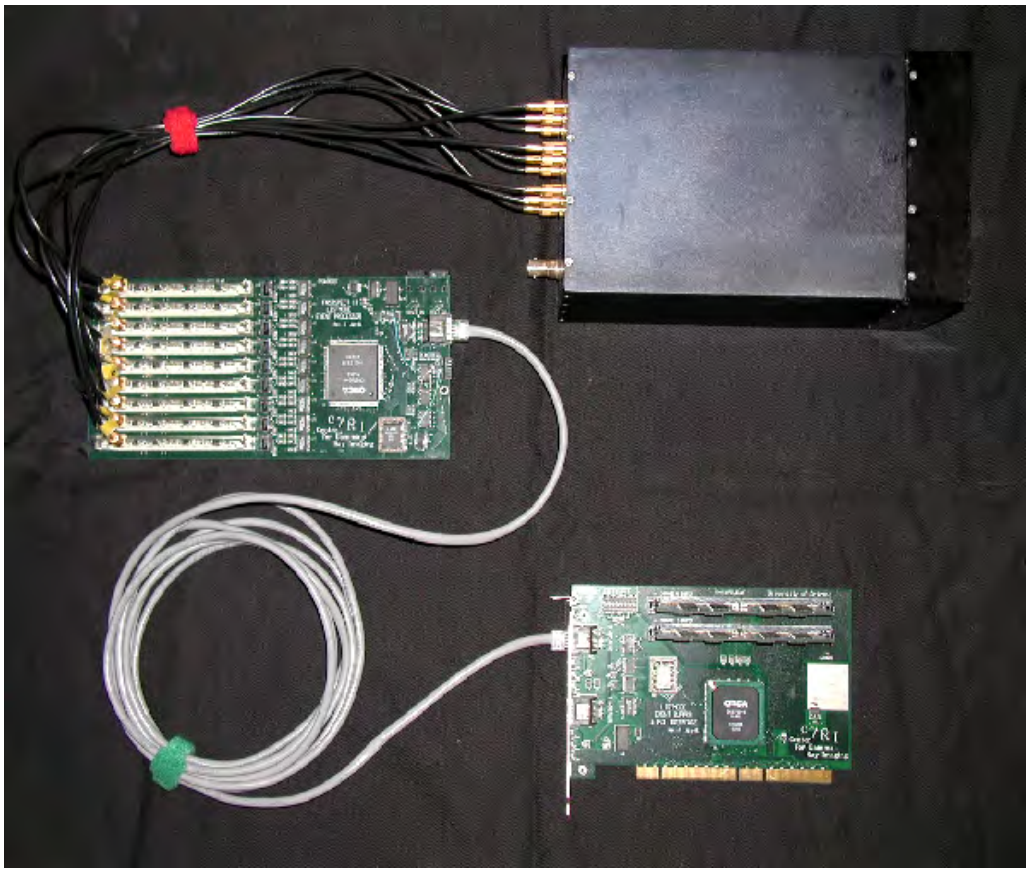

Figure 2.5: List-Mode acquisition chain. The 9 PMTs of a modular camera (upper right) are connected to the front-end acquisition board. The front-end board is responsible for detecting, shaping and amplifying the signals from each PMT, and generating the list-mode data. The data is then transmitted to the back-end board (bottom right) through a standard ethernet cable. The back-end board is designed to buffer the data from two front-end acquisition boards and communicates with the host PC.

(a) Inside the box (b) Two boxes

Figure 2.6: Expansion boxes used to link 4 PCI boards to 1 PCIe channel. (a) Two list-mode acquisition buffers are visible with room for two additional boards. (b) Photo of the two boxes hosting all 8 acquisition boards for FastSPECT II.

2.3.3 Sources of randomness in the modular camera

To use statistical estimation methods for estimating the interaction position $\mathbf{r_d}$ inside the scintillation crystal, it is important to understand the sources of signal variability in the detectors in order to build an accurate model relating the measured outputs to the interaction position. The sources of randomness for the scintillation process and the PMT amplification process described in the previous sections are summarized again here:

- The number of optical photons, $\overline{N}_{opt}$, created by a gamma-ray interaction in NaI:Tl is governed by Poisson statistics.
- Each optical photon undergoes two binomial selection processes before being amplified by a photomultiplier tube. The binomial selection of a Poisson distribution is also a Poisson distribution [21].
- The PMT gain is characterized by a gain mean and variance.

Assuming that the number of optical photons, $\overline{N}_{opt}$, produced in the scintillator is Poisson distributed (note that this assumption is not true for all scintilla-

tors [20, 81]), then the signal output from a PMT is also Poisson distributed [21]. In particular, it is a scaled Poisson distribution because of the multiplicative gain. Since it has been observed that the signals from each of the 9 PMTs are independent [39], the probability of measuring a set of specific output signals, $\{V_j\}$, given an interaction location $\mathbf{r_d}$ and energy $\mathcal{E}$ is given by:

$$\mathrm{pr}(\{V_j\}|\mathbf{r_d},\mathcal{E}) = \prod_{j=1}^{9} \mathrm{pr}(V_j|\mathbf{r_d},\mathcal{E}), \tag{2.10}$$

where V_j is the voltage measured at PMT j.

Since the voltage from each PMT is scaled by the total gain of that PMT, the raw data acquired at PMT j is given by:

$$g_j = \mathrm{NINT}\left(\frac{V_j}{G_j}\right), \tag{2.11}$$

where $\overline{G}_j = G_j^{elec}\overline{G}_j^{PMT}$ is the total gain of the PMT stage and NINT represents the nearest integer operator. With this definition for g_j, the raw data measured is the number of photoelectrons produced at the photocathode of PMT j, which we have described earlier as being a Poisson random variable with mean $\overline{N}_j(\mathbf{r_d},\mathcal{E})$ described in equation 2.5, and probability density function:

$$\mathrm{pr}(N_j|\mathbf{r_d},\mathcal{E}) = \frac{\left[\overline{N}_j(\mathbf{r_d},\mathcal{E})\right]^{N_j}}{N_j!}\exp\left[-\overline{N}_j(\mathbf{r_d},\mathcal{E})\right]. \tag{2.12}$$

Combining equations 2.10 and 2.12 leads to a probability of measuring data vector $\mathbf{g} = \{g_1, g_2, ...g_9\}$ for the 9 PMTs of the modular camera given by:

$$\mathrm{pr}(\mathbf{g}|\mathbf{r_d},\mathcal{E}) = \prod_{j=1}^{9} \frac{\left[\overline{N}_j(\mathbf{r_d},\mathcal{E})\right]^{g_j}}{g_j!}\exp\left[-\overline{N}_j(\mathbf{r_d},\mathcal{E})\right]. \tag{2.13}$$

We call this probability distribution the likelihood model of the camera and will use it in next sections for position estimation.

2.4 Maximum-Likelihood position estimation

The scintillation process and the collection of the scintillation light by a PMT are two stochastic processes. As a consequence, two gamma-ray photons interacting at the exact same location in the scintillation crystal will lead to different PMT outputs being measured. It is therefore impossible to have an accurate deterministic solution to the question of where the interaction occurs given the measurements obtained. Instead, various estimation methods have been developed to answer this question. Here we will cover the basics of the maximum-likelihood estimation method and its implementation for the modular camera.

2.4.1 Basis of ML estimation

We define $\mathbf{g}$ as the vector of observations made and $\boldsymbol{\theta}$ as the vector of parameters to estimate. In the case of the modular camera, for an event j, $\mathbf{g}_j$ is a list of the 9 digitized PMT voltages. The corresponding parameters to estimate are the interaction position and energy, $\boldsymbol{\theta}_j = \{\mathbf{r_d}, \mathcal{E}\}$. The estimated vector is denoted $\hat{\boldsymbol{\theta}}$. By definition, the ML estimate of the parameter vector is the vector that maximizes the likelihood of the probability model $\mathrm{pr}(\mathbf{g}|\boldsymbol{\theta})$:

$$\hat{\boldsymbol{\theta}}_{\mathrm{ML}} \equiv \underset{\boldsymbol{\theta}}{\operatorname{argmax}} \left\{ \mathrm{pr}(\mathbf{g}|\boldsymbol{\theta}) \right\}. \tag{2.14}$$

Alternatively, the log-likelihood of the probability model can be used:

$$\hat{\boldsymbol{\theta}}_{\mathrm{ML}} = \underset{\boldsymbol{\theta}}{\operatorname{argmax}} \left\{ \ln \left(\mathrm{pr}(\mathbf{g}|\boldsymbol{\theta}) \right) \right\}. \tag{2.15}$$

The interaction position within the crystal, $\mathbf{r_d}$, is a 3-dimensional vector. It is difficult however, to estimate the depth of interaction within the crystal unless there are more PMTs [82, 128] and therefore, using a thin crystal, we assume the interaction to be described by a 2-dimensional vector: $\mathbf{r_d} = \{x_d, y_d\}$.
An accurate likelihood model is needed to use the maximum-likelihood estimator. In this work, we use the model described in section 2.3.3. Thus, estimating the vector parameter $\boldsymbol{\theta} = \{x_d, y_d, \mathcal{E}\}$ for an event j generating a set of measurements $\mathbf{g}_j$

is equivalent to solving:

$$\left\{\hat{\mathbf{r}}_{\mathbf{d}}, \hat{\mathcal{E}}\right\} = \underset{\mathbf{r_d},\mathcal{E}}{\operatorname{argmax}} \left\{ \ln\left(\prod_{j=1}^{9} \frac{\left[\overline{N}_j(\mathbf{r_d},\mathcal{E})\right]^{g_j}}{g_j!} \exp\left[-\overline{N}_j(\mathbf{r_d},\mathcal{E})\right] \right) \right\} \tag{2.16}$$

$$= \underset{\mathbf{r_d},\mathcal{E}}{\operatorname{argmax}} \left\{ \sum_{j=1}^{9} \left[g_j \ln\left(\overline{N}_j(\mathbf{r_d},\mathcal{E})\right) - \overline{N}_j(\mathbf{r_d},\mathcal{E}) \right] - \sum_{j=1}^{9} \ln\left(g_j!\right) \right\}. \tag{2.17}$$

The last term of equation 2.17 does not depend on the parameters to estimate and can be ignored. For a known energy $\mathcal{E}$, the parameters to estimate, $\boldsymbol{\theta} = \{x_d, y_d\}$ will then maximize the following equation:

$$\{\hat{x}_{d,\mathrm{ML}}, \hat{y}_{d,\mathrm{ML}}\} = \underset{x_d,y_d}{\operatorname{argmax}} \left\{ \sum_{j=1}^{9} \left[g_j \ln\left(\overline{N}_j(x_d,y_d)\right) - \overline{N}_j(x_d,y_d) \right] \right\}. \tag{2.18}$$

Various search methods have been developed and tested to find $\{\hat{x}_{d,\mathrm{ML}}, \hat{y}_{d,\mathrm{ML}}\}$ using equation 2.18. A description of these methods can be found in [42]. In this work, we use the contracting grid algorithm developed in [76] and implemented on a GPU by Luca Caucci and Stephen Moore [34, 128].

When estimating the interaction position using equation 2.18, we can precompute part of the log-likelihood associated with the position. If we also precompute the term left over from equation 2.17, $-\sum_{j=1}^{9} \ln\left(g_j!\right)$, we have the complete likelihood associated with the estimated position: $\mathcal{L}\left(\hat{x}_{d,\mathrm{ML}}, \hat{y}_{d,\mathrm{ML}}\right)$. We can then use a likelihood threshold technique to reject events that have signals inconsistent with a single, simple energy deposition. In practice, the log-likelihood is compared to a threshold and every event that is below the threshold is rejected. Other rejection techniques such as Bayesian windowing [40, 41] and energy windowing have also been implemented, and tested in other works. Here we use the likelihood windowing method for its ease in implementation. An event is accepted if its associated likelihood satisfies:

$$\mathcal{L}\left(\hat{x}_{d,\mathrm{ML}}, \hat{y}_{d,\mathrm{ML}}\right) > \mathcal{L}_0\left(\hat{x}_{d,\mathrm{ML}}, \hat{y}_{d,\mathrm{ML}}\right) \tag{2.19}$$

where $\mathcal{L}_0\left(x_d, y_d\right)$ is a position-dependent likelihood map, calculated during the calibration of the detector.

In order to use equation 2.18 to estimate $\{x_d, y_d\}$ and equation 2.19, the mean number of photons for each position $\overline{N}_j(x_d, y_d)$ and the likelihood map $\mathcal{L}_0(x_d, y_d)$ must be determined. This can be done by calibrating the modular camera and measuring the mean number of photons acquired for each position at a given energy. The likelihood map can then be derived from this measurement.

2.4.2 Detector calibration

Calibration of the modular camera consists of two steps. First, the high-voltage supply for the camera is set and the gain for each PMT is adjusted. Then, a collimated source of known energy is scanned on a grid across the detector surface. This scan leads to the measurement of the mean number of photons at each location for each PMT: $\overline{N}_j(\mathbf{r_d}, \mathcal{E})$. We call this the mean detector response function, or MDRF. Ideally, a grid as fine as possible would be scanned and a large number of photons collected for each position. In practice though, it is recommended to keep the acquisition scan duration under a half-life of the radioactive material used for the calibration. When calibrating for ^{99m}Tc, which has a half-life of 6 hours, we scan a grid of 79×79 points spaced by 1.5mm in each direction across the surface. At each location we record around 5000 events and collect the PMT responses for each event. The mean number of photons collected per PMT is then generated from this dataset after filtering out events that are likely to have scattered. Photos of the MDRF acquisition bench and the collimator used is shown in Figure 2.7. After acquisition, the MDRF is interpolated twice for each PMT to a grid of 313×313 points with 0.375mm spacing using software developed by Stephen Moore [128]. The software includes a Compton filter, likelihood windowing, MDRF interpolation, and MDRF smoothing. A result of an MDRF for one of the AdaptiSPECT cameras is shown in Figure 2.8.

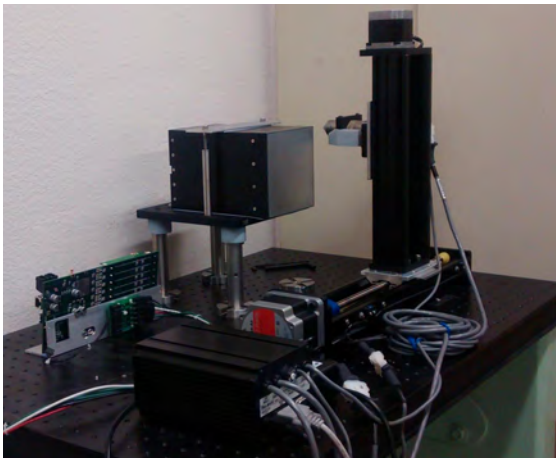

(a) MDRF acquisition bench

(b) Collimator

Figure 2.7: (a) MDRF acquisition bench with two stages to scan the collimator across the detector face. (b) The collimator, which consists of a body that can contain a capillary filled with radioactive material, and a head.

2.4.3 Camera intrinsic resolution and detector covariance

An interesting property of the modular camera that can be derived from the calibration set is the detector's covariance matrix, which is a measure of the spatial resolution of the detector. The variance and covariance are dependent on the estimator used and here we only consider the maximum-likelihood estimator. For a vector of parameters to estimate $\boldsymbol{\theta}$, the covariance matrix elements are given by:

$$[\mathbf{K}_{\hat{\boldsymbol{\theta}}}]_{nn'} \equiv \left\langle \left[\hat{\theta}_n - \left\langle \hat{\theta}_n \right\rangle\right] \left[\hat{\theta}_{n'} - \left\langle \hat{\theta}_{n'} \right\rangle\right] \right\rangle_{\mathbf{g}|\boldsymbol{\theta}}, \tag{2.20}$$

where the expression in brackets is the average over many realizations $\mathbf{g}$ given a parameter $\boldsymbol{\theta}$. In the case of the modular camera, two parameters x and y are estimated for the interaction position. Therefore, the covariance matrix is a 2×2 matrix with the following elements:

$$[\mathbf{K}_{\hat{\boldsymbol{\theta}}}] = \begin{bmatrix} \sigma_x^2 & \rho\sigma_x\sigma_y \\ \rho\sigma_x\sigma_y & \sigma_y^2 \end{bmatrix}, \tag{2.21}$$

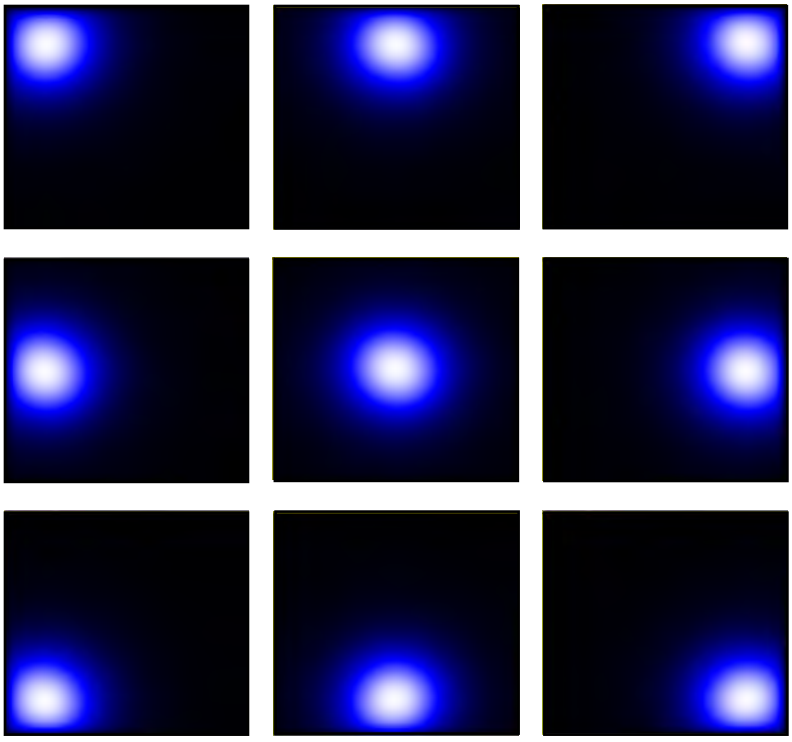

Figure 2.8: Example of MDRF plot for camera with serial number SN15012101, currently camera 00 on AdaptiSPECT. Each figure show the response of one of the PMT accross the detector surface.

where σ_x^2 and σ_y^2 are the variances along the $x-$ and $y-$axis respectively, and ρ is the covariance of x and y.

For an unbiased estimator, the variance has a lower limit given by the Cramér-Rao lower bound. The bias of an estimator is defined as:

$$\mathbf{b}\left(\boldsymbol{\theta}\right) \equiv \left\langle \hat{\boldsymbol{\theta}} \right\rangle_{\mathbf{g}|\boldsymbol{\theta}} - \boldsymbol{\theta}, \tag{2.22}$$

where $\boldsymbol{\theta}$ is the true value, $\hat{\boldsymbol{\theta}}$ is an estimate, and $< \hat{\boldsymbol{\theta}} >_{\mathbf{g}|\boldsymbol{\theta}}$ indicates the average over many events with true value $\boldsymbol{\theta}$.

An unbiased estimator is one for which $\mathbf{b}\left(\boldsymbol{\theta}\right) = 0, \forall \boldsymbol{\theta}$.

Then we introduce the Fisher Information Matrix [60, as cited in 20], denoted $\mathbf{F}$, whose elements are defined by:

$$\left[\mathbf{F}\right]_{nn'} \equiv \left\langle \left[\frac{\partial}{\partial\theta_n} \ln \mathrm{pr}\left(\mathbf{g}|\boldsymbol{\theta}\right)\right] \left[\frac{\partial}{\partial\theta_{n'}} \ln \mathrm{pr}\left(\mathbf{g}|\boldsymbol{\theta}\right)\right] \right\rangle_{\mathbf{g}|\boldsymbol{\theta}}. \tag{2.23}$$

An unbiased estimator achieves the Cramér-Rao lower bound when the variance satisfies:

$$\mathrm{Var}\left(\hat{\theta}_n\right) = \left[\mathbf{F}^{-1}\right]_{nn}. \tag{2.24}$$

To measure the variance and covariance of the detector from the calibration set, we first need to know the width of the calibration beam. We measured it by placing the collimator in front of a detector at the same distance as during a calibration set. We then placed a tungsten edge between the collimator and the detector and translated it laterally, recording the number of counts measured every time the collimator was moved. We then took the derivative of the datapoints acquired and fitted a Gaussian curve to it to obtain the profile of the beam. The measurement results are shown in Figure 2.9. Five datasets were acquired and a 1D-Gaussian was fitted to each dataset. The final width is the average of all five individual measurements and is found to be $\sigma_{beam} = 0.51$mm, which corresponds to a beam size of 1.2mm when considering the full width at half maximum. The intrinsic variance in position estimates of the detector can then be retrieved using the following relation:

$$\sigma^2_{intr} = \sigma^2_{meas} - \sigma^2_{beam}, \tag{2.25}$$

where σ^2_{meas} is the measured variance and σ^2_{beam} is the beam variance. A map of the detector's covariance is shown in Figure 2.10. The minimum variance achieved is 1.5mm.

Another way to look at the intrinsic resolution of the detectors is to look at a grid-point array from the calibration data. In Figure 2.11a, we show a grid of points spaced 5 mm apart. In the regions between 4 PMTs, where the MDRFs have steep slopes, the points have isotropic resolution. However, the resolution degrades on the edges of the camera where fewer PMTs have significant slope and therefore less information is available. This is particularly visible when superimposing the point-grid array with a shape of the 9 PMTs and a map of the total variance of the camera, as shown in Figure 2.11b. In this figure we represent the standard deviation as the square root of the sum of the diagonal terms of the covariance

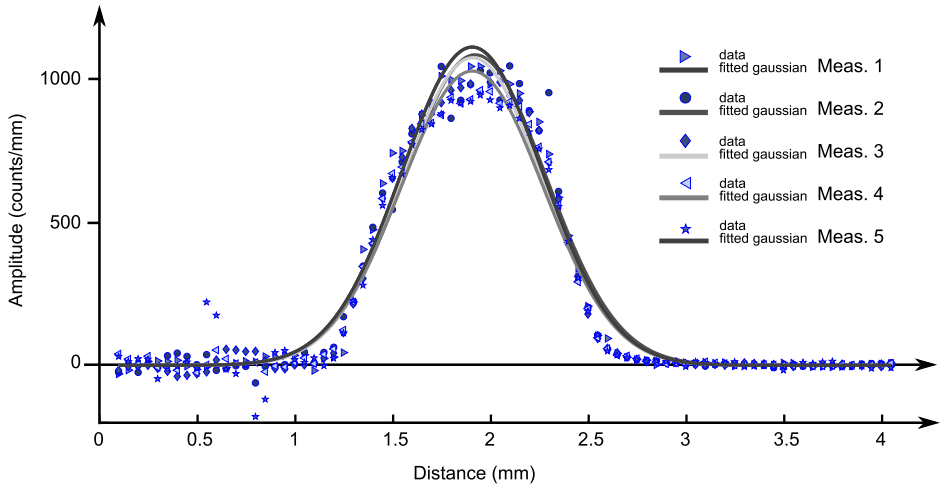

Figure 2.9: Results of the measurement of the beam size of the collimated source. Five datasets were acquired and a 1D-Gaussian was fitted to each dataset.

matrix: $\sigma_{tot} = \sqrt{\sigma_x^2 + \sigma_y^2}$. The darker areas at the intersections of 4 PMTs represent the lower variances.

2.5 Crystal yellowing and consequences for ML

An unfortunate property of NaI:Tl crystals is that they are highly hygroscopic. That is, if not sealed properly, they will absorb moisture from the air leading to precipitation of thallium in the crystal and degradation of the detector performance. Crystal yellowing can happen slowly over time, or it can happen suddenly if the hermetic seals fail, as was the case for the cameras built for AdaptiSPECT. A commercial Anger camera crystal typically lasts for approximately 8 years.

2.5.1 Crystal yellowing

After a NaI:Tl crystal has been in contact with moist air, yellow patches are visible on the surface of the normally transparent crystal. Hence the term *crystal yellowing* is used to describe the phenomenon. The yellow color actually comes from the reaction of Thallium with the moist air to form thallium-hydroxide, TlOH, which has a yellow color [80, p. 1029]. In Figure 2.12, we show the crystal and optical

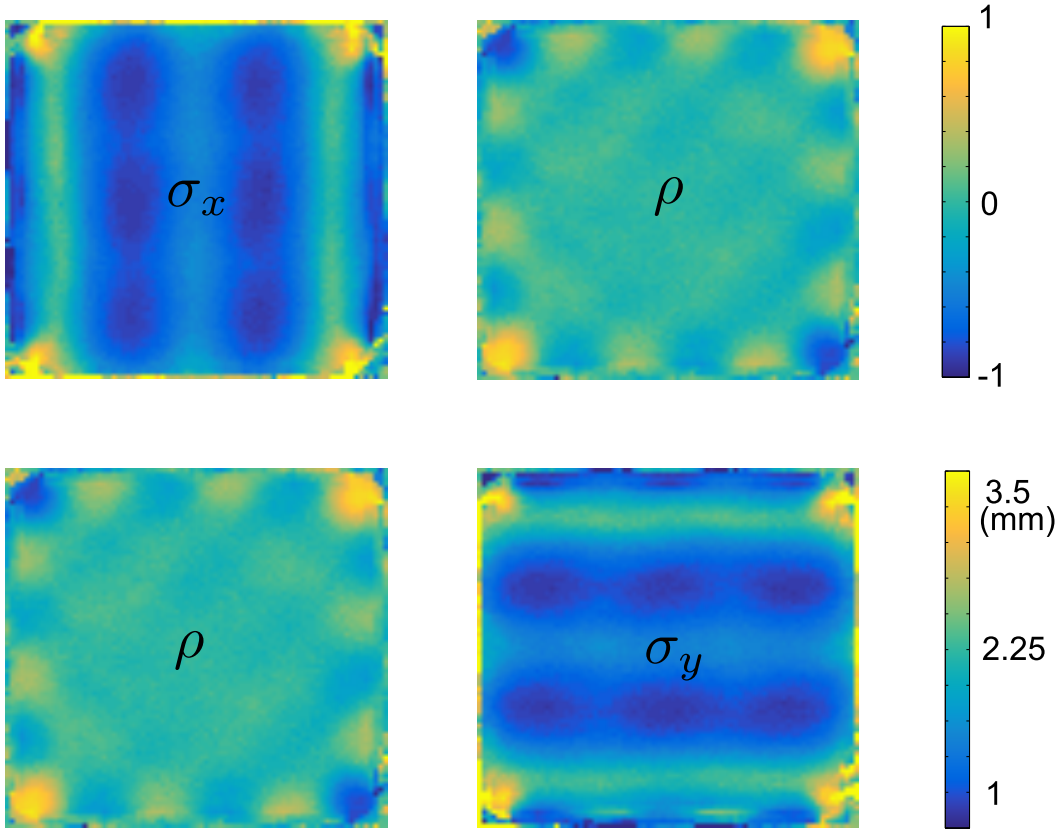

Figure 2.10: Representation of the detector covariance matrix. On the upper left, the FWHM along the x-axis, in mm, is represented across the detector face. On the bottom right, the FWHM along the y-axis, in mm, is represented. These two figures share the same color scale which is shown at the bottom, ranging from 1 mm to 3.5 mm. On the upper right and lower left, the covariance across the detector face is represented, along with the color scale at the top ranging from -1 to 1. These values are taken for camera SN15012101, currently camera 00 on AdaptiSPECT.

window of a FastSPECT II camera currently under repair. The yellowing appears to happen at the entrance face of the camera and seems most likely to happen on the edges of the crystal. The yellowed spots have a random size and distribution across the surface face though they tend to grow as disks. Fortunately, the yellowing is limited to the surface of the crystal and can be removed by polishing as shown in Figure 2.13.

A yellowed crystal will have a degraded light output, though the exact effect is

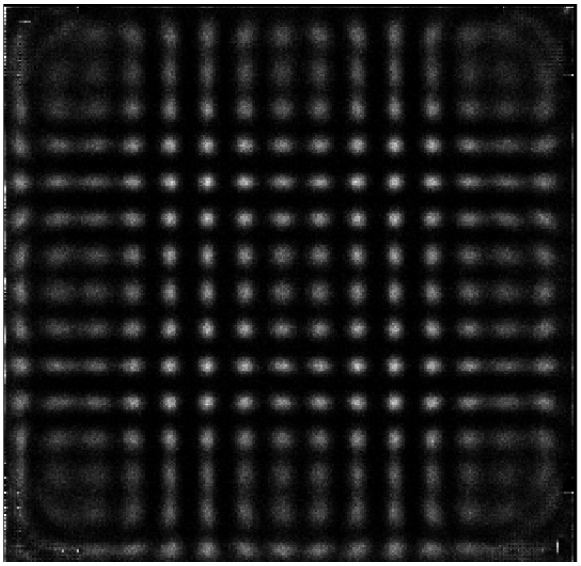

(a) Point grid array

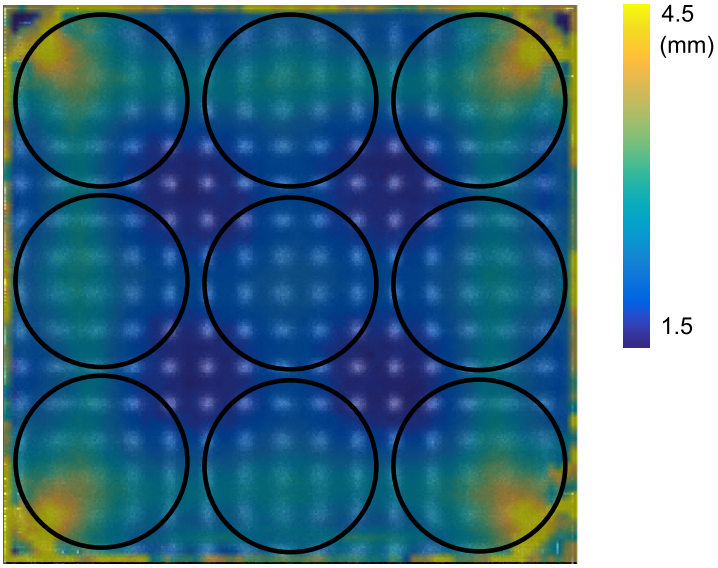

(b) Point grid array superimposed with variance

Figure 2.11: Point grid array extracted from the MDRF measurement. The points are 5 mm apart. In (b), we superimpose the point grid array with the total variance in mm of the detector and show a drawing of the approximate locations of the 9 PMTs.

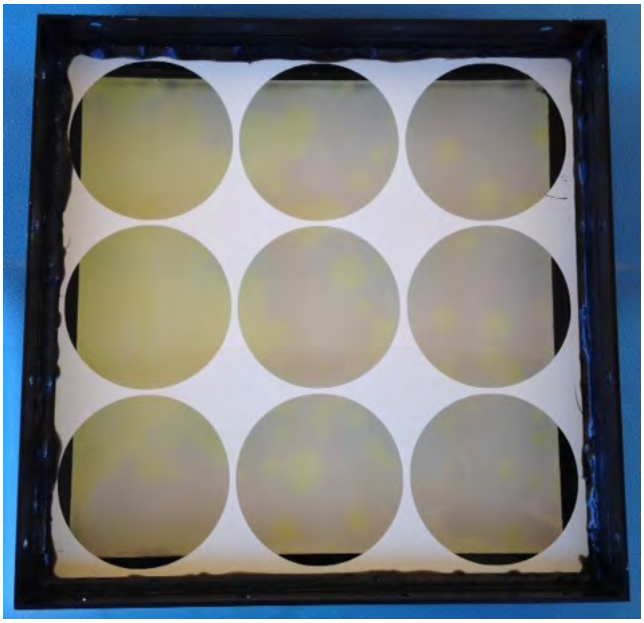

Figure 2.12: Photograph of a yellowed crystal from a spare FastSPECT II camera. The crystal is still in its housing behind the optical window. A large yellow spot is visible on the left edge and multiple smaller yellow spots are visible across the entire surface of the crystal. Photo courtesy Pier Ingram.

not very clear. It is likely, since the yellowing happens at the entrance surface of the crystal, that it affects the optical photons issued from the scintillation process. As we have stated in previous sections, the optical photons emitted when a gamma ray interacts with the crystal are emitted isotropically. Some will travel directly to the PMTs while others will first be reflected by the Lambertian reflector before being detected. Since the scintillation light is at 415nm, which is also the absorption wavelength of a yellow patch, the photons can be absorbed before, or just after, being reflected by the Lambertian surface. Some photons will not be absorbed, but overall, the light output for a location on the camera corresponding to a yellowed patch will be decreased.

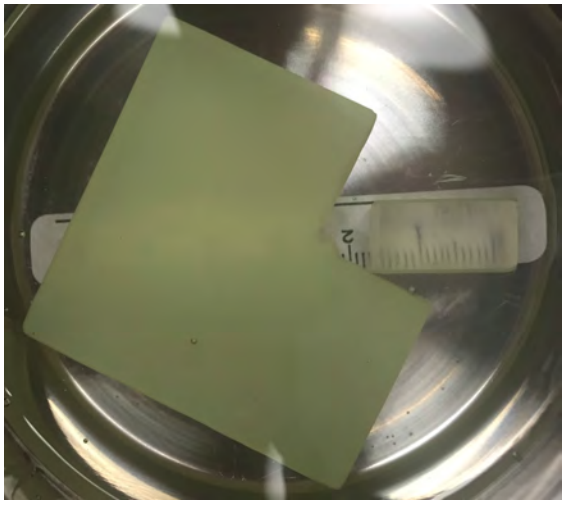

Figure 2.13: Photograph of a yellowed NaI:Tl crystal piece on the left and a small section of the same crystal after polishing the surfaces on the right. The improvement in light transmission is clearly visible. Photo courtesy Dr. Bora.

2.5.2 Consequences for the MDRF

This decrease in light output is very visible when comparing an MDRF taken on a detector with a yellowed crystal to an MDRF acquired on a detector that has a pristine crystal, as seen earlier in Figure 2.8. In Figure 2.14, we show the MDRF for a detector after it has yellowed. For all 9 PMTs, small dips in the response are visible, giving the MDRF its characteristic *swiss-cheese* look.

2.5.3 Consequences for ML positions estimation

Using an MDRF acquired after a crystal has yellowed leads to artifacts when performing maximum-likelihood position estimation. In Figure 2.15a, we show the binned projection of a 5-rod resolution phantom imaged through a pinhole using camera 01 on AdaptiSPECT. In Figure 2.15b, we show the corresponding MDRF (for illustration, showing the sum of all 9 PMTs). In both figures, we point arrows at artifacts, where the ML search algorithm attributes events and corresponding "dips" in the MDRF. The positioning algorithm described in equation 2.18 tends to find the maxima at these positions. This is visible in Figure 2.16 where we show the cross-

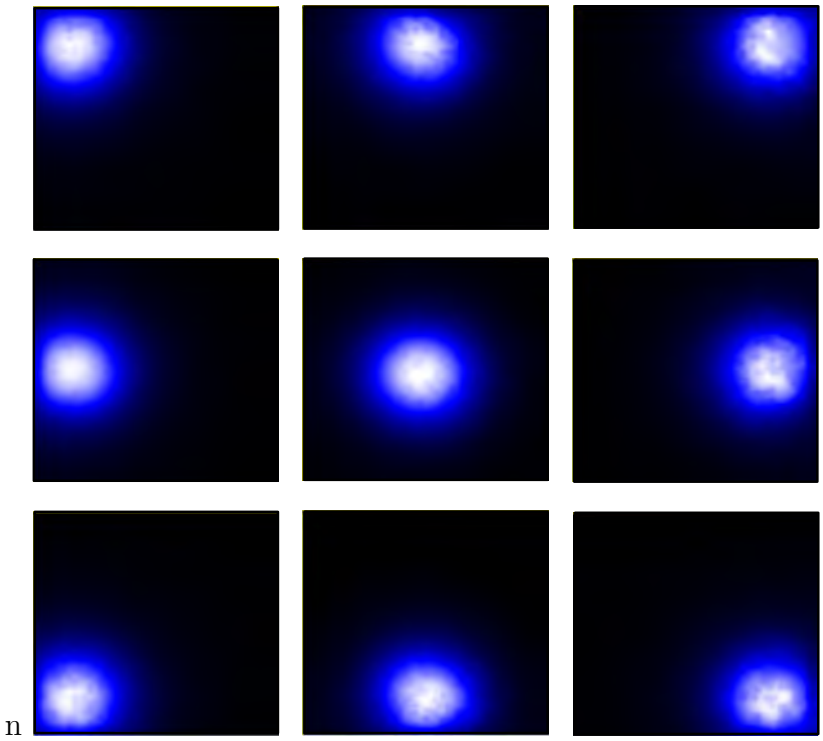

Figure 2.14: Example of an MDRF plot for a camera after it has yellowed. This is camera with serial number SN14062701, currently camera 01 on AdaptiSPECT. Each figure shows the response of one of the PMTs across the detector surface. The characteristic *swiss-cheese* dips are visible.

section along the x-axis of the MDRF from Figure 2.14 for tubes 08, and 07, along with the MDRF-dependent part of equation 2.18: $N_0 \ln\left(\overline{N}_j(x_d, y_0)\right) - \overline{N}_j(x_d, y_0)$. For the purpose of this demonstration, we try to estimate the location $x = 92$. For tube 08, this produces a mean number of photons $N_0 = 1396$, and for tube 07, this produces a mean number of photons $N_0 = 215$. The y-location, y_0 is fixed. As it can be seen in Figure 2.16a, for tube 08, the mean number of photons $N_0 = 1396$ corresponds to two possible locations, which results in two maxima in Figure 2.16c, at least for the curve produced using the original MDRF. The yellowed MDRF produces a flat section with multiple maxima. The ambiguity on the location of the maximum should be lifted when adding the maxima produced by other tubes. However, when the crystal has yellowed, the ambiguities may remain in the other tubes,

as it is illustrated in Figure 2.16d, where another flat section in the expression for the likelihood, this time for tube 07, can be seen. These flat sections correspond to parts where there is a "dip" in the MDRF, and the positioning algorithm is likely to attribute events to these locations. This is visible in Figure 2.15b where the artificial pile-ups correspond to the holes in the "MDRF".

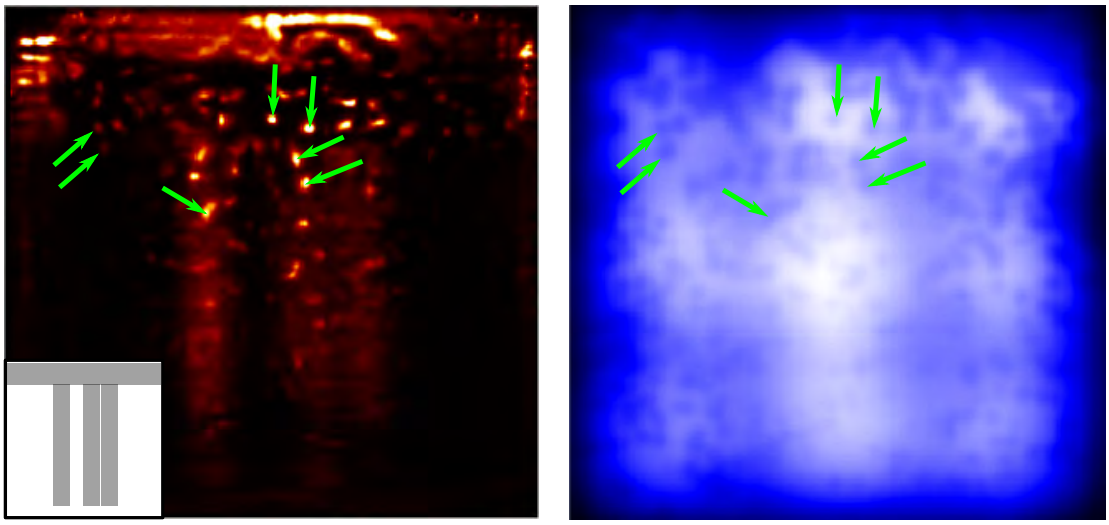

(a) Position Estimation (b) Corresponding MDRF

Figure 2.15: Position estimation results of a 5-rod phantom projected through a pinhole on a yellowed camera. The ML estimation shown in (a) is carried out using a MDRF measured after the crystal started yellowing. The corresponding MDRF is shown in (b). The green arrows point to artificial piling of events and the corresponding dips in the MDRF. At the bottom left corner of (a) we show a schematics of the expected projection.

2.5.4 Potential solutions

The main problem with using an MDRF acquired after yellowing is that the dips in the MDRF will create artifacts in binned bitmaps. One possible workaround is to smooth the MDRF until most dips disappear and then use the ML algorithm with the smoothed map. This leads to better positioning as shown in Figure 2.17c. It is also possible to use an MDRF acquired before the crystal yellowed, after re-processing it with the new gain values for the PMTs, in order to keep the same light

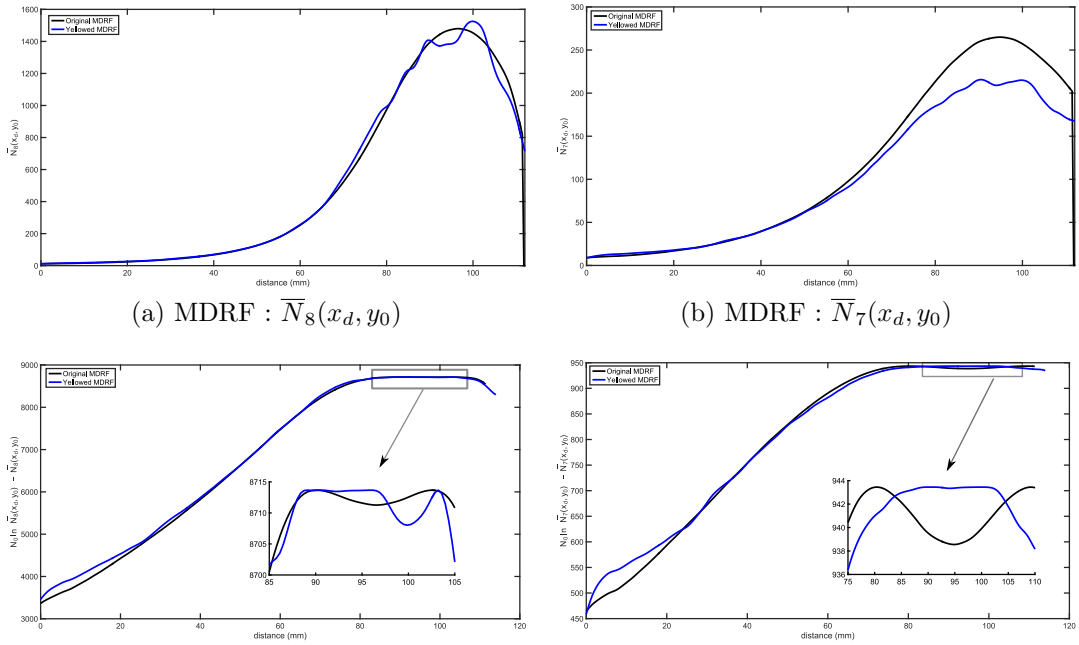

(a) MDRF : $\overline{N}_8(x_d, y_0)$ (b) MDRF : $\overline{N}_7(x_d, y_0)$

(c) $N_0 \ln\left(\overline{N}_8(x_d, y_0)\right) - \overline{N}_8(x_d, y_0)$ (d) $N_0 \ln\left(\overline{N}_7(x_d, y_0)\right) - \overline{N}_7(x_d, y_0)$

Figure 2.16: (a) Profile of the MDRF for tube 8 on camera 01. The MDRF acquired after the crystal has yellowed is compared to the MDRF acquired when the camera was first delivered. (b) Profile of the MDRF for tube 7 on camera 01. (c) Profile of the MDRF-dependent part of equation 2.18 for tube 8. The function acquired after the crystal has yellowed is compared to the function acquired when the camera was first delivered. A detailed view of the part of the curve where the maximum of the likelihood is reached is also shown. The original MDRF produces two maxima, the yellowed MDRF produces a flat section of the curve where a maxima may be harder to find. (d) Profile of the MDRF-dependent part of equation 2.18 for tube 7.

output scale. In Figure 2.16, we show the profile of the tube response of PMT 8 in camera 01, comparing the response acquired after the yellowing (visible irregularities along the curve) and the response of the MDRF acquired when the camera was first delivered but reprocessed with the new gain values. The two curves match well and the 2D position estimation is improved, as seen in Figure 2.17b. Alternatively, a smooth polynomial shape could be fitted to the yellowed MDRF and used for position estimation though this was not performed in this work.

To compare various methods of estimating the interaction position after a crystal

has yellowed, we processed the raw data acquired from a 5-rod phantom imaged through a pinhole with camera 01 on AdaptiSPECT using three different methods: the MDRF acquired after yellowing, the MDRF acquired before yellowing but scaled to accommodate new values for the gains, and the smoothed MDRF acquired after yellowing. In Figure 2.17 we show the results of these three methods. Qualitatively, using the old MDRF outperforms the other two methods but reveals some dark spots on the edges of the camera. Smoothing the MDRF leads to the next best results, but still presents some artifacts.

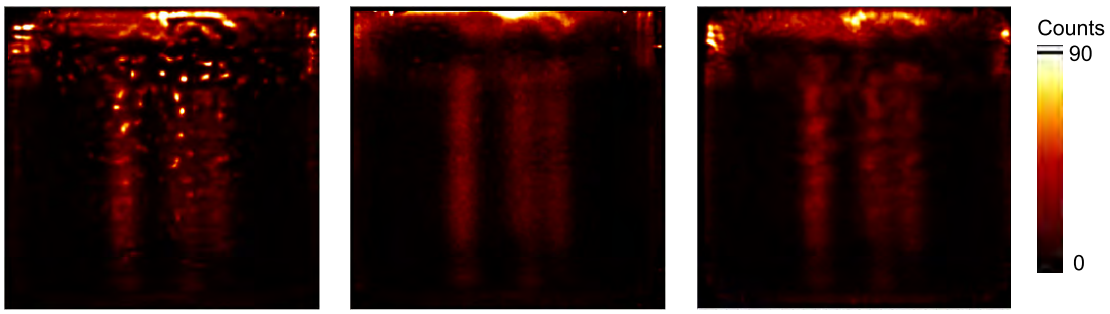

(a) with recent MDRF (b) with old MDRF (c) with recent MDRF, smoothed

Figure 2.17: Result of 2D ML position estimation of a 5-rod phantom projected through a pinhole of AdaptiSPECT. In (a), the ML algorithm is carried out using an MDRF acquired after the crystal has yellowed. In (b), the ML estimation is performed with the MDRF acquired right after arrival of the camera, before the crystal yellowed. In (c), the ML estimation is performed using the recent MDRF, after smoothing it. The position estimation performs better with the original MDRF, but some dark spots are seen on the top of the projection where a pool of activity should be observed.

It is our opinion that the only way to address the yellowing problem is unfortunately to disassemble the camera, clean and polish the crystal, and re-seal the ensemble. The way the modular camera is designed, with its Lambertian reflector to improve the ML position estimation, is not at all tolerant of yellowing.

2.6 Cameras on AdaptiSPECT

In this chapter, we have reviewed the basic physics behind the detectors used on AdaptiSPECT, as well as the calibration of these detectors and the ML-positioning algorithm. We have also discussed the unfortunate detector-yellowing problem and a method to allow use of those detectors until they are repaired. AdaptiSPECT comprises 16 modular cameras, like its predecessor FastSPECT II [66], that are arranged into 2 rings of 8 detectors, with a 45 degree angle between adjacent detectors on each ring. The back ring is rotated at 22.5 degrees relative to the front ring. This allows a complete sampling of the field of view in addition to dynamic imaging. Contrary to FastSPECT II, whose detectors are fixed with respect to the center of the field of view, the detectors on AdaptiSPECT can move continuously from 165.1mm from the center of the field of view to 317.5mm. Each detector is mounted on a translation stage and can be moved radially independently from all other detectors. A rendering of the detector arrangement of the system is shown in Figure 2.18.

Figure 2.18: Solidworks^{TM} rendering of the AdaptiSPECT gantry. The front ring of 8 detectors is visible. The translation stages which allow the radial translation of each detector are also visible.

CHAPTER 3

Adaptive Aperture

The detectors described in the previous chapter do not determine the system resolution and field of view by themselves. To predict and understand the system imaging characteristics, the imaging aperture must also be included. For small animal imaging, pinhole apertures are usually used since they enable high magnification and high resolution [24, 84]. The adaptive aperture developed in this work follows the fundamental pinhole-imaging principles that have been reviewed in various papers and book chapters [63, 104, 155]. The main difference between the adaptive aperture in AdaptiSPECT and other multicamera, cylindrical-style collimators developed in the past is that the AdaptiSPECT aperture consists of three different apertures cylinders stacked end-to-end along the imager axis. This allows one to change the pinhole diameters and pinhole-to-object distances without interrupting the imaging session to replace hardware. This chapter reviews the principles of aperture design before describing the design and fabrication of the adaptive aperture.

3.1 Basis of pinhole apertures

The imaging properties of a pinhole SPECT system depend on the size, number, orientation, and shapes of the pinholes used as much as on the size and intrinsic resolution of the detectors. Furthermore, the material used to manufacture the pinholes, and even the manufacturing technique itself, can impact the capabilities of the final imaging system.

3.1.1 Sampling of the Field of View

The field of view of a SPECT system is determined by the size of the detectors in combination with the dimensions and positions of the pinholes. Some systems

have moving hardware to achieve the desired number of views, others can move the subject to increase the field of view, and others are stationary systems, that allow for dynamic imaging. An important part of designing a pinhole collimator is to ensure that the resulting field of view is sampled properly by the number and angular orientation of the projection images. A proper sampling is usually defined as a sampling that will lead to an artifact-free reconstruction of the object inside the field-of-view, though one could imagine a different definition when using task-based principles. In that case, one could define an appropriate sampling as any one that will accomplish the task at hand. The sampling of the field-of-view is determined by the number of detectors (or detector positions for systems with moving parts), the number of pinholes and their imaging shapes, as well as whether or not the field of view is being scanned during an acquisition.

A traditional requirement to ensure adequate sampling of a field of view is to make sure that there is enough angular sampling, a condition previously derived by Orlov [130], under the assumption of a linear reconstruction process. In practice, it is very difficult to meet the Orlov conditions with a stationary system such as AdaptiSPECT, but the sparsity of the objects being imaged compensates for the lack of views, making it nevertheless possible to reconstruct them very well with iterative reconstruction methods that enforce positivity [46]. In addition to angular sampling, it is important to have sufficient axial sampling, a condition that has been shown by Tuy to be unachievable except in the central slice [154], again assuming a linear reconstruction. However, with respect to this limitation, Mok et al. [124] and Vanhove *et al.* [160] have shown that it is advantageous to design multi-pinhole collimators such that each pinhole focuses on a different slice of the field of view. One approach for adequate sampling is to make sure that the field of view is sampled as uniformly as possible. Voxels in the field of view that are sampled less often than others will have a fewer counts and thus create higher noise in the reconstructed images.

3.1.2 Resolution and sensitivity

The shape of the pinholes chosen for a SPECT system impacts the final achievable resolution. The most common shape, the knife-edge pinhole, is shown in Figure 3.1a and is relatively easy to machine, however, the small thickness around the pinhole opening results in additional gamma-ray penetration and leads to a larger effective diameter, causing a reduction in the final resolution. It is possible to reduce the penetration by using a different shape, such as the keel-edge shown in Figure 3.1b. This improves resolution over a knife-edge pinhole for higher energies but may require wider acceptance angles to avoid vignetting [149]. Other shapes have been proposed to reduce penetration such as truncated pinholes [96] and clustered pinholes [70], where a pinhole is divided into multiple smaller pinholes.

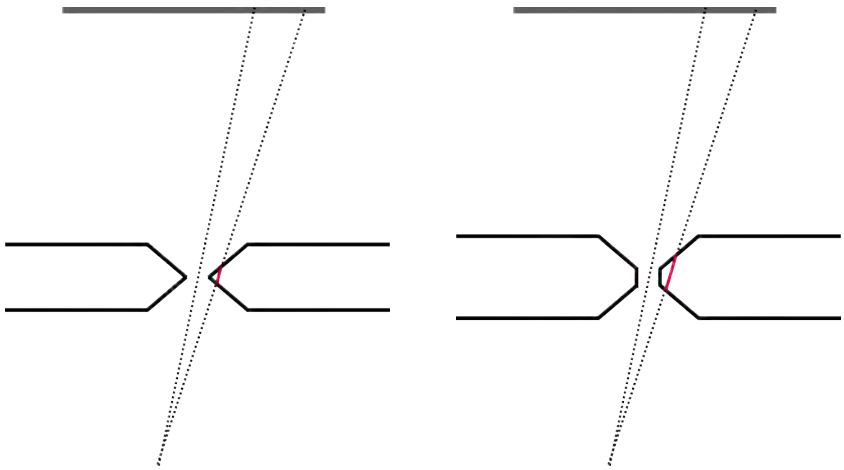

(a) Knife-edge pinhole (b) Keel-edge pinhole

Figure 3.1: Pinhole shapes: the keel-edge design in (b) has less penetration around the pinhole than the knife-edge design in (a) but may suffer from vignetting at the edges of the field of view.

Figure 3.2 shows the variables that define a pinhole, which include its opening diameter d, opening angle α, its distance to the object h, and its distance to the detector L. The geometry-derived resolution and sensitivity of a pinhole collimator have been worked out by Paix [131] and Metzler et al. [110], and for any point inside

the field of view, the resolution is given by:

$$R(L,\theta) = \sqrt{\frac{R_{\text{det}}^2}{[m(L,h)]^2} + \left(d_{R,\text{eff}}(L,\theta)\left(1 + \frac{1}{m(L,h)}\right)\right)^2}, \tag{3.1}$$

where R_{det} is the intrinsic resolution of the detector used, $d_{R,\text{eff}}$ is the effective pinhole diameter corrected for additional penetration, and $m(L,h)$ is the magnification, given by:

$$m(L,h) = \frac{L}{h}. \tag{3.2}$$

In most SPECT imaging systems, the distance of the pinhole to the detector, L, is fixed, and therefore the magnification inside of the field of view varies only with the distance of the pinhole to the object h. However, in AdaptiSPECT, L is also variable.

The effective pinhole diameter has been derived by Accorsi and Metzler [5], and is given by:

$$d_{R,\text{eff}} = d + \frac{\ln 2}{\mu}\left(\tan\frac{\alpha}{2}\right), \tag{3.3}$$

where μ is the absorption coefficient of the material used to manufacture the pinhole at the energy of the gamma ray, and α is the opening angle of the pinhole.

The sensitivity of the pinhole collimator is given by:

$$S(h,\theta) = \frac{d_{S,\text{eff}}^2 \sin^3\theta}{16h^2}, \tag{3.4}$$

where h is the normal distance of the point source to the plane of the pinhole and θ is the angle of incidence from the plane of the pinhole to the point source. When using this convention, $\theta = \pi/2$ for a normal incidence angle. The effective pinhole diameter for the sensitivity computation has been derived by Metzler et al. [110], and is given by:

$$d_{S,\text{eff}} = \sqrt{d\left(d + \frac{2}{\mu}\tan\frac{\alpha}{2}\right) + \frac{2}{\mu^2}\tan^2\frac{\alpha}{2}}. \tag{3.5}$$

The sensitivity of a single pinhole collimator is very small, which is why multiple pinholes are now often used. For example, a system can be built with multiple detectors each having a single dedicated pinhole per detector as is the case for

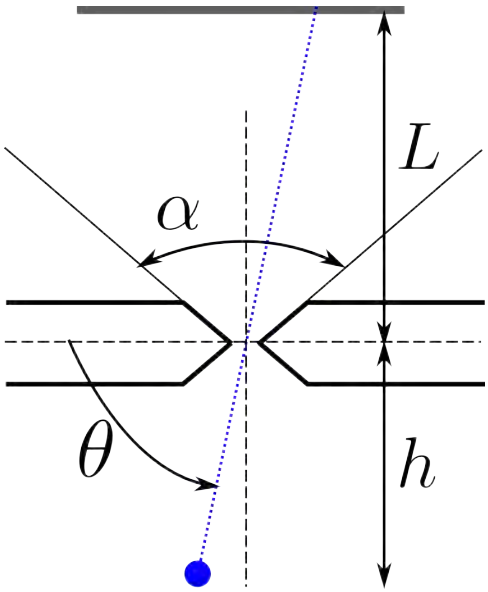

Figure 3.2: A pinhole is described by its opening angle α and its distance to the detector L. A point inside of the field of view can be described by its normal distance to the plane of the pinhole h and its angle with the plane of the pinhole θ.

both FastSPECT II [66] and the single-pinhole configuration of AdaptiSPECT. It is also possible, when using larger detectors, to design a collimator such that multiple pinholes project onto the same detector as done in the U-SPECT [26] and NanoSPECT [143] systems. When multiple pinholes project onto the same detectors, it is possible to design the pinholes such that the projections will either never overlap (U-SPECT), or allow for some overlapping (NanoSPECT). Overlapping is called multiplexing, and we will discuss it further in section 3.1.3.

Pinhole collimators are not the only possible way to form images in emission tomography. Among other techniques successfully used are coded apertures, which were first used in astronomy, and can be described as highly-multiplexed multi-pinhole apertures [4, 18, 68, 103, 105, 138, 151]. Another technique involves crossed slit collimators where a pinhole is replaced by two or more slits arranged at 90 degrees. The imaging properties are then set by the width of the slits and the distance from the slits to the object and detector, which can be different in the transaxial directions to make "anamorphic" projections [6, 22, 57, 58, 87, 152]. Other

approaches include parallel-hole or converging-hole collimators, rotating slats [173], linearly scanning slits [172], and variations thereof.

3.1.3 Multiplexing

Multiple-pinhole collimators can be designed such that there are no projections overlapping on the detector (no multiplexing), or such that there is some degree of overlapping (multiplexing). Multiplexing has the advantage of increasing the sensitivity of a system, but comes at a possible cost of reduced image quality as it is now impossible to determine exactly which pinhole a given photon passed through if it is in a multiplexed part of the projection. This increased uncertainty can create artifacts in the reconstruction [123].

A few studies have tried to assess whether the benefits of multiplexing outweigh the disadvantages, with mixed results. Vunckx *et al.* showed that multiplexing did increase the sensitivity of the system they were studying, but did not lead to any benefits in terms of contrast-to-noise ratio [164], a fundamentally flawed image-quality metric that nonetheless persists in the medical imaging literature. Their conclusion was that the added sensitivity might only just compensate for the increased complexity of the system. In another study, Mok *et al.* showed that sparse objects would benefit more from multiplexing than non-sparse ones [123]. The benefits of multiplexing in terms of detection or estimation tasks were first evaluated by Hesterman who found improved performance with a combination of multiplexed and non-multiplexed images [75].

Two main approaches have been explored to produce artifact-free reconstructions with multiplexed projections. The first way is to design the collimators with no or carefully controlled symmetries such that the reconstruction shows as few artifacts as possible. It has been shown in multiple cases that irregular pinhole patterns are less likely to cause artifacts in the reconstruction than regular pinhole patterns [32, 56, 75, 163]. The other way to address this problem is to perform reconstructions with combined datasets from both multiplexed and non-multiplexed projections. Vunckx *et al.* used a single-pinhole collimator and a dual-head detector to acquire

two datasets with different degrees of multiplexing [163] while Mahamood *et al.* used a slit-slat collimator with multiplexed and non-multiplexed projections [98, 99]. In both studies, the combination of multiplexed and non-multiplexed data reduced the artifacts in the reconstruction and improved the contrast-to-noise ratio. In some systems, the non-multiplexed data is already available when only part of the detector is used with overlapping projections. If there is enough non-multiplexed data, then it is possible to reconstruct artifact-free images without acquiring a separate additional dataset [95, 156].

Finally, multiplexing can be used with projections acquired at different detector distances in a process called "synthetic collimation". Originally proposed by Wilson *et al.* [170], this technique enables a tomographic reconstruction of an object without rotating a detector-pinhole assembly by acquiring many focused-pinhole projections on a single high-resolution detector. At small collimator-detector distances, the magnifications are small and the images non-multiplexed. At further distances, the images overlap. A few systems have been successfully designed using this principle. An example is the SiliSPECT system developed at Vanderbilt University, which uses two detectors positioned at different distances from the same collimator [146, 147]. A synthetic SPECT system was also designed and built at the University of Arizona by Havelin et al. [72], and uses one highly multiplexed aperture with a single detector mounted on a translation stage to acquire projections at different pinhole-to-detector distances.

The AdaptiSPECT aperture has been designed to allow for both multiplexed and non-multiplexed data to be acquired. To our knowledge, it is unique in the sense that the switch from one configuration to another is extremely simple, fast, and can be entirely automated. AdaptiSPECT will therefore become a platform to research how different methods of combining multiplexed and non-multiplexed data can improve system performance in terms of detection and estimation tasks.

3.1.4 Fabrication techniques

Pinhole collimators are manufactured in high-density, high-atomic-number materials to stop unwanted high-energy photons. The most commonly used materials are lead (Pb), tungsten (W), gold (Au), and platinum (Pt). Since gold and platinum are expensive, they are mostly used to manufacture pinhole inserts, while the body of the collimator is usually manufactured in lead or tungsten. Lead is more often used than tungsten, despite its lower density (11 g/cm^3 for lead vs 19.3 g/cm^3 for tungsten), because it has a low melting point and is therefore much easier to cast than tungsten.

Two recent manufacturing techniques have been introduced successfully to the tools for collimator manufacturing. The first technique is the cold casting of apertures using tungsten powder mixed with epoxy. This technique produces collimators of a density around 9 g/cm^3 [117] and should therefore be used in combination with inserts made of higher density materials. The collimator in FastSPECT III, for instance, uses this technique in combination with pinholes manufactured in a platinum alloy using a lost-wax casting technique [114, 117]. In the original AdaptiSPECT design, this technique was proposed for its aperture fabrication but it proved to be impractical due to the large size causing distortions in the molds during the heavy casting phase. Nevertheless, some parts of the system, such as the aperture shroud, were manufactured using the relatively inexpensive cold casting [117].

The second technique now available is additive manufacturing with metal powder. It is now possible to "3D-print" parts directly in tungsten, with a laser that selectively melts tungsten powder layer by layer to produce the desired shapes. This technique has already been successfully used to manufacture a collimator [54] with a density of 18.5 g/cm^3 and a precision of $\pm 35\mu$m in each direction [155]. This technique has the additional advantage of being somewhat MR-compatible, which is not the case of apertures machined in tungsten alloys that often contain ferrous components. The AdaptiSPECT collimator makes use of this recently developed manufacturing technique.

What is most remarkable about these two novel techniques is that by allowing very complex shapes to be manufactured by adding material, many collimators that could not be made by removing material from a solid blank are now feasible.

3.2 Design of the Adaptive Aperture

The design of the adaptive aperture has evolved over four years. The original design was made by Furenlid *et al.* in 2008 [65], and refined in 2010 by Van Holen *et al.* [159] The cold casting technique for manufacturing was proposed but the design did not include the mechanical components necessary for the adaptation. The design was modified again in 2012 to allow more room for animal imaging [38]and at this same time the mechanical design for the aperture motion was finished. The manufacturing method for the aperture was changed to machined tungsten alloy with additive manufacturing for the pinholes themselves in 2013 and the construction drawings were finalized in 2014 [36, 37].

The AdaptiSPECT collimator consists of 3 rings of pinholes, where each ring is designed to yield a different magnification and field of view when translated into the imaging position, in order to accommodate different imaging subjects and imaging tasks. The collimator is thus axially segmented into different diameter sections such that for each ring segment the pinholes are at a unique fixed distance from the center of the field of view. Placing the desired ring segment into the imaging position for a particular application is achieved by translating the full imaging aperture. The collimator has one pinhole per detector, for a total of 16 pinholes always open per magnification, though the mid-magnification and low-magnification rings can be switched from a single-pinhole-per-camera configuration to a five-pinhole-per-camera configuration to increase the sensitivity at the expense of multiplexing. A rendering of the aperture is shown in Figure 3.3.

The main constraint in the design of the aperture derives from the intended imaging application of each ring of pinholes. The smallest diameter ring segment (high-magnification) is sized for mouse studies. The diameter of the high-magnification

ring is sized such that any organ in a 20g-30g mouse can be placed in the center of the field of view while the ring's length is long enough to permit whole-body scans. Similarly, the diameter of the middle ring segment (mid-magnification) is sized such that any organ of a 250g rat may be placed in the center of the field of view with the segment length again being long enough to allow for whole-body rat scans. The spacing between the ring segments is set such that no leakage occurs through the pinholes of other rings while one ring is in the imaging position, and when one ring segment is in the imaging position, the other ring segments are covered by a shroud.

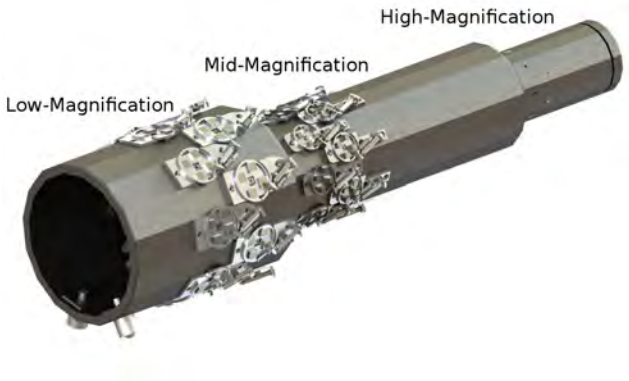

Figure 3.3: CAD rendering of the pinhole aperture showing the three ring-segments, the shutters, and some of the motion controllers.

3.2.1 Imaging Properties

The constraints due to the sizes of the animals described above have a direct impact on the distance of the pinholes to the center of the field of view. It is tempting to reduce this distance to increase magnification, but this would reduce the ability to position the animal inside the collimator. Keeping these limitations in mind, we used ray tracing methods to compute the sensitivity, magnification, resolution, and field of view of the system for various designs. The ray-tracing software was developed by Dr. Roel Van Holen and is based on the Siddon algorithm [148] and Equations 3.1 and 3.4. For each pinhole, 456 rays were traced to compute the imaging properties of the collimator [159].

	Low-M	Mid-M	High-M
pinhole distance (mm)	76.2	50.8	26.1
pinhole diameter (mm)	1.5	1	0.6
total length (mm)	140	315	140

Table 3.1: Aperture dimensions. The pinhole aperture consists of three ring segments: low-magnification, mid-magnification and high-magnification.

The final dimensions of each aperture ring segment are summarized in Table 3.1 and the geometric imaging characteristics achieved with each segment are presented in Table 3.2. With this design, the magnification of the system ranges from $\times 1$ to $\times 11$, the resolution ranges from 700 μm to 3 mm, and the transaxial field of view ranges from 10 mm to 90 mm. The resolution predicted is often surpassed in real applications since a well-calibrated statistical reconstruction algorithm such as ML-EM has a certain degree of resolution recovery built in [23, 132].

Imager Configuration	Low-Mag		Mid-Mag		High-Mag	
detector distance (mm)	165.1	317.5	165.1	317.5	165.1	317.5
magnification	1.2	3.2	1.7	4.2	5.3	11.1
resolution (mm)	3.48	1.95	2.40	1.60	0.8	0.7
transaxial FOV (mm)	90	37.5	48	24	20	10.5

Table 3.2: System properties of AdaptiSPECT. Since the detector distance to the central axis is variable from 165.1 mm to 317.5 mm, each pinhole-ring has a range of magnifications, resolutions, and fields of view.

3.2.2 Design and Fabrication of the Adaptation Controls

Design Constraints

The total travel distance required to move the three separate ring segments — low-, mid-, and high-magnification — into the imaging position is 370 mm. There are three mechanical requirements on the design of the motion system:

- The entry into the low-magnification ring segment of the aperture has to remain clear since this is the end where an animal is inserted into the aperture

when imaged in AdaptiSPECT. Therefore, the aperture motion has to be driven from the high-magnification segment.

- The aperture has a mass of 43 kg and its center of gravity is located within the low-magnification ring-segment. Therefore, it is necessary to support the aperture from the low-magnification end to avoid sag.
- The linear translation of the aperture must provide high-precision placement and excellent repeatability in order to maintain the validity of the measured calibration.

Design of the motion controls

On the high-magnification side of the aperture we have chosen to use a Velmex stage that has 508 mm of travel. We designed a holder that bolts on to the Velmex stage and an arm that is clamped in the holder. The arm is fastened to the aperture using spring-loaded bolts which allows for some flex when driving the motion so that the assembly is not overdetermined and consequently stressed. A CAD rendering of this motion system is shown in Figure 3.4a.

On the low-magnification end, we support the aperture and guide it during its motion with two SKF ball transfer units that are directly threaded into the aperture. They are adjustable in height and therefore allow for correct horizontal alignment of the aperture. The two ball transfer units run on precision-ground stainless steel rails, one of which is a plain rail and the other which has a v-groove that defines the linear trajectory of the aperture in what is known as a kinematic-3-point support. The ball transfer units are mounted at a 45 degree angle relative to each other to provide stability. A CAD rendering of this system is shown in Figure 3.4b.

3.2.3 Design of the shutters

To enable easy conversion between the single-pinhole-per-camera configuration and the five-pinhole-per-camera configuration, we have designed shutters consisting of four tungsten blocks glued to a circular plate that rotates in a fixed mount (see

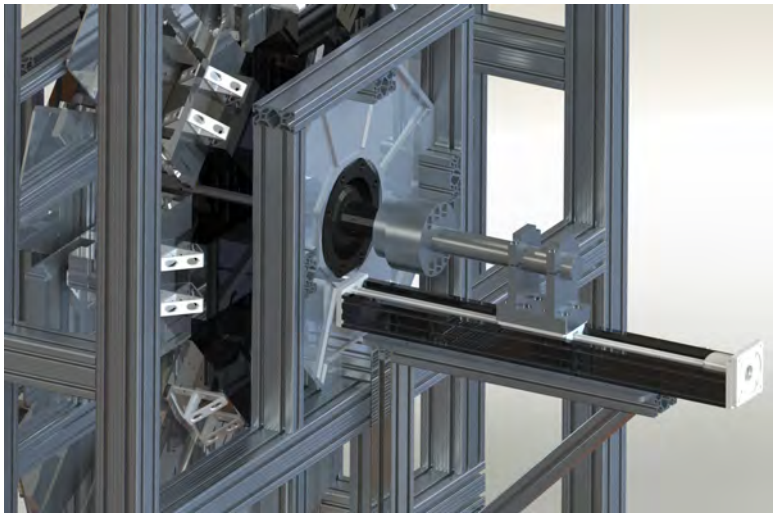

(a) CAD rendering of the aperture support and motion control on the high-magnification ring segment side.

(b) CAD rendering of the aperture support and motion system on the low-magnification ring segment side.

Figure 3.4: CAD rendering of the aperture support and motion controls for (a) the high-magnification end of the aperture, where the motorized stage driving the motion is located, and (b) the low-magnification end of the aperture where the ball-bearings and linear rails that guide the motion are located.

Figure 3.12). This assembly is directly mounted on the aperture above a group of five pinholes arranged in a quincunx pattern. The rotation of the circular plate enables the covering or uncovering of the four peripheral pinholes to switch between

configurations. A miniature air piston from Clippard Minimatic is used to actuate the circular plate into the open configuration. Pneumatic actuators have high reliability and are less prone to failure than miniature solenoids. The return of the plate to the closed position is driven by a spring. This design has a very low profile to accommodate the small space between the aperture and the shrouds that block gamma-ray leakage.

The shutters are mounted individually on the aperture in the same orientation. This way, the tubing necessary to actuate the air pistons are all directed towards the high-magnification ring segment of the aperture in order to leave the animal-handling side of the aperture unimpeded.

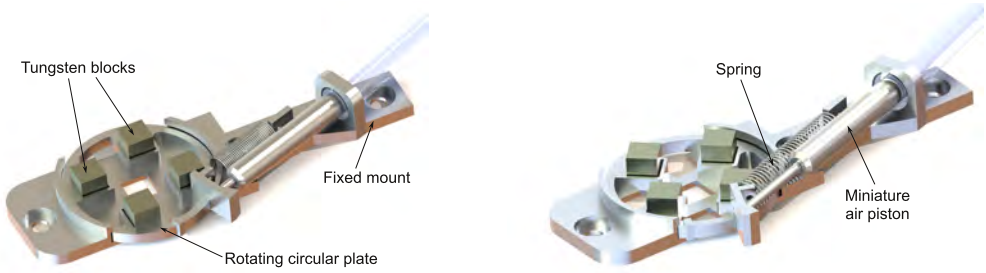

(a) Single-pinhole configuration (b) Five-pinhole configuration

Figure 3.5: Rendering of the shutters for the mid-magnification ring-segment. (a) Single pinhole-per-camera configuration. The piston is not actuated and the four peripheral pinholes are covered by tungsten blocks. (b) Five pinhole-per-camera configuration. The actuated piston pushes the circular plate and opens the four peripheral pinholes.

3.3 Fabrication of the Aperture

The aperture for AdaptiSPECT imposed challenging design and manufacturing requirements. In addition to the precise placement of the pinholes, the body of the aperture needs to be able to support its own weight. The pinholes themselves are designed to taper from a circular hole to a square opening that matches the detector area (this is also called a "lofted pinhole", or "lofthole" [53]). These kinds of shapes can be realized only with a 3D-printing-based additive manufacturing technique.

We first designed the aperture to be cast in a tungsten-epoxy composite with pinhole inserts cast in platinum. This method was successfully used to manufacture the aperture in FastSPECT III [116] and has been described by Miller *et al.* [117] In this technique, a plastic mold is created using a rapid prototype printer and a tungsten-powder-epoxy-resin is poured into that mold and left to cure. Unfortunately, the large size of the molds that were created for the AdaptiSPECT aperture led to poor results because the high weight of the tungsten epoxy deformed the mold slightly during the casting process. This led to imprecise pinhole placement, as shown in Figure 3.6. We concluded that the AdaptiSPECT aperture was too large to successfully use this simple method.

We therefore proposed a new manufacturing technique [36] utilizing conventionally machined tungsten alloy parts for the body of the aperture, but incorporating tungsten inserts created using additive manufacturing. To implement this, we first tested the approach by manufacturing the high-magnification part of the collimator. Because there is only one pinhole per detector in this section, this is the smallest and easiest part to manufacture. Next, we manufactured one segment each of the mid-magnification and low-magnification parts of the collimator to verify our pinhole designs. Finally, after validating the design and productions method, we manufactured and assembled the rest of the aperture. This three-step approach enabled us to limit our risks when manufacturing the aperture (*i.e.* if a design revision were required during either of the first two stages, the cost would not have been nearly as high as re-manufacturing the whole aperture).

Similarly, we first designed the shutters that enable the conversion between one and five pinhole-per-camera configurations on the mid- and low-magnification parts of the aperture to be manufactured using a 3D-printing approach. However, this soon proved to be impractical because the material in the 3D-printed parts had an unacceptably-high friction coefficient. We therefore re-designed the parts and manufactured them using materials used in plastic bearings.

(a) (b)

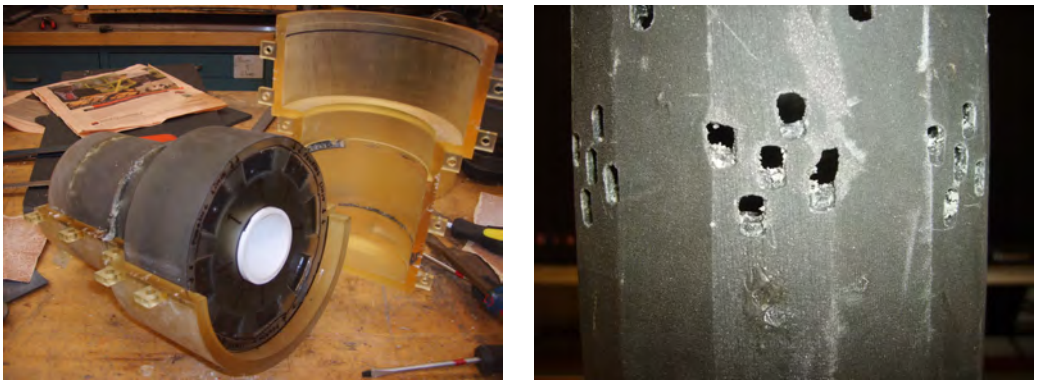

(c) (d)

Figure 3.6: (a) A mold manufactured for the aperture before pouring the tungsten powder into it. (b) Mold after casting. (c) Opening of the mold. The hard outer plastic shell is apart while the soft plastic shell is still attached to the cast aperture. (d) Aperture after being released from its mold. The pinhole emplacements are larger than designed and show the limitations of the cold-casting technique.

3.3.1 Aperture body and pinholes

With the new manufacturing technique, the body of the aperture was machined using a tungsten alloy while the pinholes were 3D-printed in tungsten powder. Since it would be very expensive to machine the aperture from a single block, we designed it as an assembly of plates that are bolted together in a barrel-like fashion around a cylindrical core. By using circular end plates of different diameters, it is very easy to transition from one diameter of aperture to another. Furthermore, by designing parts of the aperture as an ensemble of identical plates, machining becomes simple and efficient. In fact, most of the aperture plates can be manufactured in a single pass on a Computer Numerical Control (CNC) mill, reducing the time and cost of fabrication. The design of the plates is also simplified because we only need to design two plates per aperture section: one for the cameras in the front ring, and one for the cameras in the back ring. Finally, by having a barrel-like structure made with overlapping tungsten plates, we ensure that there are no seams with direct sight lines passing through the aperture, greatly reducing the risk of gamma-ray leakage.

Aperture parts: plates and pinholes

Figure 3.7 shows a plate manufactured for the high-magnification part of the collimator along with the lofthole pinholes. The pinholes were manufactured by 3D Systems LayerWise [1] using an additive manufacturing technique. The plates were machined in the University of Arizona on a CNC using a machinable tungsten alloy with 90% tungsten. The screws used to bolt the plates on the cylindrical holder were also machined in a tungsten alloy.

Figure 3.8 shows the pinhole plates manufactured for the mid-magnification and low-magnification sections of the aperture. The tapering from circle to square is clearly visible. In Figure 3.9, we show the test plates, pinholes, and shutters manufactured to test the mid- and low-magnification sections of the collimator.

In Figure 3.10 we show the assembly of the high-magnification part of the collimator. The barrel-like arrangement of the machined plates is clearly visible. Also

(a) Pinholes for the high-magnification part of the aperture

(b) Machined plates along with their machined screws

Figure 3.7: (a) Pinholes manufactured for the high-magnification part of the aperture are shown. The pinholes are manufactured by 3D Systems Layerwise using an additive manufacturing technique. The pinholes are then inserted into the plates shown in (b). Both the plates and the screws that attach the plates to the cylindrical holders are machined using a machinable tungsten alloy.

visible is the circular disk on which the mid-magnification part of the aperture is now bolted.

Leakage Tests

In the manufacturing technique described here, there are two main risks for leakage: first there is a chance of leakage where the plates are joined together, and second, there is a chance of leakage where the pinholes are inserted. We conducted two leakage tests on the aperture. In the first test, we joined together three adjacent plates and placed a pinhole in the central one. We acquired a planar x-ray image of

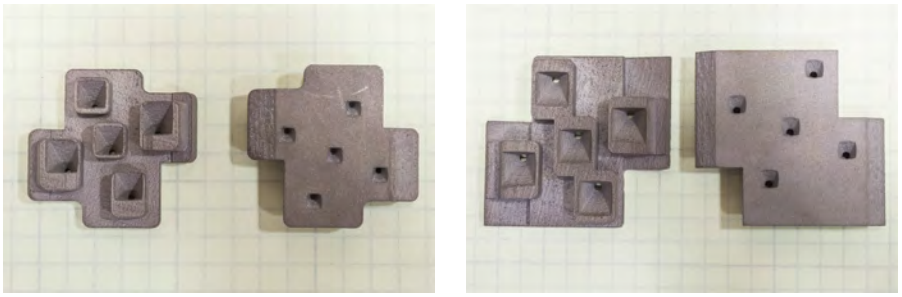

(a) Mid-magnification pinholes (b) Low-magnification pinholes

Figure 3.8: Pinhole plates manufactured for the mid- and low-magnification sections of the collimator.

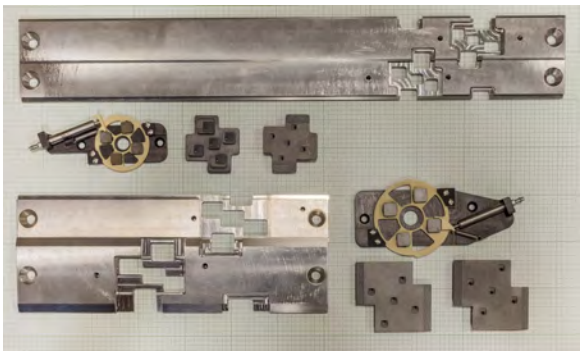

Figure 3.9: All the parts manufactured to test the mid- and low-magnification section of the collimators. Shown are two plates for both ring-segments, two 3D-printed pinhole for both segments, and a mid-magnification and low-magnification shutter assembly.

this assembly, using the Faxitron x-ray machine, at 60KeV, with 5 minutes exposure, and compared the attenuation from a part with no pinhole to a part with a pinhole. No leakage was detected at the place where the plates are joined. In the second test, we used the completed high-magnification part of the aperture with its pinholes inserted and placed a ^{99m}Tc point source at the center of the collimator. We then recorded counts coming out of a pinhole using one of our detectors. No leakage was found from the places where the plates join nor from the places where the pinholes are inserted. The results of these leakage tests are shown in Figure 3.11. These tests were successfully repeated on the mid- and low-magnification test parts.

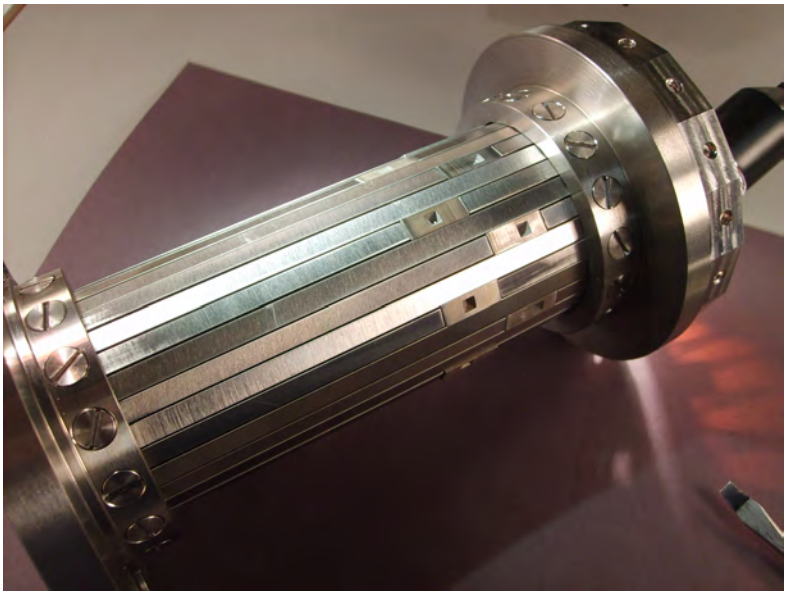

(a) Assembled high-magnification collimator

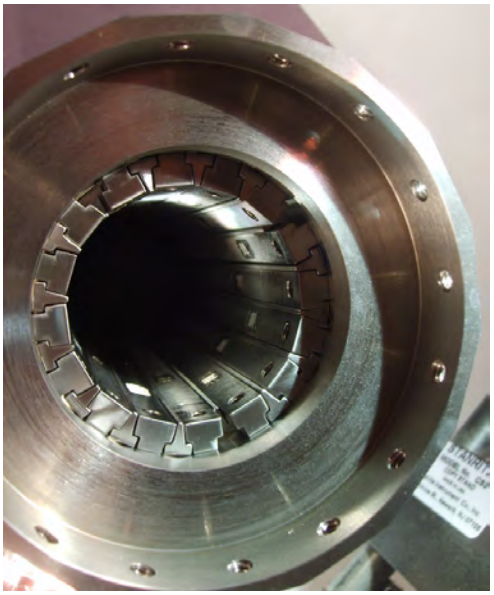

(b) Front view of the collimator

Figure 3.10: (a) Photo of the assembled collimator. The plates are bolted together using tungsten screws and the pinholes are inserted and glued on them. At the right end of the collimator, the screw holes to bolt the mid-magnification part of the collimator are visible. (b) Front view of the collimator showing the barrel-like arrangement of the plates to prevent leakage.

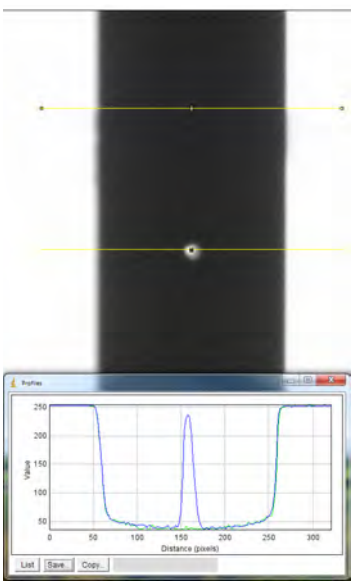

(a) Results of x-ray leakage test

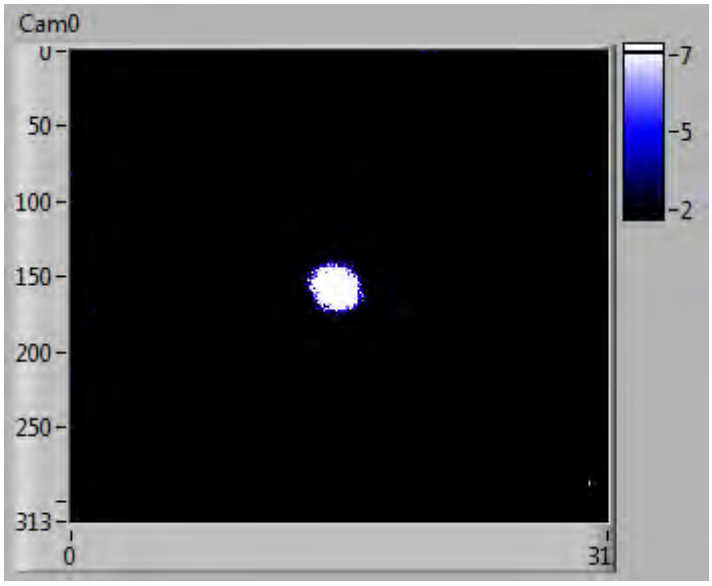

(b) Results of leakage test using a $^{99m}Tcsource$

Figure 3.11: (a) Results of the leakage test performed using an x-ray source. Leakage is measured by joining three adjacent plates and placing a pinhole in the central plate. A planar x-ray projection is taken and the intensity along a line passing through the pinhole is compared to a line through all the material. No leakage was observed at the place where the plates are joined nor at the place where the pinhole is inserted. (b) Result of the test performed using a ^{99m}Tc point source showing no leakage.

3.3.2 Shutters

To manufacture the shutters, we selected a polymer used in plastic bearings called Igus® J. [83] This material is easy to machine, strong, and has a very low coefficient of friction when used in contact with anodized aluminum. We therefore manufactured the fixed part of the shutter in aluminum and the rotating part using the Igus® J material. This combination allows the rotating ring of the shutter to act as its own bearing. The tungsten blocks were again manufactured by 3D Systems Layerwise using 3D-printing. This enables us to use a complex design for the blocks, with large radii on the edges and a step in the height, so that the manufacturing of the shutter ring can be easily accomplished on the CNC. Figure 3.12 shows pictures of the mid-magnification shutters in both the opened and closed states.

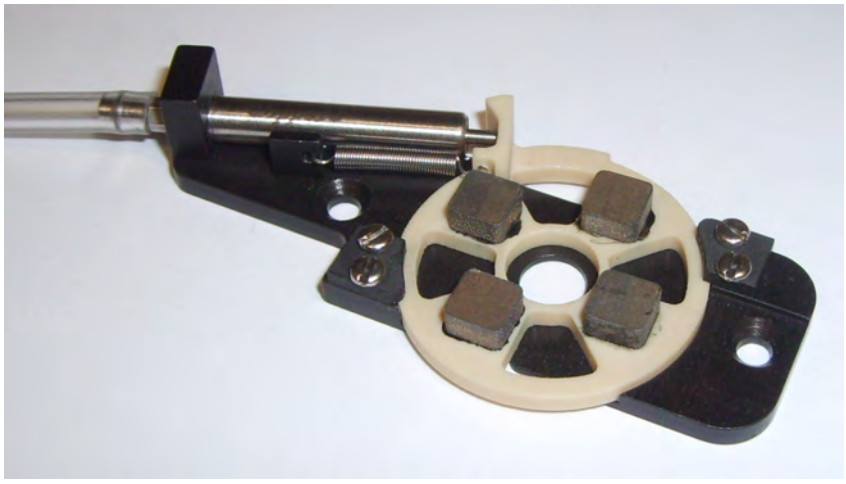

(a) Single-pinhole configuration

(b) Five-pinhole configuration

Figure 3.12: Shutters manufactured for the mid-magnification ring segment. The base (black) is in aluminum and has been hard anodized. The circular plate (yellow) is manufactured using the Igus® J material. The four tungsten blocks are manufactured using additive manufacturing and glued on the circular plate. In (a) the piston is not actuated and the four peripheral pinholes are covered by tungsten blocks yielding single-pinhole projections. In (b) the actuated piston rotates the circular plate and opens the peripheral pinholes yielding a five pinhole-per-camera configuration. The spring is extended and will bring the circular plate back in place once the piston retracts.

3.3.3 Complete Aperture

The final parts for the aperture were delivered in July 2015 and successfully assembled. The completed aperture, along with its shutters is shown in Figure 3.13

Figure 3.13: Assembled Aperture.

3.4 Conclusions

In this chapter, we presented the design of the adaptive aperture, its imaging properties, and its mechanical components. We made use of additive manufacturing, both for the pinhole inserts of the aperture as well as its shutters. We designed the body of the aperture to be machined in a tungsten alloy and assembled like a barrel. This design proved successful, as it allowed for manufacturing an aperture that is really three apertures stacked together that can support its own weight during linear motion. The next chapter will discuss the integration of the system and the controllers that drive the aperture motion.

The manufacturing techniques discussed in this chapter (cold casting and additive manufacturing) enable new shapes to be developed, as well as an easy transition from computer-assisted design to finished product. It is our belief that these techniques will be widely used in the future since they can produce apertures with designs that were impossible only a few years ago. We are also convinced that apertures that can be axially translated to allow for multiple magnifications or pinhole shapes will become more common. In fact, this type of design has also been used by Moore *et al.* [127] to produce a collimator capable of two magnifications for mouse imaging, as well as by Pato *et al.* [133] to produce a collimator that allows complete angular sampling with tilted holes whose angular view change when the collimator is translated.

CHAPTER 4

System Integration and Controllers

This chapter describes the mechanical integration of AdaptiSPECT as well as the controllers and software developed for autonomous adaptation. It describes the adaptive capabilities of the AdaptiSPECT hardware.

4.1 Detector Mounts and Controllers

The 16 independent gamma-ray detectors in AdaptiSPECT are completely controlled by a custom software package. This includes both the radial, or adaptive, motion of the detector and the non-adaptive features such as the high-voltage (HV) and acquisition electronics. A schematic of the detector controllers including the software layers is shown in Figure 4.1.

Each detector is mounted on a linear stage that is in turn mounted on a backplate to form a modular unit that is bolted to the system gantry. The programmable HV unit and the acquisition electronics are also mounted on the module but do not move with the detector. A photograph of the detector module and its various components is shown in Figure 4.2

4.1.1 Motion Controllers

The linear stages used for each detector are manufactured by Velmex. They have 6 in of travel (152.4 mm), and the smallest achievable step is 0.000125 in (3.1 μm). The pitch of the lead screw of the stage is in imperial units, and therefore precise placement will be achieved when translation commands are also issued in imperial units (inches). Each stage is driven by a Velmex VXM controller capable of driving two stages. However, since only one stage on the controller can be moved at a time, moving all 16 detectors requires two separate procedures.

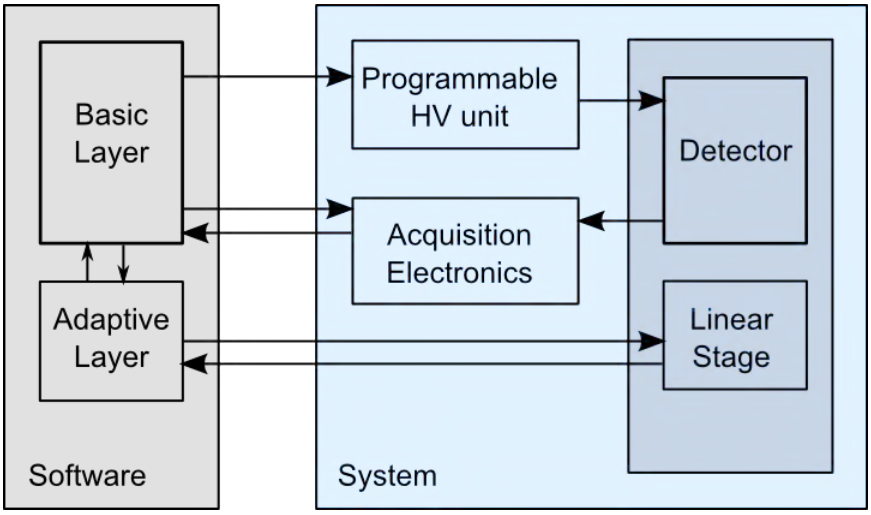

Figure 4.1: Schematics of the communication system for the detector controllers.

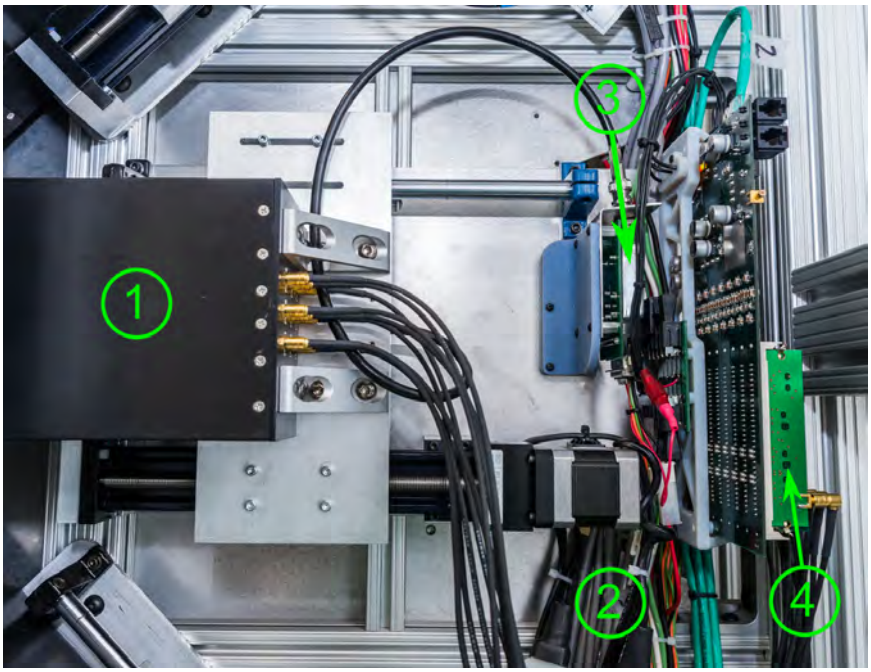

Figure 4.2: Picture of a detector module mounted in AdaptiSPECT. The detector (1) is mounted on a plate fixed to the translation stage (2). Behind the detector sit the high-voltage unit (3) and the acquisition electronics (4). Photo by Joseph Ortiz.

4.1.2 High Voltage

Each camera has its own programmable high-voltage unit connected to the computer through a 16-channel National Instruments DAQ board. The high-voltage unit is manufactured by EMCO and converts a digital to analog volatge input ($\leq 5\ V$) to the roughly 800 V supply required by the AdaptiSPECT cameras. In order to function properly, the high-voltage unit requires an additional 5V reference signal. A picture of a high-voltage unit with the proper wiring is shown in Figure 4.3.

Figure 4.3: Picture of a programmable high-voltage unit used on AdaptiSPECT. The wiring on this unit is (from bottom to top): 5V ground, DAQ ground, DAQ command, 5V reference, input V.

4.2 Aperture Controllers

The adaptive layer of the software is the only layer that communicates with the aperture. The components to control are (1) the linear stage that positions the appropriate ring of pinholes in front of the detectors for imaging, (2) a linear sensor used to precisely position the aperture, and (3) the shutters that can open or close individually to switch between a one-pinhole-per-camera configuration to a five-pinholes-per-camera configuration. These shutters are operated by pneumatic pistons that can be activated when the shutter controller signals a solenoid valve in the air supply line to switch between open and closed states. A schematic of the aperture controller configuration is shown in Figure 4.4.

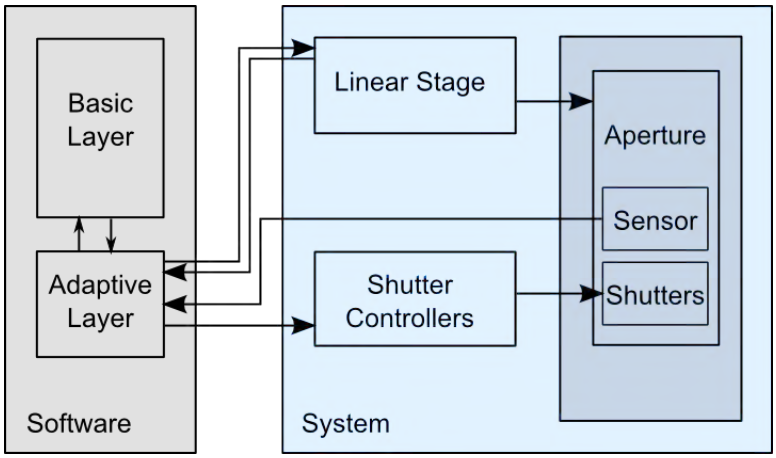

Figure 4.4: Schematic of the communication system for the aperture controllers.

4.2.1 Aperture integration

The first step in mounting the aperture was to align the stage that drives the motion. To do this, we started by 3D-printing a set of pinholes that attach to the detectors in the front and back, creating an axis to which we can align the aperture. We then sent a collimated He-Ne laser through the pinholes to provide an optical reference for the axis. The stage was then aligned using an autocollimation method with a mirror that we permanently attached inside the aperture holder. The holder was mounted on the translation stage and moved back and forth along the entire length of the aperture stage to verify the alignment. Once the procedure was completed, the aperture was bolted to the holder and aligned to the supporting rails, again using autocollimation. Stress from any residual misalignment is relieved by a spring-tensioned connector.

The next step in positioning the aperture was to find the three positions at which the pinholes are in front of the detectors. To do this, we designed and 3D-printed a mount that places a radioactive point source at the center of the mid-magnification segment of the aperture. The detectors are then moved to their middle positions where the center of the field of view is designed to be projected to the center of the detector. We then corrected the aperture position by moving it until the projection of the point source was actually at the center of each detector. The LEDs and positioning sensor described in Section 4.2.2 are then set to this position.

We repeated the process for the high- and low-magnification sections of the aperture.

In practice, there is a parallax error possible with this technique. *I.e.* if the point source is not exactly at the center of the field of view, the aperture will either be placed too far forward or too far towards the back of the system, as illustrated in Figure 4.5. This error is visible when moving the detectors away from the aperture. In this case, the point that was initially at the center of the field of view should be displaced by the same amount on the detectors in the front of the system as on the detectors in the back. If that is not the case, then the aperture is misplaced by an amount δ_x, as shown in Figure 4.5. The value of the misplacement can be calculated from the positions on the detectors in the front $x_1^{'}$ and on the back $x_1^{''}$, along with the pinhole height h, and the detector distances D_1 and D_2:

$$\delta_x = \left(x_1^{'} - x_1^{''}\right) \frac{1}{2} \frac{D_1 - h}{D_2 - D_1} \tag{4.1}$$

If $x_1^{'} > x_1^{''}$, then the aperture is too far back.

4.2.2 Aperture positioning

The linear stage that controls the aperture motion is a Velmex E01, with a smallest achievable step of 0.00025 in (6.3 μm). This stage has a backlash correction programmed in its controller that will adjust for 20 steps (0.005 in or 127 μm) when the stage is driven towards the motor. We designed a sensor based on a Hamamatsu position-sensitive optical detector that mounts on the aperture holder to increase the precision of the positioning. The sensor circuit board is shown in Figure 4.6 with the 12 mm x 1 mm detector shown in a yellow box. The detector has two photodiodes connected to a common cathode (see schematic in Figure 4.7) and outputs two currents, I_1 and I_2. When a light-emitting (LED) source is aligned with the center of the detector, the two currents are equal. Thus, alignment is accomplished by finding where $I_2 - I_1 = 0$.

To position the aperture properly, we mount LEDs on the side of the aperture motion stage that are at a fixed position relative to the pinhole rings. To provide a uniform illumination pattern, we positioned 910 nm LEDs behind 1.6 mm diameter

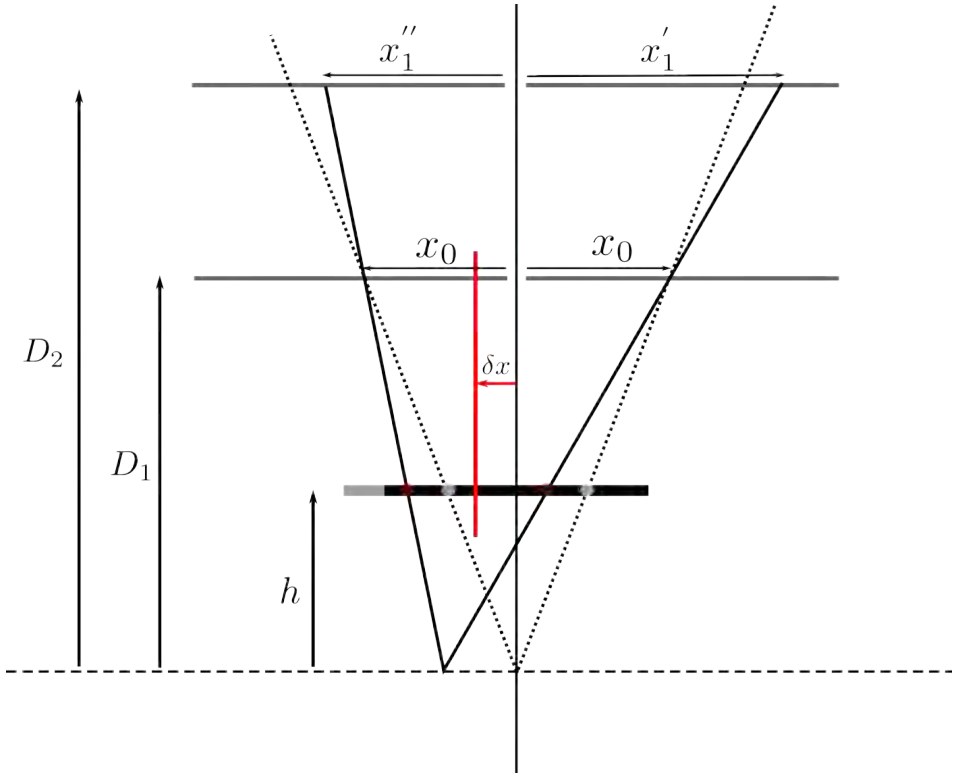

Figure 4.5: Aperture misplacement: if the aperture is moved too far back from the center of the system by a distance δ_x, then the symmetry of the system is lost. It is still possible to find a point that will project to the center of the detector when the detectors are in the middle position (at distance D_1), but when moving the detectors farther away (at distance D_2), the projection will be displaced more on one detector than the other. When the aperture is well centered (pinholes in gray), we have $x_1^{'} = x_1^{''}$, and if not (pinholes in red), then $x_1^{'} \neq x_1^{''}$.

pinholes at multiple locations. This ensures that all possible positions for the aperture have the same spot size and provide the same sensor response. The custom printed circuit board with the position sensor is mounted on the aperture holder and moves with the aperture during the translation. Since there are only 3 primary positions for the aperture corresponding to the three pinhole rings, we need to place LEDs at only 3 locations. For each, we used two LEDs: one is used to indicate the position of the aperture and the other one is placed a few millimeters ahead of the first to signal to the control computer that the aperture is approaching the

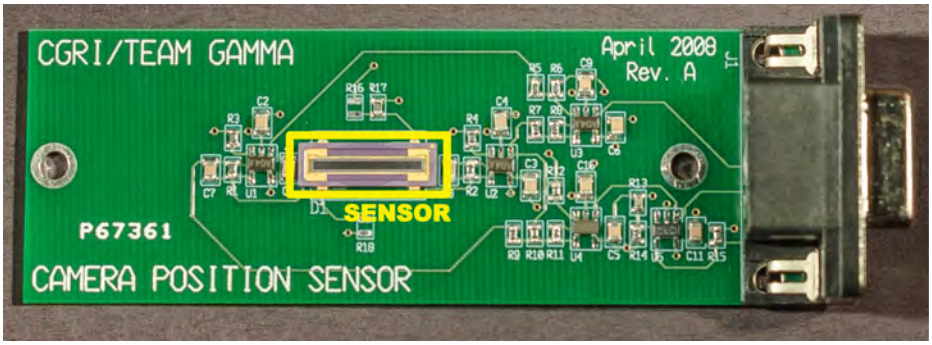

Figure 4.6: Custom printed circuit board for controlling the aperture positioning. The sensor is a position-sensitive detector, manufactured by Hamamatsu (S3932).

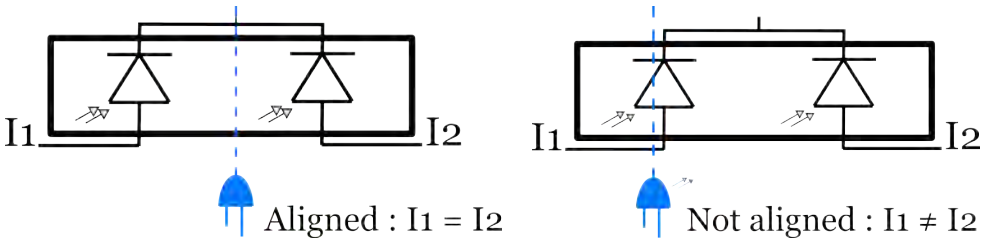

(a) LED and sensor are aligned (b) LED and sensor are not aligned

Figure 4.7: Functional schematic of the Hamamatsu position sensitive detector S3932. The sensor is made of two photodiodes connected to a common cathode. When the light source (in this case an LED) is positioned above the center of the sensor as shown in (a), the two currents coming from the photodiodes are equal. (b) When the light source is not positioned above the center of the sensor, the two currents are different. Alignment of the positioning LED and the detector is accomplished by simply measuring the difference between I_1 and I_2.

correct position, and that a deceleration should start. This positioning scheme is summarized in Figure 4.8.

The circuit board outputs three signals that are read by a National Instruments DAQ device. The three channels are:

- **Channel 0, detection**: This channel is a simple comparator and outputs 5V when $I1$ or $I2$ are non-zero. When the output of this channel is 5V, the detector is in front of an LED.

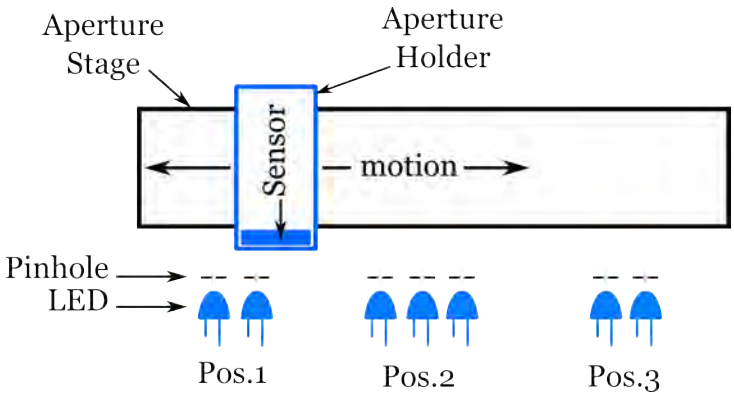

Figure 4.8: Diagram of sensor position scheme. For each of the three aperture configurations there is a group of LEDs and their corresponding optical elements placed in fixed positions along the stage. The printed circuit board with its sensor is mounted on the aperture holder and moves with the aperture, translating in front of the positioning LEDs.

- **Channel 1, sum**: This channel outputs $I1 + I2$. It is non-zero when the detection channel voltage is high and has a minimum at $I1 = I2$ when the middle of the sensor is in front of an LED.

- **Channel 2, difference**: This channel outputs $I1 - I2$ and reaches 0 when the middle of the sensor is in front of the LED.

Figure 4.9 shows the output of each channel along the entire aperture travel.

The LED holders and their pinholes were 3D printed in an opaque plastic and each LED module is mounted on a Thorlabs manual stage so that the position of the LEDs can be adjusted when the aperture is first aligned. Once the aperture is aligned, the stage set screw is tightened to fix the position. A photo of the LED modules positioned along the stage of the aperture is shown in Figure 4.10.

Adding this position sensor to the linear stage improves the reproducibility of the positioning of the aperture. This is crucial for the correct operation of the system because the aperture-positioning configuration with which a dataset is acquired needs to be known relative to the configurations used to calibrate the system. Furthermore, the stage controller only gives a relative position and the independent LEDs provide the ability for the system to home to a known location after a power outage, without user intervention.

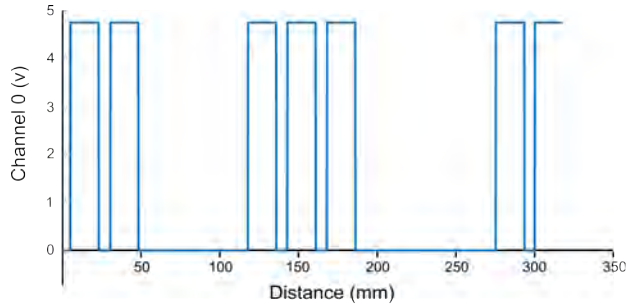

(a)

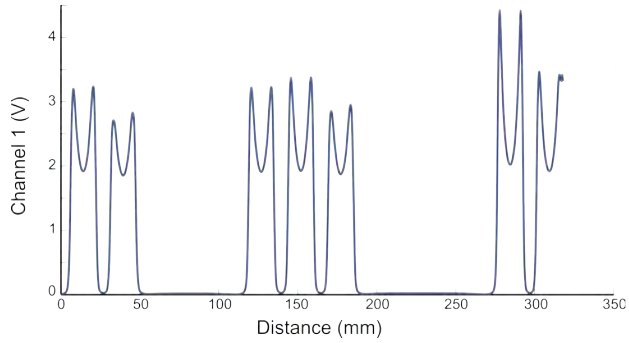

(b)

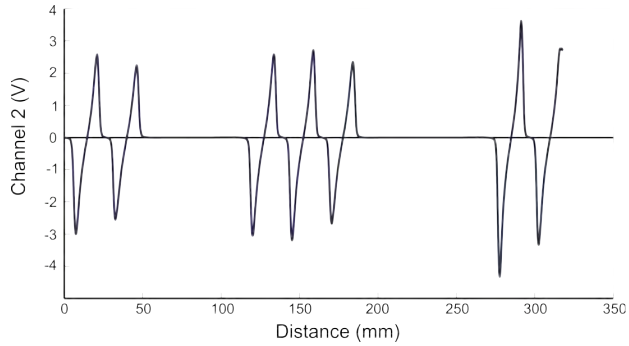

(c)

Figure 4.9: Output of the three channels from the positioning circuit board. (a) Channel 0 indicates when the sensor is in front of an LED, (b) channel 1 and (c) channel 2 can be used to position the sensor exactly in front of an LED.

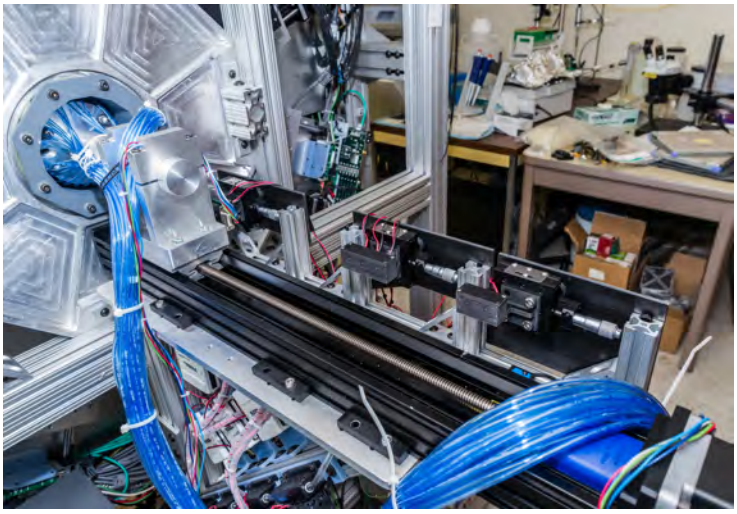

(a) View of the three LED modules.

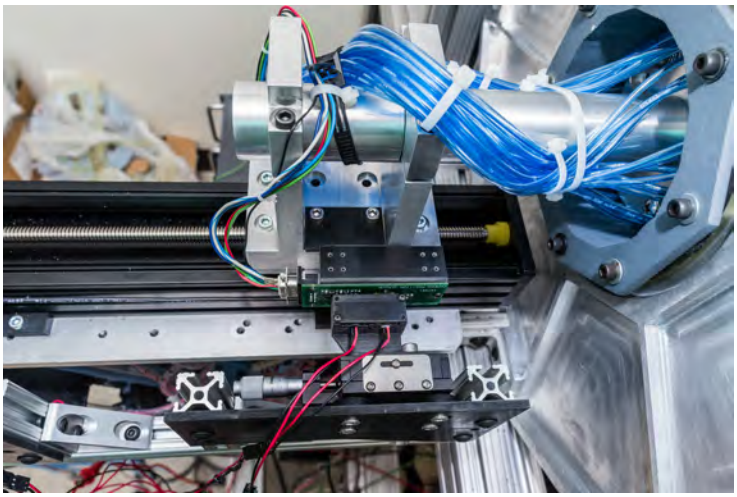

(b) Close view of the positioning sensor in front of the high-magnification LED module.

Figure 4.10: This figure shows the LED modules used for precise positioning of the pinhole aperture. The three modules are each mounted on a Thorlabs translation stage to adjust their position during the aperture alignment. The sensor is mounted on the aperture holder and translates along the stage during the aperture motion. Photos by Joseph Ortiz.

Positioning algorithm

The positioning algorithm we chose to implement is quite straightforward and uses only channel 0 and channel 2. Because the stage controller implements a backlash correction when moving the aperture backward, it is more efficient to use a positioning algorithm that only moves the aperture forward. For this reason we do not use channel 1 which would require implementing a minimum search algorithm that would move the aperture back and forth multiple times. Instead we use channel 2 and move the aperture in only the forward direction. The positioning algorithm follows the following steps:

1. A command is sent to move the aperture to a new position.
2. The distance to travel is computed from a look-up table. The aperture is moved.
3. Fine positioning begins. If conditions are met (channel 0 outputs 5V to show that the aperture is in front of a LED, and channel 2 value is less than 6 times the variance measured with LEDs off), no further motion is done.
4. If condition is not met, aperture is moved 30 steps backwards, and then moved forward 2 steps at a time until a change of sign in channel 2 is detected. Motion is stopped.

Precision of positioning

To test the positioning reproducibility, we performed the following measurements:

(1) We positioned a dial indicator that contacted the aperture when it was in the high-magnification configuration. We then move the aperture to the mid-magnification position and then back to the high-magnification position, where we noted the new value of the dial indicator. We repeated this measurement 10 times. A photo of the set-up for this measurement is shown in Figure 4.11. The dial indicator used has increments of 0.001 in (25 μm) and for all 10 measurements the displacement was smaller than one increment of the indicator. We therefore

conclude that we can reproducibly position the aperture with a precision less than 0.001 in (25 μm).

(2) We placed a point source approximately at the center of the field of view when the aperture was in the high-magnification position. The point source is identical to the sources we use to calibrate the system and will be described in more detail in Chapter 5. We acquired the projection of this point source on all 12 available detectors in this configuration. The aperture was then moved to the mid-magnification position and the acquisition was repeated before returning to the high-magnification position. This process was repeated 10 times to acquire a total of 10 point source projections at each of these two aperture configurations. We then processed the data as if they were calibration data by fitting a 2D-Gaussian to each projection. The values that are the most interesting for this experiment are the position of the 2D-Gaussian and the variance of the 2-D Gaussian. In Table 4.1 we show the results of the 2D-Gaussian fits averaged over the 10 measurements for each camera file in the high-magnification (HM) and mid-magnification (MM) positions. The position of the 2D-Gaussian is given by x_{detector} and y_{detector} and the FWHM of the 2D-Gaussian is given by σ_x and σ_y. It is clear that for each camera file, the standard deviation on the position of the 2D-Gaussian is much smaller than the width of the 2D-Gaussian. In fact, in the worst case (HM Cam06), we still have $\text{deviation}\,(x_{detector}) < 1/10 * \sigma_x$. In all other cases, we have $\text{deviation}\,(x_{detector}) < 1/100 * \sigma_x$ and $\text{deviation}\,(y_{detector}) < 1/100 * \sigma_y$.

From these two measurements, we conclude that the repeatability in positioning the aperture and moving it from one configuration to another is precise enough that the system does not need to be re-calibrated after each change of configuration.

4.2.3 Shutters integration and controllers

The shutters are opened and closed using miniature compressed air pistons that are controlled by electronic valves. We have designed a custom printed circuit board to control the actuation of the shutters. For each electronic valve, we use a FET switch triggered by a signal generated by a National Instruments DAQ USB

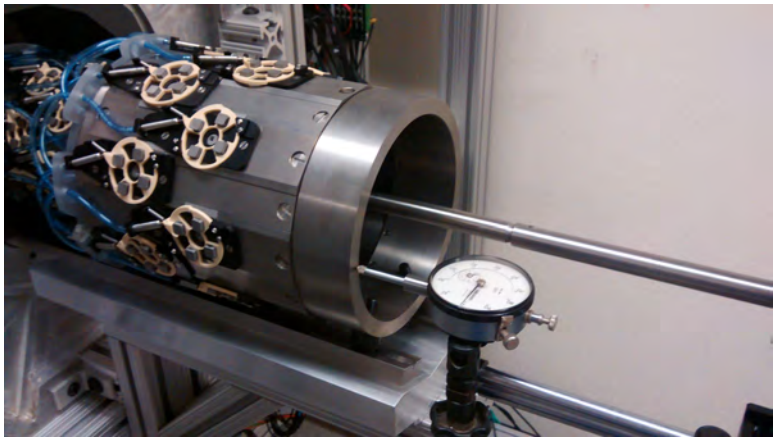

Figure 4.11: Setup to control the aperture positioning. A pressure probe is placed in contact with the front of the aperture in the high-magnification configuration. When the aperture is moved, any misalignments would result in a change in the measured pressure.

6009. Each custom electronic board monitors the opening and closing of 8 shutters independently of each other. In addition to the transistor switch, each circuit has logic that shows the open/closed status of each shutter. All four controllers for the shutters are mounted on the AdaptiSPECT gantry directly below the aperture drive stage. This minimizes the amount of pneumatic tubing necessary to connect the compressed air source with each shutter. This also places all of the controllers and air tubing away from the entrance of the imaging system where the operator will be handling animals and related equipment (anesthesia, heart rate monitor, etc.). Figure 4.12 shows a single shutter and the associated control components (a) unmounted and (b) mounted in final position on the gantry.

	$x_{detector}$ (mm)	σ_x (mm)	$y_{detector}$ (mm)	σ_y (mm)
HM Cam00	60.103 ± 0.016	2.753 ± 0.002	60.717 ± 0.108	2.654 ± 0.003
HM Cam01	58.562 ± 0.039	2.874 ± 0.003	63.437 ± 0.097	2.786 ± 0.003
HM Cam02	60.079 ± 0.117	4.022 ± 0.007	62.892 ± 0.057	3.168 ± 0.006
HM Cam03	59.833 ± 0.045	3.099 ± 0.001	60.757 ± 0.033	2.572 ± 0.002
HM Cam04	59.638 ± 0.024	2.511 ± 0.002	59.532 ± 0.032	2.448 ± 0.003
HM Cam05	61.410 ± 0.066	2.837 ± 0.001	61.176 ± 0.034	2.770 ± 0.005
HM Cam06	60.948 ± 0.341	4.244 ± 0.005	61.087 ± 0.101	3.610 ± 0.003
HM Cam07	59.338 ± 0.133	3.321 ± 0.002	60.360 ± 0.072	2.814 ± 0.002
HM Cam08	58.128 ± 0.002	2.771 ± 0.002	60.138 ± 0.051	2.674 ± 0.003
HM Cam09	58.785 ± 0.067	3.214 ± 0.001	57.398 ± 0.091	2.982 ± 0.005
HM Cam10	57.041 ± 0.058	2.578 ± 0.002	58.310 ± 0.068	2.399 ± 0.002
HM Cam11	60.578 ± 0.212	3.442 ± 0.004	57.669 ± 0.047	2.805 ± 0.002
MM Cam00	56.666 ± 0.009	2.176 ± 0.001	61.607 ± 0.010	2.210 ± 0.001
MM Cam01	55.635 ± 0.015	2.395 ± 0.001	64.829 ± 0.006	2.416 ± 0.001
MM Cam02	59.074 ± 0.018	3.265 ± 0.002	64.236 ± 0.008	2.724 ± 0.002
MM Cam03	61.816 ± 0.021	2.243 ± 0.003	60.639 ± 0.007	2.227 ± 0.002
MM Cam04	62.899 ± 0.014	1.921 ± 0.001	60.350 ± 0.006	2.040 ± 0.001
MM Cam05	63.460 ± 0.026	2.203 ± 0.002	63.610 ± 0.003	2.085 ± 0.002
MM Cam06	60.194 ± 0.040	3.394 ± 0.004	63.771 ± 0.006	2.919 ± 0.007
MM Cam07	56.458 ± 0.027	2.397 ± 0.002	63.318 ± 0.005	2.356 ± 0.002
MM Cam08	61.042 ± 0.007	2.239 ± 0.002	58.847 ± 0.008	2.260 ± 0.002
MM Cam09	58.380 ± 0.009	2.403 ± 0.002	56.825 ± 0.008	2.517 ± 0.004
MM Cam10	54.434 ± 0.028	2.112 ± 0.003	58.547 ± 0.008	2.044 ± 0.001
MM Cam11	63.099 ± 0.025	2.439 ± 0.001	58.453 ± 0.004	2.417 ± 0.002

Table 4.1: Position and variance of the 2D-Gaussian fitted to the projection of a point source through the aperture. The positions and variances reported are averaged over 10 measurements.

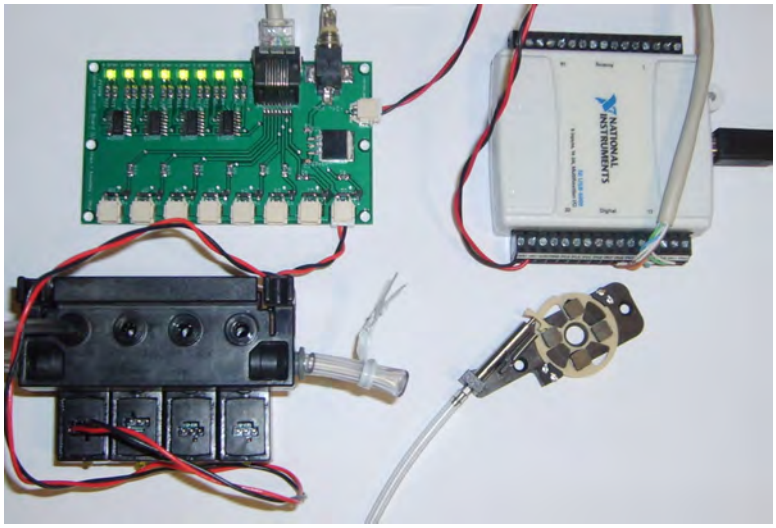

(a) Mid-Magnification shutter and its controllers

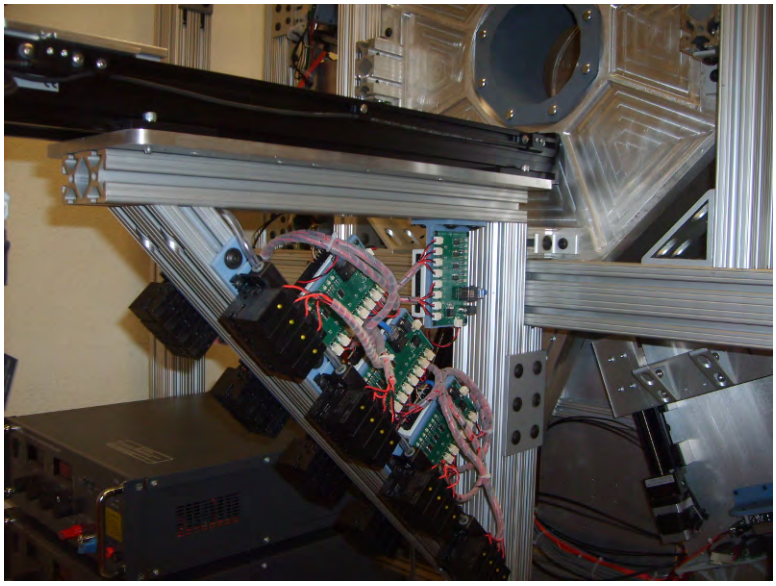

(b) Shutter controllers integrated with the AdaptiSPECT gantry

Figure 4.12: (a) Mid-magnification shutter and control elements including the custom electronics, pneumatic valves, and National Instruments DAQ system. (b) All four shutter controllers and 32 valves mounted on the gantry. The boards and valves are placed directly under the stage driving the selection of the adaptive aperture configuration.

4.3 Conclusion

In this chapter we have presented the various controllers that drive the adaptive functionality of AdaptiSPECT. In particular, the controllers positioning the aperture were described and measurements performed to quantify their repeatability. We found that the precision and repeatability is adequate for imaging without having to re-calibrate the system after each change of configuration. A photo of the completed system is visible in Figure 4.13.

Figure 4.13: Complete AdaptiSPECT system. Photo courtesy Joseph Ortiz.

CHAPTER 5

System Calibration

The final step in building a system like AdaptiSPECT is to have a calibration method for the detectors and imaging apertures introduced in previous chapters. This chapter reviews the calibration method used at the Center for Gamma-Ray Imaging on systems such as FastSPECT II and FastSPECT III, and proposes a way to expand this method for the unique challenges of AdaptiSPECT.

5.1 Introduction

The purpose of a calibration is to model the continuous-to-discrete operator $\mathcal{H}$ that maps the object in continuous space $f(r)$ to the discrete projection $\mathbf{g}$:

$$\mathbf{g} = \mathcal{H}f(r) + \mathbf{n}, \tag{5.1}$$

where n is the system noise [21]. A discrete-to-discrete representation of equation 5.1 that describes a SPECT imaging system mapping a voxelized object $\mathbf{f}$ to a binned projection $\mathbf{g}$ can be modeled by a system matrix $\mathbf{H}$ such that

$$\mathbf{g} = \mathbf{H}\mathbf{f} + \mathbf{n} \tag{5.2}$$

where $\mathbf{n}$ is a random noise vector. If the object space is modeled by N volume elements (voxels), and the projection space is modeled by M bins, then $\mathbf{f}$ is an $N \times 1$ vector, $\mathbf{g}$ is an $M \times 1$ vector, and $\mathbf{H}$ is an $M \times N$ matrix. Each element of the matrix $\mathbf{H}$, h_{ij} represents the probability that a photon emitted in voxel j is detected in bin i.

Knowledge of this system matrix is essential for iterative reconstruction algorithms, such as the Maximum-Likelihood Expectation-Maximization method (MLEM) [144], that are widely used in small-animal SPECT. These reconstruction

algorithms have the advantages of incorporating an accurate model of the imaging system, not requiring a mathematical expression for the inverse transformation, and enforcing positivity. Knowledge of the system matrix is also necessary to carry out estimation and detection tasks. For example, the Wiener estimator [74, 169], the Hotelling observer, and the scanning-linear estimator [168] all require knowledge of the system matrix **H**. The more accurate the chosen model, the more accurate the image reconstruction, estimated properties of the object, and lesion detectability will be [25, 59, 61, 153]. Furthermore, in adaptive SPECT imaging systems, accurate models of system matrices for multiple possible configurations are needed to implement decision algorithms that adapt the imager's configuration in response to the data it has acquired [17, 35, 44].

The system matrix should contain accurate information about the system geometry, pinhole penetration, aperture fabrication defects, detector blur, and detector misalignments. A variety of methods to compute the system matrix have been demonstrated including Monte-Carlo simulations [90], analytical models [5, 28, 109, 113, 150], geometrical calibration of rotating systems [28, 50, 93, 111–113, 136], direct measurement [43, 66, 72, 89, 118], or a combination of all these techniques [158].

Direct measurement techniques are well suited for stationary SPECT systems and have been used previously at CGRI on FastSPECT I, II, and III [66, 118]. Direct measurement of the system matrix consists of scanning the system's field of view with a small point source and measuring each point response function [43, 66, 158]. Since a direct measure of the system matrix takes into account all the physics of the system and can be used with only smoothing and normalization for reconstructions, it is the most straightforward way of calibrating a system. However, this calibration technique comes with the drawback that it requires preparation of a point source and long acquisition times during which the system cannot be used for other imaging purposes. For example, on FastSPECT II, exhaustive calibration requires scanning a small point source of ^{99m}Tc in a cylindrical field-of-view with a 42 mm diameter and 54 mm length. For a grid with 1 mm spacing, this scan

requires the acquisition of more than 50,000 points, each requiring motion of at least one translation stage. With compensation for the radioactive decay of ^{99m}Tc, the calibration procedure takes around 24 hours to acquire 3,000 events per point. The reconstruction resolution was originally limited by how finely the grid was scanned during the calibration measurement. It is however possible to reduce the acquisition time and increase the resolution by scanning a grid with larger spacing and interpolating the system matrix between calibration points [43, 118].

In AdaptiSPECT, the problem of calibration time is even more challenging. The 16 detectors of AdaptiSPECT are mounted on translational stages and can move radially towards or away from the center of the field of view, and the aperture has multiple positions. The detectors can move continuously and independently along their radial axes, therefore the number of system configurations is essentially infinite. Unfortunately it is impractical to measure more than about 15 different configurations, as even the sparse calibration measurements still require an entire day to run. To account for the flexibility of these adaptive systems, we proposed a method to interpolate the system matrix for any detector position, given a few measured system matrices.

5.2 System Matrix Measurement

5.2.1 System matrix model

Starting with equation 5.2, the system matrix $\mathbf{H}$ can be decomposed into its scattered (sc) and unscattered components (un):

$$\mathbf{H} = \mathbf{H}^{(un)} + \mathbf{H}^{(sc)}. \tag{5.3}$$

The unscattered part of the system matrix, $\mathbf{H}^{(un)}$, can be further decomposed as:

$$\mathbf{H}^{(un)} = \mathbf{H}^{(det)} \left[\mathbf{H}^{(geom)} \odot \mathbf{A}\right], \tag{5.4}$$

where $\mathbf{H}^{(det)}$ describes the contribution of the detector, $\mathbf{H}^{(geom)}$ describes the contribution of the system geometry, and the matrix $\mathbf{A}$ is the object-dependent at-

tenuation along the propagation path. The operator $\odot$ is an element-by-element multiplication. Under the assumption that attenuation varies slowly compared to the spatial resolution of the detectors, the following approximation can be made [21]:

$$\mathbf{H}^{(un)} \approx \left[\mathbf{H}^{(det)}\mathbf{H}^{(geom)}\right] \odot \mathbf{A}. \tag{5.5}$$

The product $\mathbf{H}^{(det)}\mathbf{H}^{(geom)}$ describes the system completely and its elements are what are acquired experimentally by measuring the system response point-by-point in air. The acquisition process is described in the following section.

5.2.2 System matrix measurement

To experimentally acquire the system matrix, we manufacture a ^{99m}Tc point source using resin chromatography ion-exchange beads that have taken up the radioactive material. The beads have diameters varying between 250 and 850 μm and the total number of beads and their distribution inside a small epoxy drop determines the size of the final point source. The beads are attached to a carbon rod and the point source is then stepped inside the field of view on a 3D grid. For each point, the response of each detector is acquired in list mode with the resulting image at each location corresponding to one column of the system matrix. By scanning the entire field-of-view, the matrix is therefore populated column by column. In Figure 5.1, we show the point source inside the high-magnification segment of the AdaptiSPECT collimator, as well as the system response for 8 detectors when the point source is at the center of the field of view.

To smooth out noise from counting statistics, to allow for interpolation inside the field of view, and to increase the sampling of the object space, a 2D-Gaussian model is fitted to each detector's response. Interpolation in object space is then performed as described in [43] and [158]. On each detector j, the 2D-Gaussian response for voxel $\mathbf{n}$ can be described by:

$$h_{j\mathbf{n}}(\mathbf{r}) = \frac{A_{\mathbf{n}}}{2\pi\sqrt{\det \mathbf{K}_{\mathbf{n}}}} \exp\left\{-\frac{1}{2}[\mathbf{r}-\bar{\mathbf{r}}_{\mathbf{n}}]^T {\mathbf{K}_{\mathbf{n}}}^{-1}[\mathbf{r}-\bar{\mathbf{r}}_{\mathbf{n}}]\right\}, \tag{5.6}$$

where $\bar{\mathbf{r}}$ is the 2×1 mean vector of the 2D-Gaussian, A the scalar amplitude, and $\mathbf{K}$ the 2×2 covariance matrix that has three independent variables. Thus 6 parameters are estimated when fitting the point response on each detector. To increase the number of columns in the system matrix, these six coefficients are interpolated using trilinear interpolation.

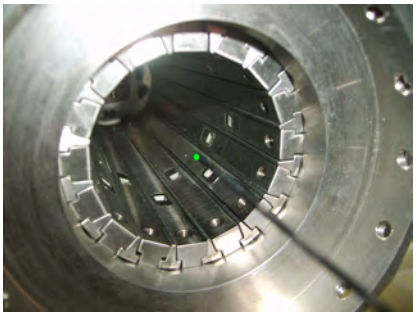

(a) Point source placed inside the AdaptiSPECT collimator.

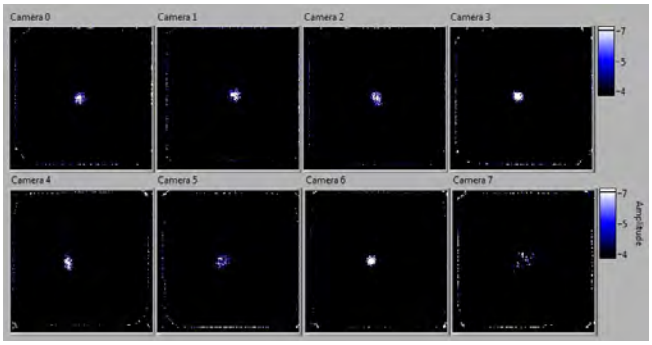

(b) Point response on 8 detectors of AdaptiSPECT when the source is placed at the center of the field of view.

Figure 5.1: Measurement of the system matrix. In (a), a point source materialized by a green dot is placed inside the collimator of AdaptiSPECT and then stepped on a 3D grid. In (b), the response of 8 detectors of AdaptiSPECT when the point source is placed in the center of the field-of-view is shown. This response corresponds to one column of the system matrix.

5.2.3 Normalization of the system matrix

As stated previously, each element of the system matrix, $h_{(i,j)}$ represents the probability that a photon emitted in voxel j is detected in bin i. To be able to quantify the activity in each voxel of a reconstructed image, it is necessary to normalize the response function such that the sum of each column of the system matrix, which represents the sensitivity of the system, can be expressed in counts per second per MBq (cps/MBq). To this end, we measure the activity of the point source used to calibrate the system at the beginning of the scan. The duration and time of acquisition at each point in the grid tells us how many photons have been emitted at this location. By dividing the amplitude of the fitted Gaussian by the number of

photons emitted, we can obtain the normalized system matrix, since each response is now expressed as the number of photons detected relative to the number of photons emitted at the calibration location.

5.3 Interpolation scheme for an adaptive SPECT system

For an adaptive SPECT imaging system where the detectors can be moved radially relative to the imaging aperture, we are interested in interpolating the system matrix for any detector position from a set of measured system matrices. The calibration technique we proposed, illustrated in Figure 5.2, consists of acquiring just two system matrices for each setting of the aperture: one with cameras at the nearest position (**N**) and one with cameras at the farthest position (**F**).

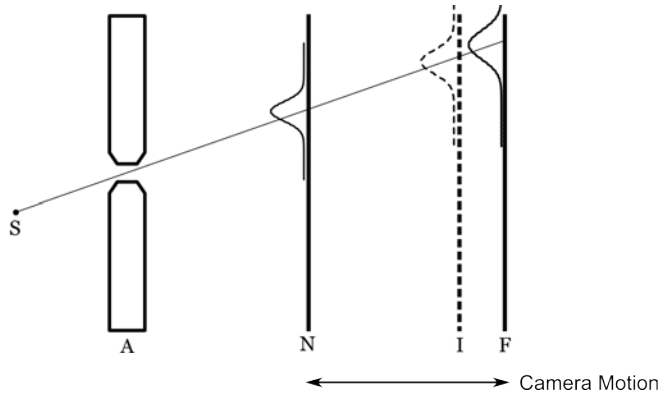

Figure 5.2: General calibration scheme: a point source (S) is positioned inside the field of view. Gamma-rays emitted from the source pass through the pinhole aperture (A) and hit the detector in its nearest position (N) and farthest position (F). The response for these positions is modeled by a 2D Gaussian. At any intermediate detector position (I), the response Gaussian can be derived from the N and F measurements.

For each measured point in the field-of-view for these two system matrices, a 2D-Gaussian is fitted to the point-response image acquired by each detector. The amplitude of the 2D-Gaussian is then normalized to take into account the activity of the point source. For any intermediate position of the detector **I**, we can interpolate the 6 Gaussian coefficients as described below.

Mean ($\bar{\mathbf{r}}$)

Gamma rays travel along straight lines established by the object location and pinhole location, and therefore we can find both components of $\bar{\mathbf{r}}$, $\bar{x}$ and $\bar{y}$, for the new camera position ($\mathbf{I}$) in the following way:

$$\bar{x}_{\mathbf{I}} = (\bar{x}_{\mathbf{F}} - \bar{x}_{\mathbf{N}}) \times \left(\frac{d_{\mathbf{I}} - d_{\mathbf{N}}}{d_{\mathbf{F}} - d_{\mathbf{N}}} \right) + \bar{x}_{\mathbf{N}} \tag{5.7}$$

$$\bar{y}_{\mathbf{I}} = (\bar{y}_{\mathbf{F}} - \bar{y}_{\mathbf{N}}) \times \left(\frac{d_{\mathbf{I}} - d_{\mathbf{N}}}{d_{\mathbf{F}} - d_{\mathbf{N}}} \right) + \bar{y}_{\mathbf{N}}, \tag{5.8}$$

where $d_{\mathbf{N}}$, $d_{\mathbf{F}}$, and $d_{\mathbf{I}}$ are the distances of the detector to the central axis for the nearest position, farthest position, and interpolated position respectively.

Covariance matrix

The variance of the 2D-Gaussian response, describing the width of the response, is a function of the magnification, which varies linearly with the detector position. However, this parameter cannot be interpolated directly because the intrinsic resolution of the detector is position dependent. We discussed this position dependency in Chapter 2, and the effect is illustrated in Figure 2.11. It is possible that when acquiring the response at the nearest position for voxel $\mathbf{n}$, the projection is located at a position on the detector where the detector resolution is high and isotropic, and that when acquiring the same voxel at the farthest position, the projection is located at a position where the detector resolution is lower and anisotropic, but that the intermediate camera positions are not the average of these conditions. Therefore, if we directly interpolate the fitted Gaussian variance, we will introduce an error that originates from the detector variance. The same argument holds for the covariance term and therefore, we need to correct our interpolation to take into account the anisotropic detector response.

From equation 5.5 we know that the resulting 2D-Gaussian from projecting a point source through a pinhole, is a convolution of the blur occurring from the pinhole and the blur occurring from the intrinsic resolution of the detector. Both can also be modeled by 2D-Gaussians. Therefore, combining equations 5.5 and 5.6

we have the following for the covariance matrices:

$$\mathbf{K}^{(un)} = \mathbf{K}^{(det)} + \mathbf{K}^{(geom)}, \tag{5.9}$$

where $\mathbf{K}^{(un)}$ is the covariance matrix stored in the system matrix, $\mathbf{K}^{(det)}$ is the contribution of the detector, and $\mathbf{K}^{(geom)}$ is the contribution of the geometry of the system, effectively a shadow image of the pinhole, that varies with magnification. Furthermore, the covariance matrix whose elements are given by:

$$\mathbf{K}^{(un)} = \begin{bmatrix} \sigma_x^2 & \rho\sigma_x\sigma_y \\ \rho\sigma_x\sigma_y & \sigma_y^2 \end{bmatrix}, \tag{5.10}$$

can be diagonalized:

$$\mathbf{K}^{(un)} = \begin{bmatrix} \cos\phi & -\sin\phi \\ \sin\phi & \cos\phi \end{bmatrix} \begin{bmatrix} l_x^2 & 0 \\ 0 & l_y^2 \end{bmatrix} \begin{bmatrix} \cos\phi & \sin\phi \\ -\sin\phi & \cos\phi \end{bmatrix}, \tag{5.11}$$

where l_x and l_y, the eigenvalues of $\mathbf{K}^{(un)}$, are the length of the axis of the 2D-Gaussian, and ϕ is the angle between the major axis and the $x-$axis of the detector. The values l_x, l_y and ϕ can also be decomposed into their geometrical contribution and their detector contribution:

$${l_x}^2 = {l_x}^{2(geom)} + {l_x}^{2(det)} \tag{5.12}$$

$${l_y}^2 = {l_y}^{2(geom)} + {l_y}^{2(det)} \tag{5.13}$$

$$\phi = \phi^{(geom)} + \phi^{(det)} \tag{5.14}$$

The geometrical components of the eigenvalues, $l_x^{(geom)}$ and $l_x^{(geom)}$, scale with the magnification and can be interpolated linearly. Therfore, $l_x^{2(geom)}$ and $l_y^{2(geom)}$ can be interpolated as follow:

$${l_{x,\mathbf{I}}}^{2(geom)} = \left({l_{x,\mathbf{F}}}^{2(geom)} - {l_{x,\mathbf{N}}}^{2(geom)}\right) \times \left(\frac{{d_\mathbf{I}}^2 - {d_\mathbf{N}}^2}{{d_\mathbf{F}}^2 - {d_\mathbf{N}}^2}\right) + {l_{x,\mathbf{N}}}^{2(geom)} \tag{5.15}$$

$${l_{y,\mathbf{I}}}^{2(geom)} = \left({l_{y,\mathbf{F}}}^{2(geom)} - {l_{y,\mathbf{N}}}^{2(geom)}\right) \times \left(\frac{{d_\mathbf{I}}^2 - {d_\mathbf{N}}^2}{{d_\mathbf{F}}^2 - {d_\mathbf{N}}^2}\right) + {l_{y,\mathbf{N}}}^{2(geom)} \tag{5.16}$$

The angle $\phi^{(geom)}$ is a constant with respect to detector travel, as it is only a function of the angle of incidence, which remains constant when the detectors are moved.

Thus we can interpolate the three components of the covariance matrix.

Amplitude (A)

The amplitude is normalized so that each 2D-Gaussian reflects the sensitivity of the system, which is not dependent on the camera position. In fact, the sensitivity of the system, at least in the center of the field-of-view should be the same for each camera location for a given aperture. The amplitude changes when moving the cameras so that the ratio $A/\sqrt{\det\mathbf{K}}$ is constant. Since $\sqrt{\det\mathbf{K}}$ varies as a square of the detector distance, we can interpolate the amplitude:

$$A_{\mathbf{I}} = (A_{\mathbf{F}} - A_{\mathbf{N}}) \left(\frac{{d_{\mathbf{I}}}^2 - {d_{\mathbf{N}}}^2}{{d_{\mathbf{F}}}^2 - {d_{\mathbf{N}}}^2} \right) + A_{\mathbf{N}}. \tag{5.17}$$

5.4 Demonstration

To test our interpolation method, we measured three system matrices for the high-magnification section of the AdaptiSPECT aperture. The configurations measured were for the cameras in the nearest position (165.1mm from the central axis), the cameras in the farthest position (317.5mm), and the middle position (241.3 mm). We used the system matrices acquired in the nearest and farthest positions to interpolate a system matrix for the detectors located at the middle position and compare it to the measured matrix. We then compared the sensitivity volumes for both system matrices, as well as the reconstructions of a known phantom.

5.4.1 Point comparison: proof of concept

The field of view scanned for the cameras in the nearest position was a cylindrical volume of $21 \times 27 \times 27$ points spaced by 1 mm, and for the farthest position, a volume of $17 \times 23 \times 23$ points, also spaced by 1 mm. We padded the smallest system matrix with 0 values where coefficients had not been measured, so that the resulting interpolated system matrix has a volume of $21 \times 27 \times 27$ points spaced by 1 mm. For reference, the system matrix measured for the cameras in the middle position has a volume of $19 \times 25 \times 25$ points, again spaced by 1 mm. The point source was made by concentrating ^{99m}Tc inside chromatographic beads and drawing them into an epoxy

bead on the end of a carbon fiber rod, which was then moved inside the collimator using a 3-axis translational stage. Extra care was taken to position the center of the field of view at the same place for all three measurements. In Figure 5.3 we show the raw PSF data for the center of the field of view for the three measured camera positions. The effect of changing magnification is clearly visible, as well as the effect of the point source traveling across the camera surface when the camera is moved.

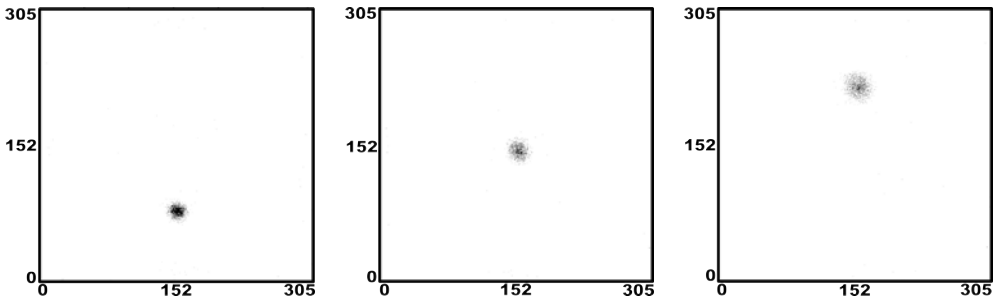

(a) Camera near (b) Camera mid (c) Camera far

Figure 5.3: PSF of the point at the center of the measured field of view for 3 camera positions (nearest position (a), middle position (b), and furthest position (c)). The entire camera surface with 305 by 305 bins is shown in this figure. The AdaptiSPECT pinholes are oblique, and the point at the center of the field-of-view travels across the camera face when the camera is moved.

We performed 2D-Gaussian fits on these measurements and, for the middle camera position, we compared the 2D-Gaussian parameters obtained from the measured data to the interpolated parameters. Only the location and covariance of the 2D-Gaussian were interpolated, the amplitude for the interpolated system matrix was set to be the same as the amplitude of the measured system matrix. In Figure 5.4, we show the results obtained for the point at the center of the field of view (point (0,0,0)) including the raw data, the 2D-Gaussian obtained by fitting the data, the interpolated 2D-Gaussian, and the interpolated 2D-Gaussian corrected for the detector covariance. Here, for the point (0,0,0), the fits match the measured data well because the interactions in all three cases (camera at the nearest, middle, and farthest positions) happen at the center of the detector, where the detector response is isotropic and fixed. In this case, correcting for the detector response is not critical.

In Figure 5.5, we show the same fits for another point in the field of view (point (3,-9,-3)). In this case, for all three detector positions, the interaction on the detector surface happens close to the edge of the detector where the intrinsic resolution is reduced and anisotropic. In this case, we find that correcting for the detector covariance is crucial.

5.4.2 Full field of view and reconstructions

We computed the sensitivity of the interpolated system matrix and compared it to the sensitivity of the measured system matrix. In Figure 5.6 we show the resulting sensitivity maps on the central axis of the imaging volume and it is clear that the field of view is smaller in the interpolated system matrix than in the measured system matrix. This occurs because the field of view is smallest when the detector is farthest from the aperture and thus there will be portions of the detector in closer positions that fall outside the field of view of the farthest position. Any interpolated system matrices will therefore be limited to the field of view determined by the farthest position. This is particularly evident when looking at the axial field of view, which is much smaller and of lower quality than the field of view from the measured system matrix. In fact, in the high magnification configuration, the axial field of view when the camera is at its farthest position is only 5 mm thick. This will be discussed further in Chapter 6.

The profiles of the sensitivity plots taken across the transaxial slice, shown in Figure 5.7, confirm the assessment that the sensitivity is not smooth. Therefore, it is likely that when trying to reconstruct a phantom using this interpolated matrix, only small fractions of the volume will be reconstructed properly, and that any reconstruction performed with this matrix will present more artifacts than reconstructions performed with the measured system matrix.

Another problem that we encountered when carrying out this interpolation scheme is that for some points in the field of view, the projection of the point source hits a yellowed spot on the camera and either creates a dark spot or a distorted projection. When using two system matrices to find a third one, the number

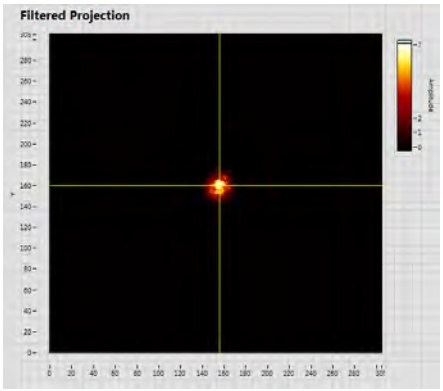

(a) Measured point response. The interaction occurs at the center of the detector surface.

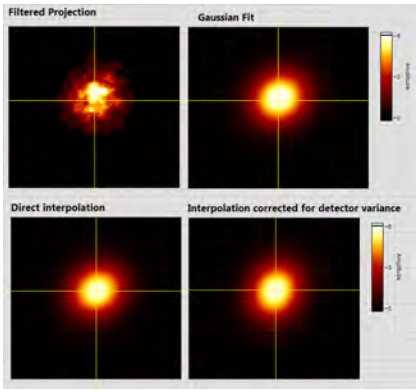

(b) Close-up view of the measured point response (upper left), fitted Gaussian (upper right), interpolated Gaussian without detector correction (lower left) and interpolated Gaussian with detector correction (lower right).

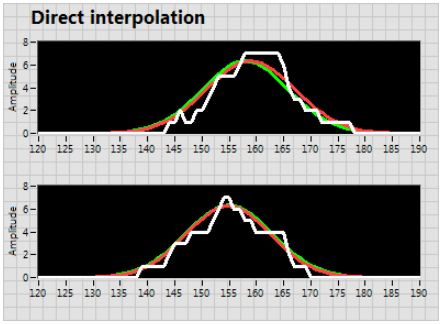

(c) Cross sections of the point response and the 2D-Gaussians (fitted and interpolated) without correcting for the detector.

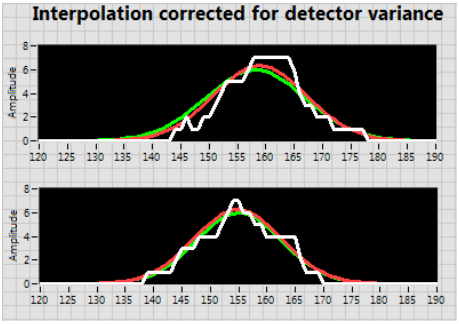

(d) Cross sections of the point response and the 2D-Gaussians (fitted and interpolated) with correction for the detector.

Figure 5.4: Results of the interpolation for the point at the center of the field-of-view (0,0,0): (a) measured response with camera placed in its middle position; (b) corresponding fitted 2D-Gaussian and interpolated Gaussians, with and without detector correction; (c) profiles of the measured response with the fitted Gaussian (in red) and the interpolated Gaussian without detector correction (in green); (d) profiles of the measured response with the fitted Gaussian (in red) and the interpolated Gaussian with detector correction (in green).

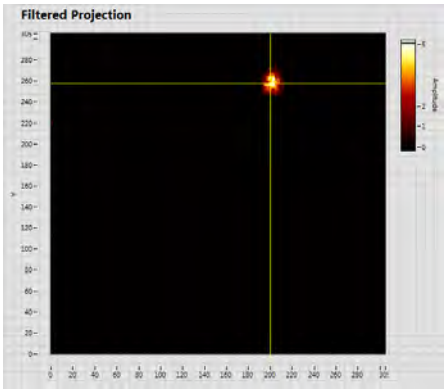

(a) Measured point response. The interaction occurs on the edge of the detector surface.

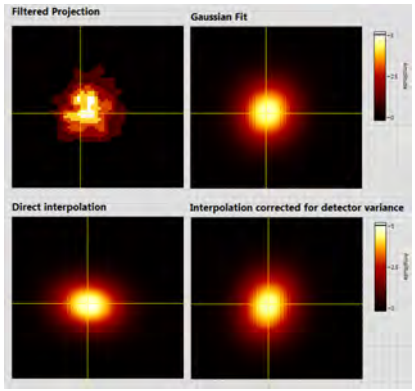

(b) Close-up view of the measured point response (upper left), fitted Gaussian (upper right), interpolated Gaussian without detector correction (lower left) and interpolated Gaussian with detector correction (lower right).

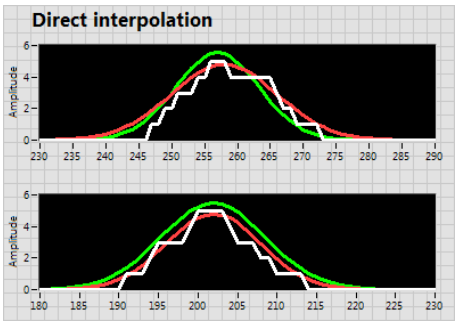

(c) Cross sections of the point response and the 2D-Gaussians (fitted and interpolated) without correcting for the detector.

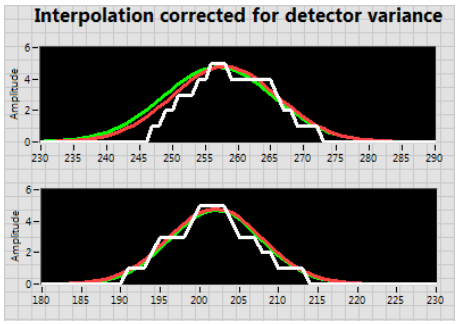

(d) Cross sections of the point response and the 2D-Gaussians (fitted and interpolated) with correction for the detector.

Figure 5.5: Results of the interpolation for the point (3,-9,-3): (a) measured response with camera placed in its middle position; (b) corresponding fitted 2D-Gaussian and interpolated Gaussians, without and with detector correction; (c) profiles of the measured response with the fitted Gaussian (in red) and the interpolated Gaussian without detector correction (in green); (d) profiles of the measured response with the fitted Gaussian (in red) and the interpolated Gaussian with detector correction (in green). In this case, it is clear that correcting for the detector covariance is crucial.

of potential bad spots increases. This also contributes to the fact that the sensitivity map for the interpolated system matrix is degraded compared to the sensitivity map for the measured system matrix. These effects should clear when cameras with repolished or retrofitted crystals are installed.

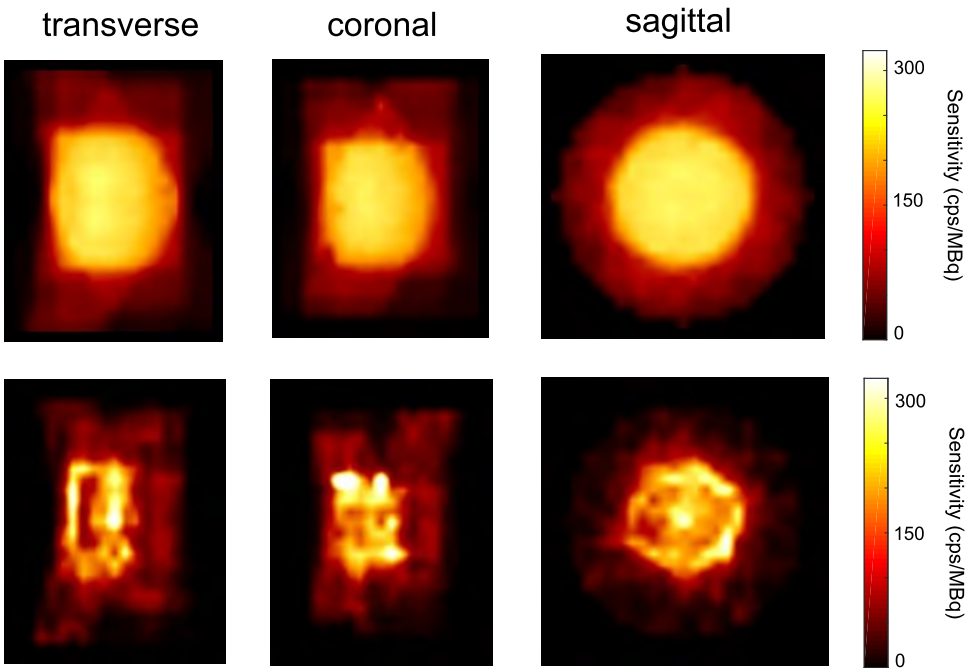

Figure 5.6: Comparison of the high-magnification configuration sensitivity maps for the measured system matrix (top row) and the interpolated system matrix (bottom row). The size of the field-of-view of the interpolated system matrix is smaller than the measured system matrix and the sensitivity itself is not as smooth.

Nevertheless, we assessed the possibility of using the interpolated system matrix in reconstructions by acquiring a Derenzo-like hot-rod phantom with three groups of rods (diameters 1.3 mm, 1.1 mm, and 0.9 mm) using the high-magnification segment of the aperture and the cameras in the middle position. We reconstructed the phantom using the MLEM algorithm with 35 iterations, both with the measured system matrix and the interpolated system matrix. The reconstruction software used here was developed in-house by Prof. Luca Caucci. The results of the reconstructions are shown in Figure 5.8 and demonstrate that it is indeed possible to reconstruct such a phantom using the interpolated system matrix. However, the slice presented here,

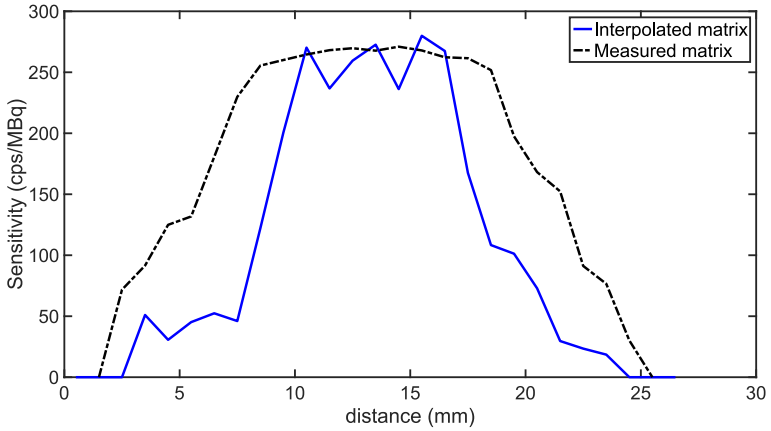

(a) Transaxial field-of-view

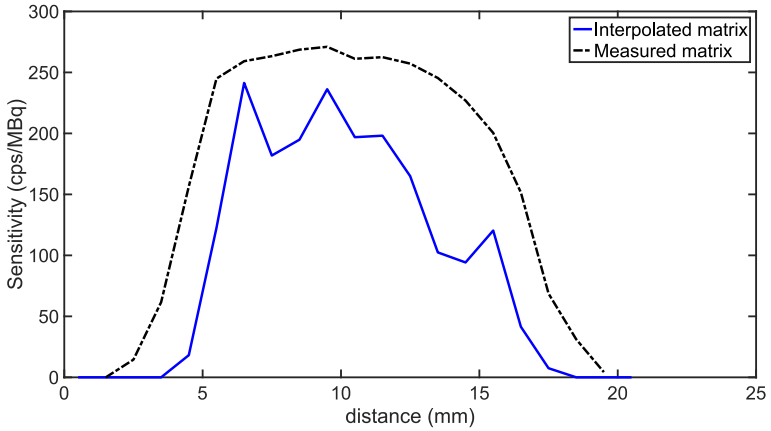

(b) Axial field-of-view

Figure 5.7: Comparison of the sensitivity profiles for the measured system matrix and the interpolated system matrix for the high-magnification, cameras in mid-position configuration. We show the transaxial sensitivity profile as well as the axial sensitivity.

which is 0.5 mm thick, shows more artifacts than the same slice for the measured system matrix. Not only on the edges of the field of view, but also at the center, were there is a "ghost rod" indicated by the green arrow. Additionally, the rods appear distorted, and as predicted from the sensitivity maps, the axial reconstruction only works for a 2 mm axial range. In comparison, the measured system matrix produces a well-reconstructed phantom over an 9 mm axial range.

Figure 5.9, shows the profiles across two groups of rods from Figure 5.8. For this particular slice at least, most of the rods are present, and they are at the

correct location. The intensity of the rods is very different, which is due partly to the fact that the sensitivities of both system matrices do not match, and partly to the fact that we saved the reconstructions in the dicom format, which loses the absolute intensity values. Nevertheless, this result is encouraging, as it shows it may indeed be possible to reconstruct a phantom using a system matrix that has been interpolated, at least for a small portion of the field of view, thus opening the imaging capabilities of adaptive systems.

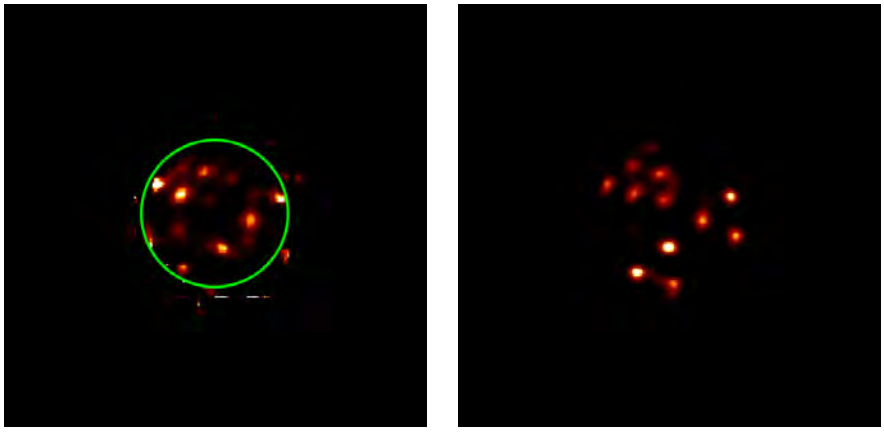

(a) Interpolated system matrix (b) Measured system matrix

Figure 5.8: Reconstruction of a Derenzo-like phantom with three groups of rods of 1.3mm, 1.1mm, and 0.9mm. In (a) we show the reconstruction using the interpolated system matrix, and in (b), we show the reconstruction using the measured system matrix. The green circle materializes the size of the field-of-view.

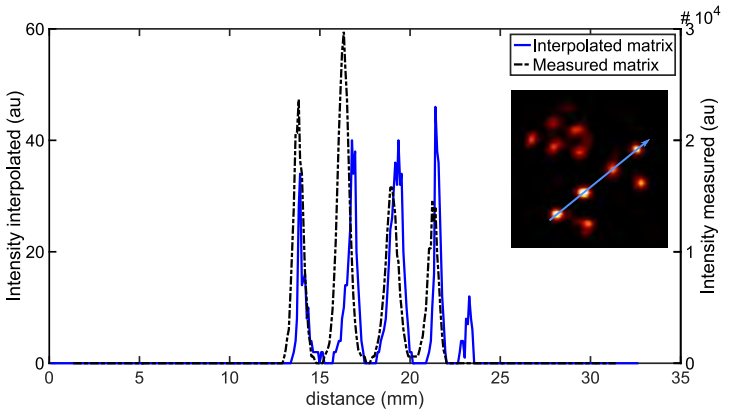

(a) Profile across line 1 from Figure 5.8a

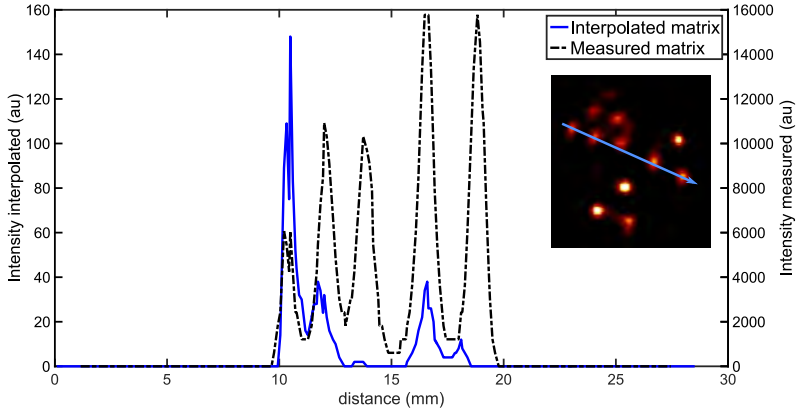

(b) Profile across line 2 from Figure 5.8a

Figure 5.9: Line profiles for the reconstructed Derenzo-like phantom. For each profile, we plot both the profile from the phantom reconstructed with the interpolated system matrix, and the profile from the phantom reconstructed with the measured system matrix. (a) shows the profile across rods 1.3mm and 1.1mm, a reconstruction artifact is visible at the edge of the field of view for the interpolated system matrix. (b) shows the profile across the 0.9mm and 1.1mm rods.

5.5 Discussion and future work

In this chapter, we have reviewed the method used to calibrate AdaptiSPECT, which consists of an exhaustive measurement of the system response on a cylindrical grid, and in interpolating the measured coefficients to create a voxel volume with a finer grid. We have also described a new interpolation scheme, specific to adaptive SPECT imaging systems where the detectors can move to multiple locations. This new interpolation scheme yields system matrices for any configuration employed during adaptive imaging, thus opening imaging possibilities to configurations that have not been measured. We showed results in terms of sensitivity, and the reconstruction of a known phantom. While we were successful in reconstructing a phantom in a small field of view, it presented reconstruction artifacts, not only at the edges of the field of view, but also at the center of the field of view. Whether these artifacts come from the interpolation method itself or are a result from the camera yellowing remains to be assessed.

This interpolation method is so far limited by the size of the field of view of the detectors when placed in the farthest position. To address this problem, it may be possible to acquire the system matrix at the nearest and farthest positions, and to use these two measurements to parameterize the position of the pinholes. The parameters would then be used to deduce a system matrix, at least for the points that are in one field of view but not the other. It is also possible to acquire a system matrix at the nearest position and a system matrix when the cameras have been moved back by a small amount, and then use these two measurements to carry out the interpolation scheme as before (which now becomes an extrapolation scheme, but the camera plane we wish to deduce from measurements does not need to be located between the measured camera planes). Further work is therefore needed on this method, to be able to exploit fully the adaptive capabilities of AdaptiSPECT.

CHAPTER 6

System Performance

This chapter aims to evaluate the imaging performance of AdaptiSPECT through measurements of the sensitivity, resolution, and size of the field of view. Since there are an infinite number of possible configurations with AdaptiSPECT, we chose to measure only a few relevant configurations to illustrate the imaging capabilities of the system. We also show results from the first mouse imaging at the end of the chapter.

All of the presented measurements were performed at the end of 2015 when the system had 12 of its 16 detectors installed. Among these 12 detectors, 4 showed little to no yellowing, 4 showed moderate amounts of yellowing, and 4 had severe amounts of yellowing (see Chapter 2). While the results presented in this chapter are still a good indication of the future performance of the system, it is likely that the performance will improve when all the cameras have been integrated and the yellowed ones have been repaired or replaced.

6.1 System Sensitivity and Field of View

For each of the configurations we evaluated, we acquired a system matrix as described in Chapter 5, Section 5.2. The acquired system matrix is normalized in cps/MBq, and therefore, the system's sensitivity is directly accessible since the sum of each column of the system matrix corresponds to the sensitivity of the corresponding voxel.

To assess the size of the field of view, we defined it in this work as being the volume where the sensitivity was within 80% of the maximum sensitivity.

6.1.1 High Magnification

We measured three camera positions with the high-magnification segment of the adaptive aperture. These configurations correspond to the nearest camera position (HM-CN), resulting in a 5.3 magnification, the middle position (HM-CM), resulting in a 8.1 magnification, and the farthest position (HM-CF), resulting in a 11.1 magnification. For each camera position, we acquired a cylindrical volume with size and step size shown in Table 6.1. We interpolated each system matrix 8 times in each dimension.

Configuration	Size of measured system matrix	Measured step	Interpolated system matrix	Voxel size
HM-CN	$21 \times 27 \times 27$	1 mm	$161 \times 209 \times 209$	0.125 mm
HM-CM	$19 \times 25 \times 25$	1 mm	$145 \times 193 \times 193$	0.125 mm
HM-CF	$17 \times 21 \times 21$	1 mm	$129 \times 161 \times 161$	0.125 mm

Table 6.1: Measured volumes and resulting system matrix sizes for the high-magnification ring-segment.

In Figure 6.1, we show the sensitivity maps for the HM-CM configuration as well as the sensitivity profiles across the central axis. These maps represent the three central planes at 1.125 mm thickness and show that the maximum measured sensitivity is 250 cps/MBq. We use the profiles to determine the size of the field of view, which is a cylinder of 12 mm diameter and 11 mm length. The small asymmetry in the transverse and coronal maps is due to the fact that 4 cameras are missing on the system at the time of acquisition.

In Figure 6.2 we show a fly-through of the sagittal slices of the volume, from back to front with respect to the axis of the imager, with 1 mm between each slice.

In Figure 6.3 we show the sensitivity maps for the HM-CN configuration, as well as the sensitivity profiles across the central axis. The maximum value of the sensitivity is 248 cps/MBq and the field of view is a cylinder of 20 mm diameter and 9 mm length.

In Figure 6.4, we show the sensitivity maps for the HM-CF configuration, as well as the sensitivity profiles across the central axis. Here, the maximum value of the

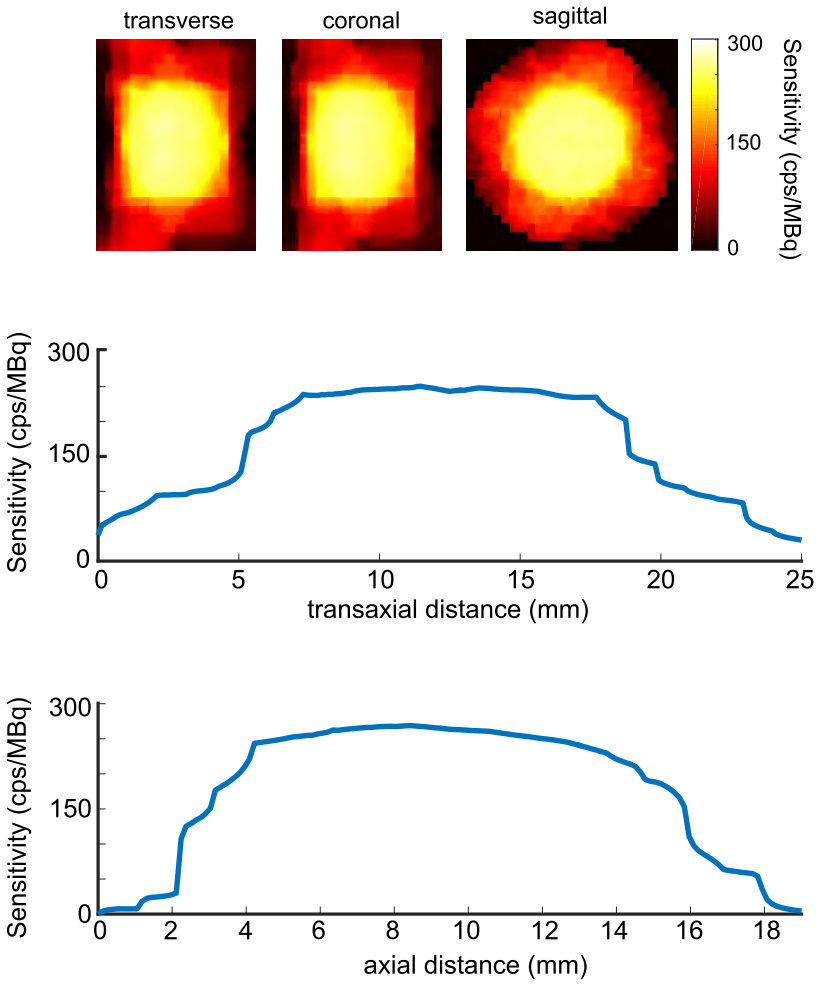

Figure 6.1: Sensitivity map for the HM-CM configuration. The central slices of the three directions (transverse, coronal, sagittal) are shown, as well as the sensitivity profiles taken from the central axes of the transverse slice.

sensitivity is 260 cps/MBq and the field of view is a cylinder of 10 mm diameter and 5 mm length.

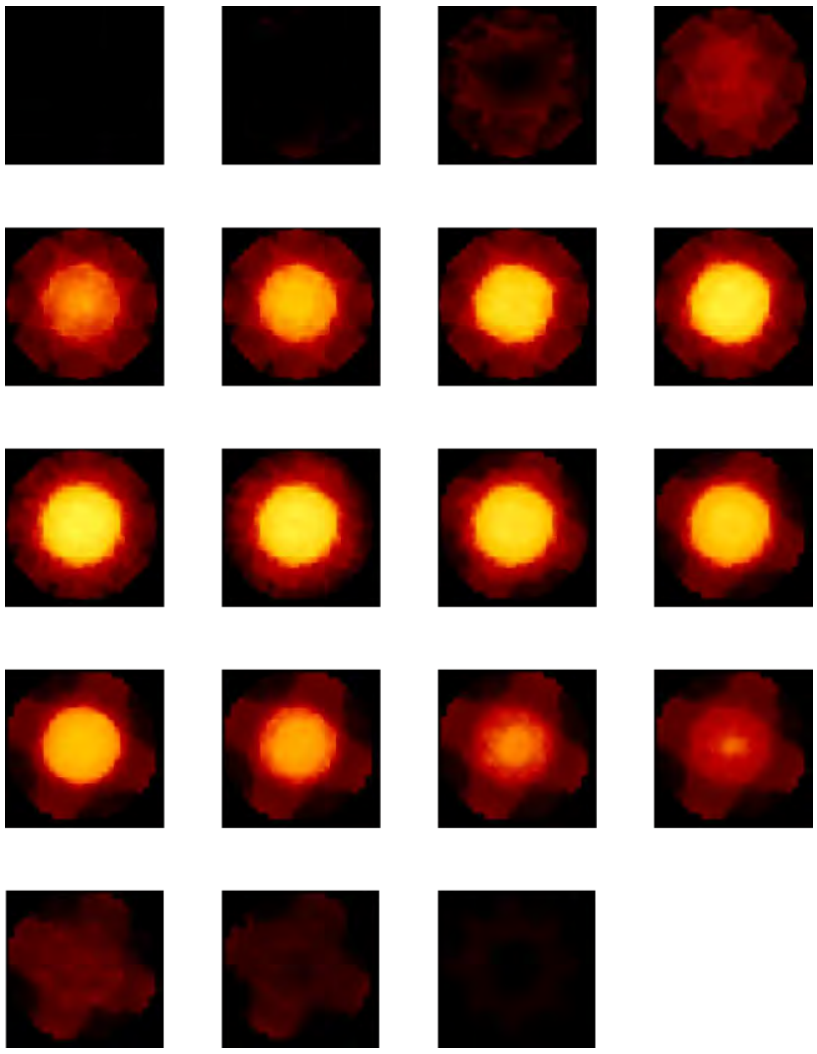

Figure 6.2: Fly-through of the sagittal slices of the sensitivity volume for the HM-CM configuration.

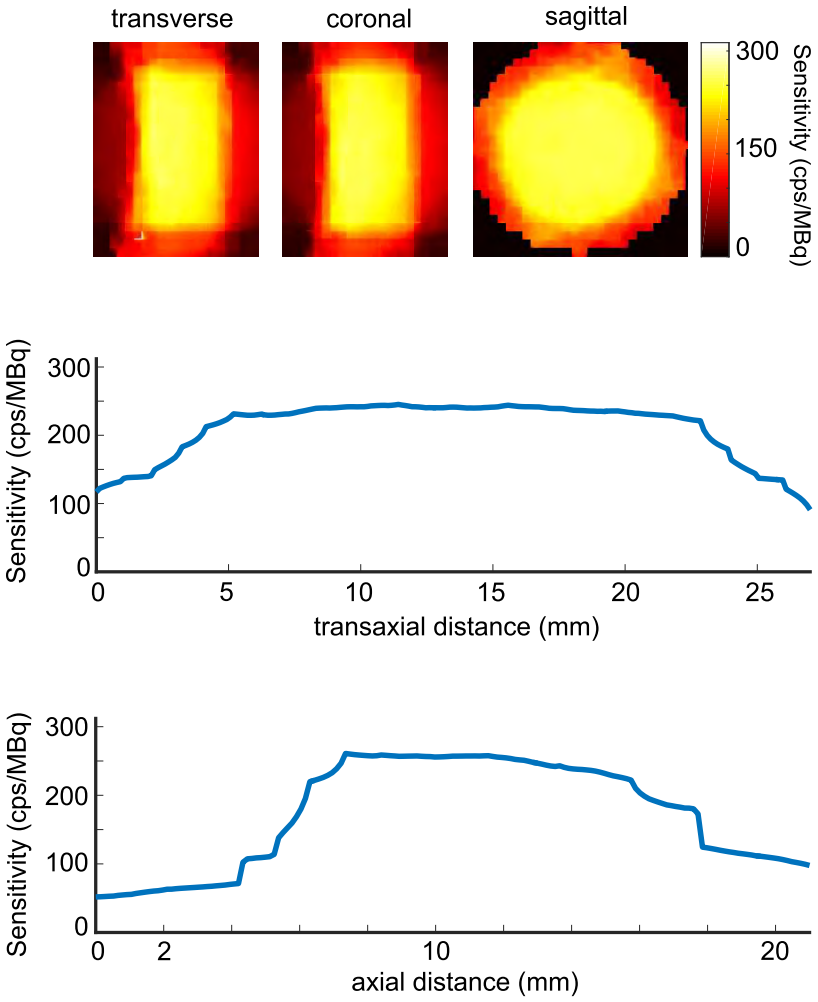

Figure 6.3: Sensitivity map for the HM-CN configuration. The central slices of the three directions (transverse, coronal, sagittal) are shown, as well as the sensitivity profiles taken from the central axes of the transverse slice.

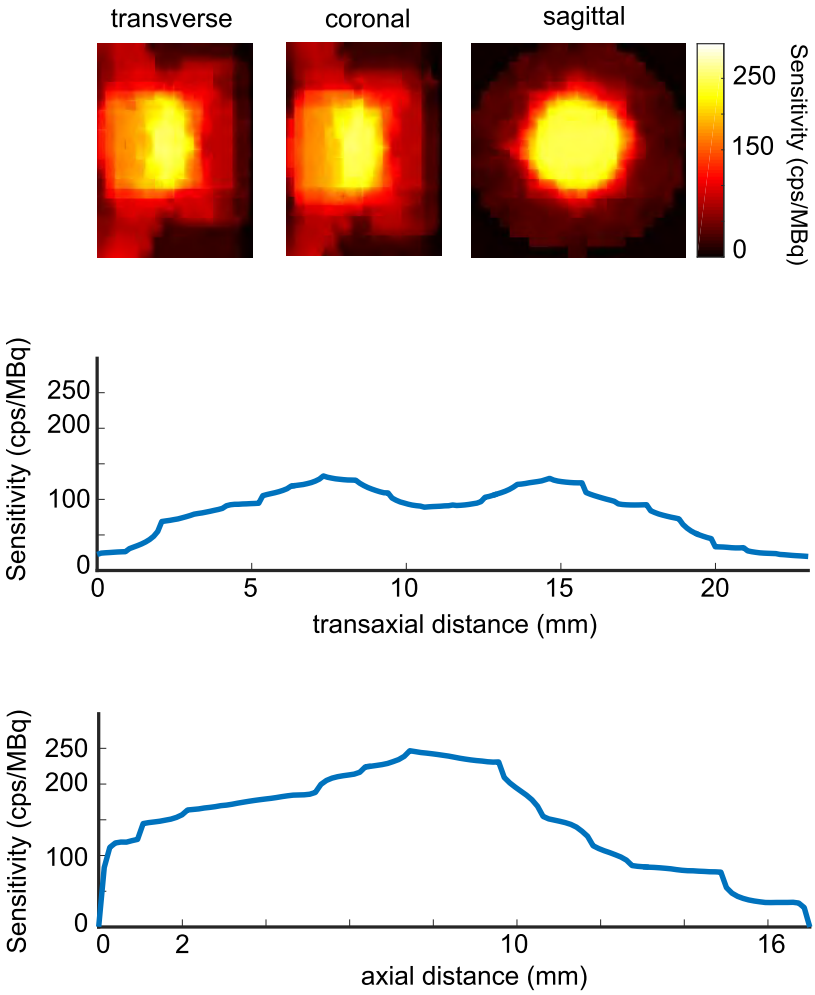

Figure 6.4: Sensitivity map for the HM-CF configuration. The central slices of the three directions (transverse, coronal, sagittal) are shown, as well as the sensitivity profiles taken from the central axes of the transverse slice.

6.1.2 Mid Magnification

We measured three camera positions with the mid-magnification segment of the adaptive aperture. These configurations correspond to the nearest camera position (MM-CN), resulting in a 1.7 magnification, the middle position (MM-CM), resulting in a 3.0 magnification, and the farthest position (MM-CF), resulting in a 4.2 magnification. For each camera position, we acquired a cylindrical volume with size and step size shown in Table 6.2. We again interpolated each system matrix 8 times in each dimension.

Configuration	Size of measured system matrix	Measured step	Interpolated system matrix	Voxel size
MM-CN	$21 \times 29 \times 29$	2 mm	$161 \times 225 \times 225$	0.25 mm
MM-CM	$21 \times 25 \times 25$	2 mm	$161 \times 193 \times 193$	0.25 mm
MM-CF	$19 \times 23 \times 23$	2 mm	$145 \times 177 \times 177$	0.25 mm

Table 6.2: Measured volumes and resulting system matrix sizes for the mid-magnification ring-segment.

In Figure 6.5, we show the sensitivity maps for the MM-CM configuration, as well as the sensitivity profiles across the central axis. The maximum sensitivity is 190 cps/MBq and the field of view is a cylinder with a 28 mm diameter and 26 mm length. In Figure 6.6, we show a fly-through of the sagittal slices of the volume, from back to front with respect to the axis of the imager, with 2 mm between each slice.

In Figure 6.7, we show the sensitivity maps for the MM-CN configuration, as well as the sensitivity profiles across the central axes. The maximum sensitivity is 185 cps/MBq and the field of view is a cylinder of 22 mm diameter and 12.5 mm length.

In Figure 6.8, we show the sensitivity maps for the MM-CF configuration, as well as the sensitivity profiles across the central axes. The maximum sensitivity is 167 cps/MBq and the field of view is a cylinder of 11 mm diameter and 10 mm length.

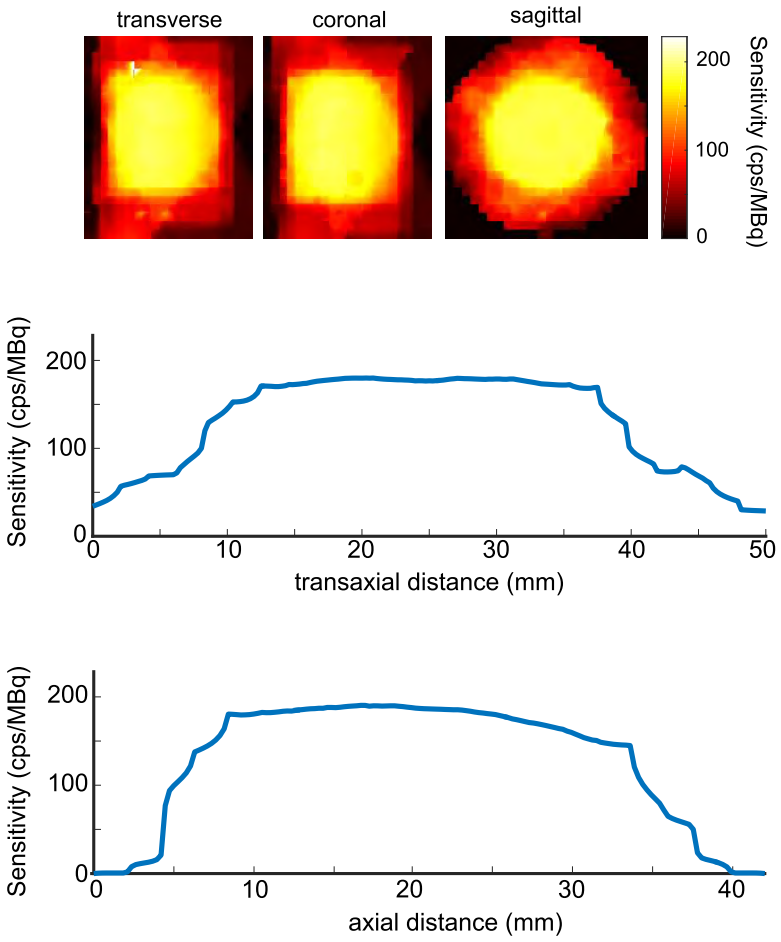

Figure 6.5: Sensitivity map for the MM-CM configuration. The central slices of the three directions (transverse, coronal, sagittal) are shown, as well as the sensitivity profiles taken from the central axes of the transverse slice.

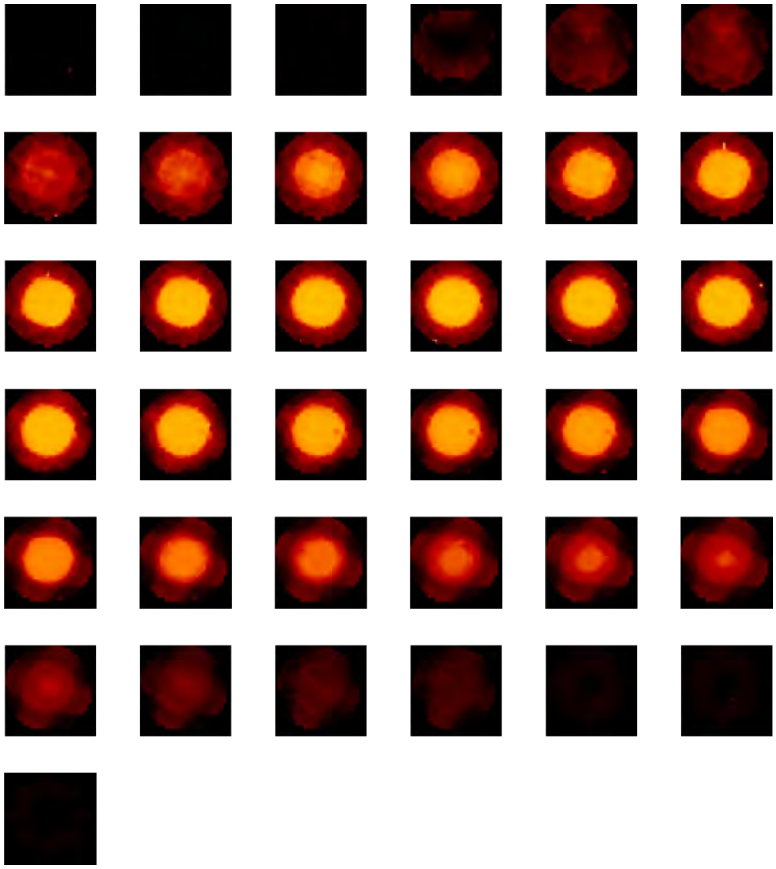

Figure 6.6: Fly-through of the sagittal slices of the sensitivity volume for the MM-CM configuration.

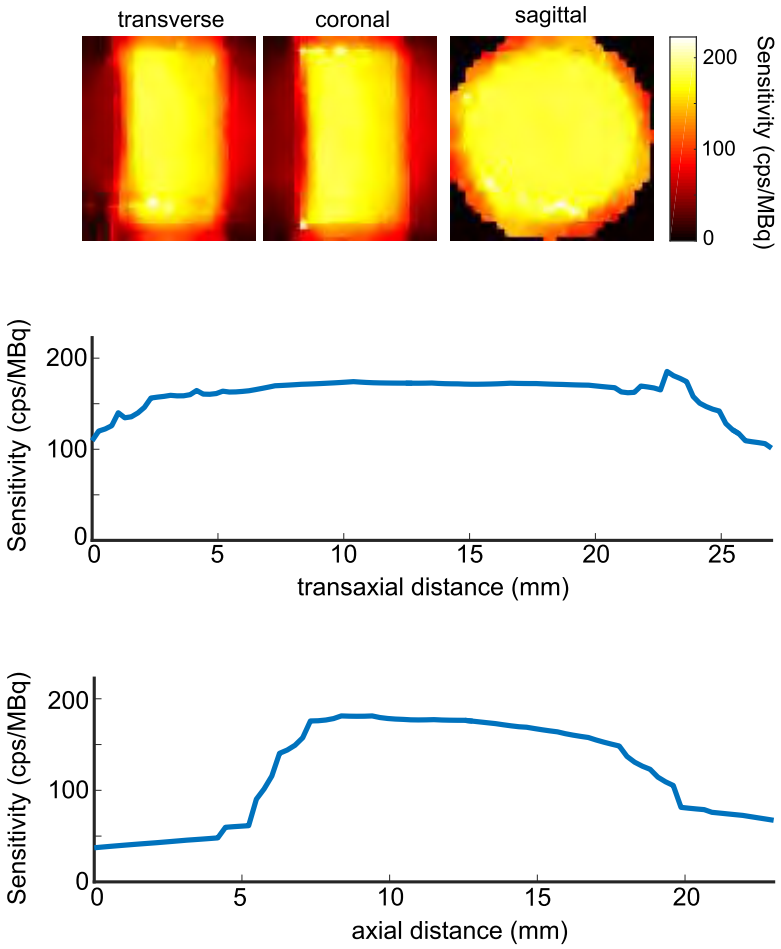

Figure 6.7: Sensitivity map for the MM-CN configuration. The central slices of the three directions (transverse, coronal, sagittal) are shown, as well as the sensitivity profiles taken from the central axes of the transverse slice.

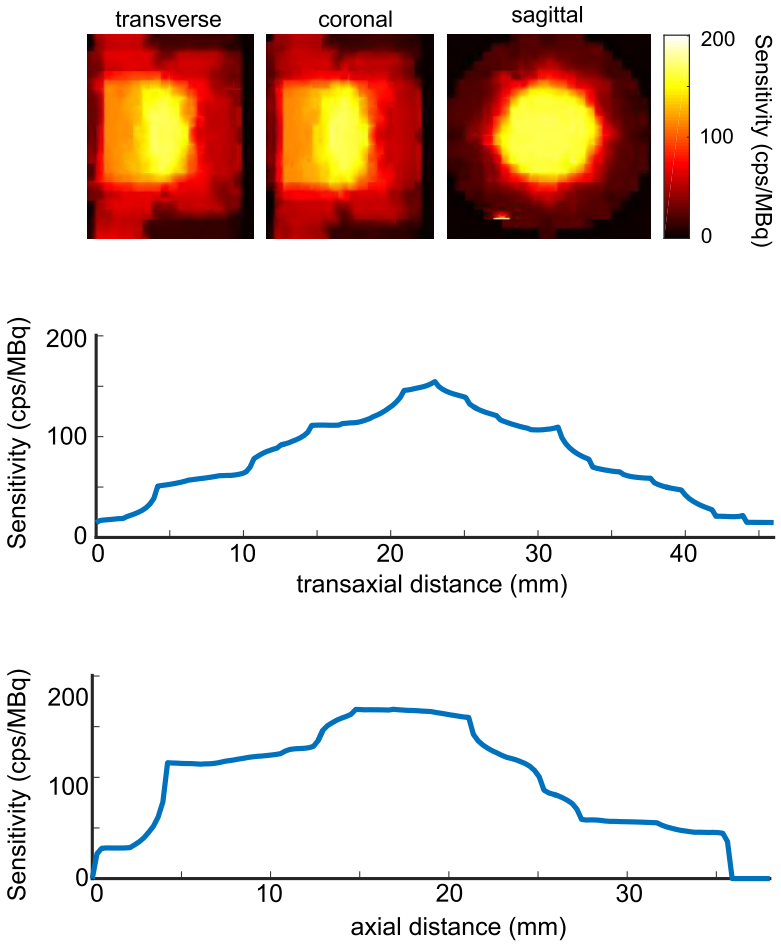

Figure 6.8: Sensitivity map for the MM-CF configuration. The central slices of the three directions (transverse, coronal, sagittal) are shown, as well as the sensitivity profiles taken from the central axes of the transverse slice.

6.1.3 Low Magnification

We measured three camera positions with the low-magnification segment of the adaptive aperture. These configurations correspond to the nearest camera position (LM-CN), resulting in a 1.2 magnification, the middle position (LM-CM), resulting in a 2.2 magnification, and the farthest position (LM-CF), resulting in a 3.2 magnification. For each camera position, we acquired a cylindrical volume with size and step size shown in Table 6.3. We interpolated each system matrix 8 times.

Configuration	Size of measured system matrix	Measured step	Interpolated system matrix	Voxel size
MM-CN	$21 \times 29 \times 29$	3 mm	$161 \times 225 \times 225$	0.375 mm
MM-CM	$21 \times 25 \times 25$	3 mm	$161 \times 193 \times 193$	0.375 mm
MM-CF	$19 \times 23 \times 23$	3 mm	$145 \times 177 \times 177$	0.375 mm

Table 6.3: Measured volumes and resulting system matrix sizes for the low-magnification ring-segment.

In Figure 6.9, we show the sensitivity maps for the LM-CM configuration, as well as the sensitivity profiles across the central axises. The maximum sensitivity is 185 cps/MBq and the field of view is a cylinder of 48 mm diameter and 44 mm length. In Figure 6.10, we show a fly-through of the sagittal slices of the volume, from back to front with respect to the axis of the imager, with 3 mm between each slice.

In Figure 6.11, we show the sensitivity maps for the LM-CN configuration, as well as the sensitivity profiles across the central axes. The maximum sensitivity is 186 cps/MBq and the field of view is a cylinder with 84 mm diameter and 40 mm length.

In Figure 6.12, we show the sensitivity maps for the LM-CF configuration, as well as the sensitivity profiles across the central axes. The maximum sensitivity is 184 cps/MBq and the field of view is 28 mm wide and 19 mm long.

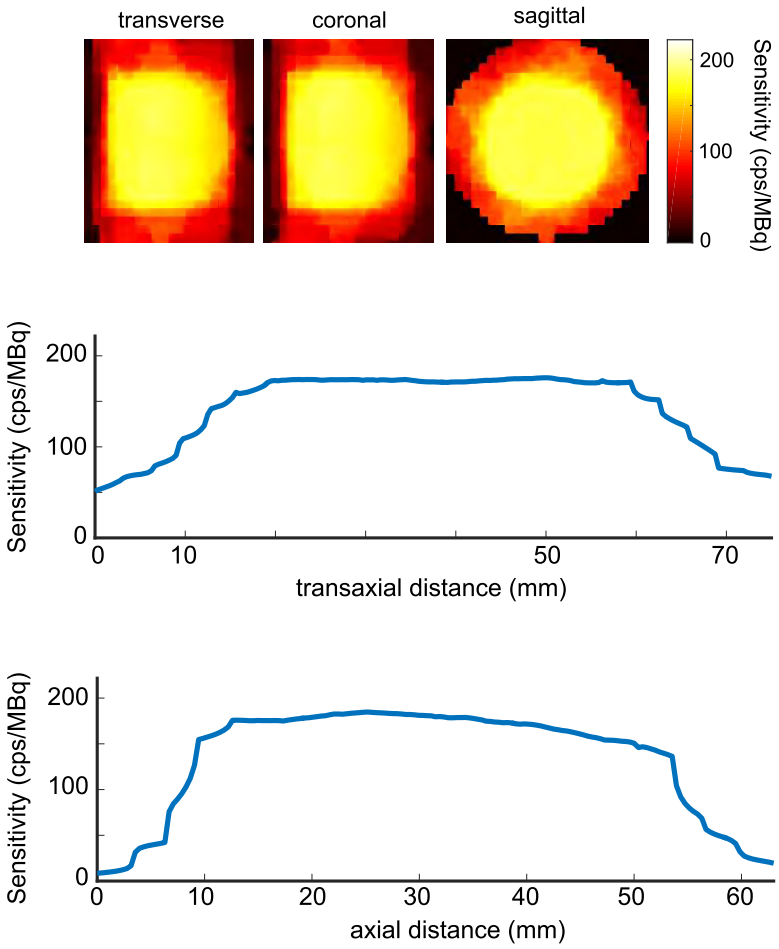

Figure 6.9: Sensitivity map for the LM-CM configuration. The central slices of the three directions (transverse, coronal, sagittal) are shown, as well as the sensitivity profiles taken from the central axes of the transverse slice.

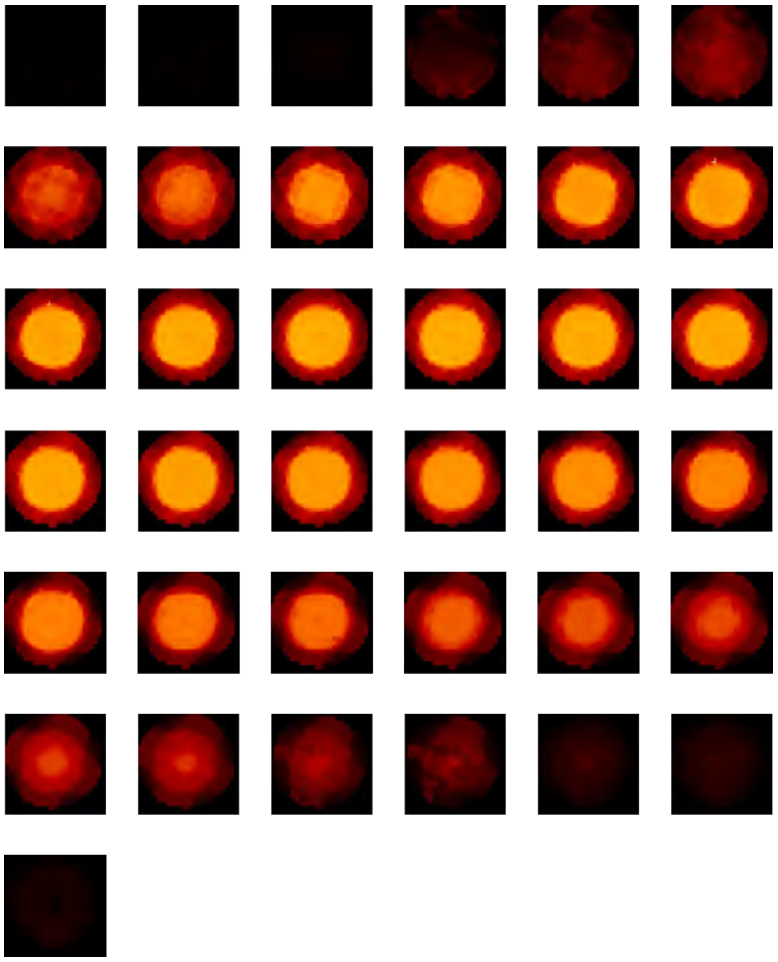

Figure 6.10: Fly-through of the sagittal slices of the sensitivity volume for the LM-CN configuration.

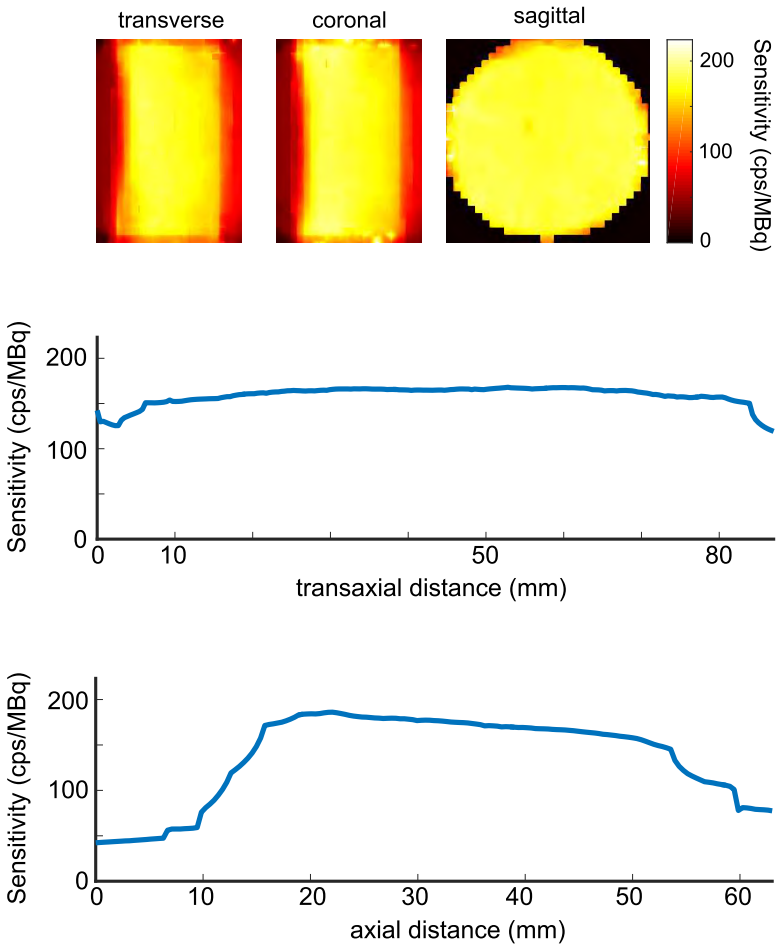

Figure 6.11: Sensitivity map for the LM-CN configuration. The central slices of the three directions (transverse, coronal, sagittal) are shown, as well as the sensitivity profiles taken from the central axes of the transverse slice.

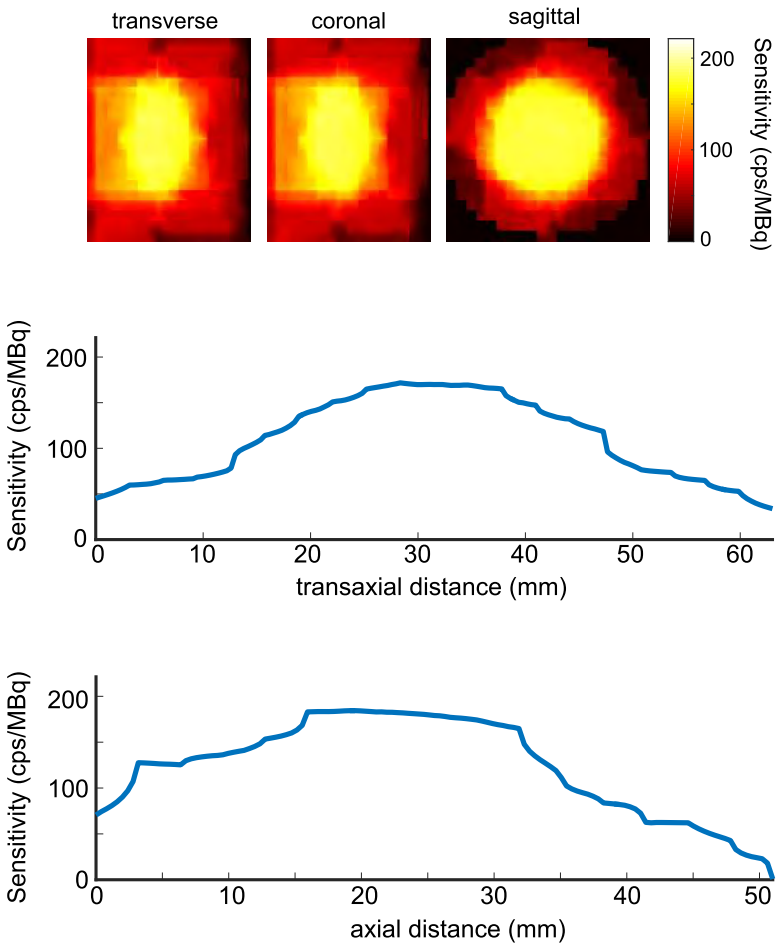

Figure 6.12: Sensitivity map for the LM-CF configuration. The central slices of the three directions (transverse, coronal, sagittal) are shown, as well as the sensitivity profiles taken from the central axes of the transverse slice.

6.1.4 Summary

We have presented results for the sensitivity and field-of-view at different configurations of AdaptiSPECT. The size of the transaxial field of view varies from 84 mm in the lowest magnification to 10 mm in the highest magnification. The sensitivity in the central slices is 190 cps/MBq for the mid- and low-magnification ring-segment configurations, and 250 cps/MBq for the high-magnification configurations. It is likely that the sensitivity will scale by a factor of 4/3 once the four missing cameras are added to the system, at least in the central planes.

The sensitivity maps presented for all configurations look satisfactorily uniform, at least for the configurations where the cameras are in the closest and middle positions. When the cameras are in the farthest position though, the quality of the sensitivity maps is degraded, probably due to the fact that we used too big of a step size when measuring the system matrices at these configurations. For instance, the LM-CF configuration results in a magnification of 3.2, which is similar to the 2.9 magnification resulting from the MM-CM configuration. Both also have similar sizes of field of view, and should be calibrated with a similar step size. We measured the LM-CF configuration with a 3 mm step size, but it would probably yield better results if measured with a 2 mm step size, as with the MM-CM configuration. Likewise, the MM-CF configuration, which results in a 4.2 magnification, is similar to the HM-CN configuration which results in a 5.3 magnification, and has a field of view of similar dimensions as the HM-CM configuration. Therefore, it should be calibrated with a step size similar than the HM-CM and HM-CN configuration. We recommend the use of a 1 mm step instead of the 2 mm step used in this work despite the extra acquisition time required. Finally, the HM-CF configuration, which results in a 11.1 magnification should be calibrated with a 0.75 or 0.5 mm step.

6.2 System Resolution

To measure the resolution of the system, we acquired and reconstructed Derenzo-like phantoms. A Derenzo phantom has an ensemble of rods of different diameters,

spaced such that the distance between the centers of two rods of the same diameter is twice the diameter of the rods. These rods are then filled with activity to create a hot rod phantom. It is also possible to fill the rest of the volume with activity, leaving the rods unfilled, creating a cold rod phantom which is generally more difficult to reconstruct. Traditionally, a Derenzo phantom comprises six groups of rods of different diameters. Such a phantom proved difficult to reconstruct on AdaptiSPECT, which currently has only 12 detectors, and only 4 non-yellowed detectors. We therefore used a sparse version of the Derenzo phantom having only 3 sets of rods. All the phantoms used for these measurements were 3D printed in a plastic polymer and the rods were then cleaned using precision micro drill bits to ensure that the rod diameters were within tolerance. The phantoms were then reconstructed using the MLEM algorithm with 50 iterations. The resolution of the system was assessed by plotting line profiles across the reconstructed phantoms to determine whether a particular group of rods was resolved or not. This is not an ideal way to define the resolution of a system, but the complete characterization of the system would require a full complement of working cameras.

6.2.1 High Magnification

For the high-magnification segment, we acquired multiple 3-segment Derenzo phantoms at the three camera positions described above. In Figure 6.13, we show a phantom that has three groups of rods of dimensions 0.8 mm, 0.7 mm and 0.6 mm imaged at the three camera positions. The effect of the change in size of field of view is visible: as the cameras are moved back, the field of view shrinks and a smaller number of rods are visible. The effect of the magnification and subsequent resolution improvement is also visible. For the camera in the nearest position (5.3 magnification, see Figure 6.13a), the rods with diameter 0.6 mm are clearly not resolved. They become more defined, but are still not fully resolved, when the camera is in the middle position (8.2 magnification, see Figure 6.13a), and are resolved when the cameras are at their farthest position (11.1 magnification, see Figure 6.13a). We conclude from this that the resolution is 0.7 mm for the HM-CN and HM-CM

configurations and 0.6 mm for the HM-CF configuration.

In Figure 6.14, we show the line profiles from the reconstruction of a sparse Derenzo phantom acquired with the HM-CM configuration (8.2 magnification). This Derenzo phantom also has three groups of rods of 0.8 mm, 0.7 mm and 0.6 mm. The line profiles show clearly that the 0.6 mm rods are not resolved. Furthermore, when looking closely at the image, it is also possible to see some faint reconstruction artifacts called "ghost rods". The origin of these artifacts could be from the camera yellowing as well as from the lack of four views.

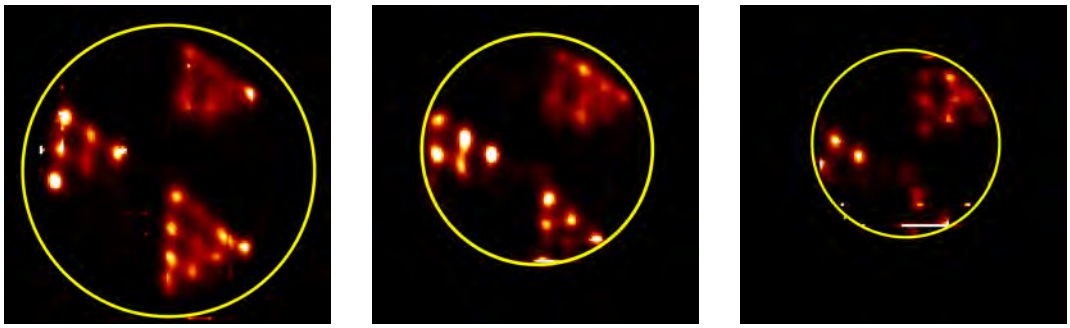

(a) HM-CN configuration (b) HM-CM configuration (c) HM-CF configuration

Figure 6.13: Reconstructions of a 3-segment Derenzo phantom with rods of sizes 0.8 mm, 0.7 mm and 0.6 mm. The same phantom was imaged for three different camera configurations with the high-magnification collimator. (a) shows the phantom for the HM-CN configuration, (b) for the the HM-CM configuration and (c) for the HM-CF configuration. The effect of changing the field of view size as the cameras are moved backwards and the improvement in the resolution are clearly visible.

6.2.2 Mid Magnification

For the mid-magnification ring segment, we only measured one camera position: the middle position, resulting in a 2.9 magnification. In Figure 6.15, we show the reconstruction of the 3-segment Derenzo phantom used to assess the resolution. The phantom used has three groups of rods of diameters 1.5 mm, 1.3 mm, and 1.1 mm. While the 1.5 mm and 1.3 mm rods are resolved, the 1.1 mm rods are not. We conclude that the resolution at this configuration is 1.3 mm.

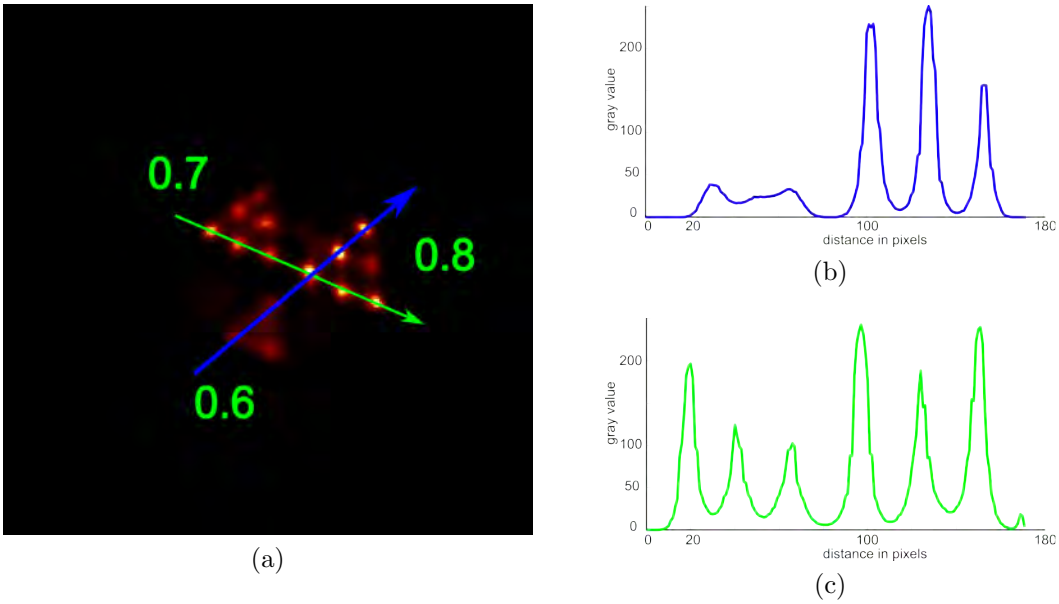

(a) (b) (c)

Figure 6.14: A 3-segment Derenzo phantoms with rods of 0.8 mm, 0.7 mm and 0.6 mm acquired with the HM-CM configuration. (a) shows the sagittal plane of the reconstruction, (b) and (c) show line profiles along two rows of rods. The 0.8 mm and 0.7 mm rods are clearly resolved, but the 0.6 mm rods are not.

6.2.3 Low Magnification

For the low-magnification ring segment, we measured three camera positions corresponding to 1.2, 2, and 3.2 magnifications. For each ring segment, we used a 3-segment Derenzo phantom that was then reconstructed using the MLEM algorithm with 50 iterations. Each reconstruction was then trimmed to eliminate the reconstruction artifacts on the edges of the field of view.

The Derenzo phantom used for the LM-CM and LM-CF has three groups of rods of 2.2 mm, 2.0 mm, and 1.8 mm diameters, and is shown in Figure 6.16. The effect of the magnification change can be seen as the 1.8 mm rods that were unresolved for the LM-CM configuration (see Figure 6.16a) become resolved in the LM-CF configuration (see Figure 6.16b). The effect of the change in size of field of view is also visible as one of the 2.0 mm rods becomes clipped in the LM-CF configuration. We conclude from this phantom that the resolution for the LM-CM configuration is 2.0 mm. We tried imaging a phantom with smaller rods in the LM-CF configuration,

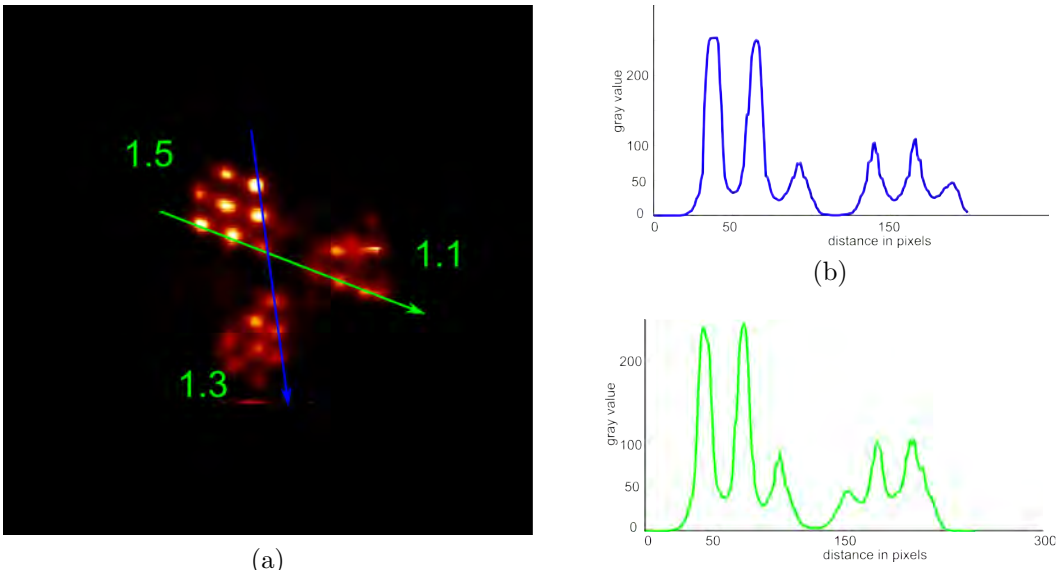

(a) (b) (c)

Figure 6.15: A 3-segment Derenzo phantom with rods of 1.5 mm, 1.3 mm and 1.1 mm acquired with the MM-CM configuration. (a) shows the sagittal plane of the reconstruction, (b) and (c) show line profiles along two rows of rods. The 1.5 mm and 1.3 mm rods are resolved, but the 1.1 mm rods are not. The line profile shows three rods present on the 1.1 mm side when there are in fact 4 rods.

but were not able to resolve them. We therefore conclude that the resolution for this configuration is 1.8 mm.

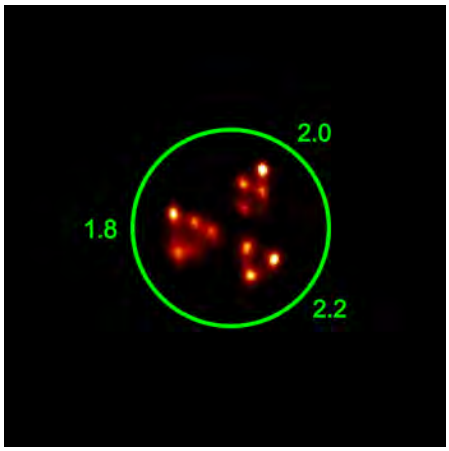

(a) LM-CM configuration

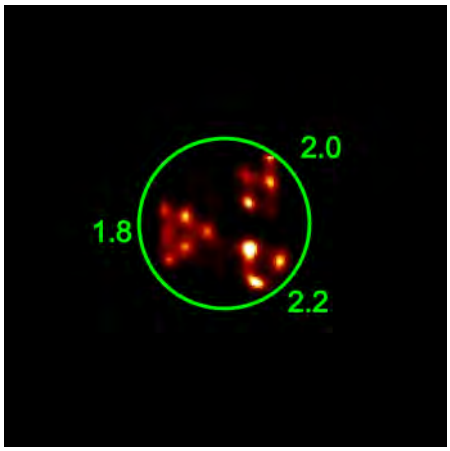

(b) LM-CF configuration

Figure 6.16: Reconstructions of a 3-segment Derenzo phantom with rods of sizes 2.2 mm, 2.0 mm and 1.8 mm. The same phantom was imaged for two different camera configurations with the low-magnification collimator. (a) shows the phantom for the LM-CM configuration and (b) for the the LM-CF configuration. The effect of changing the field of view size as the cameras are moved backwards and improvement in the resolution are clearly visible.

The phantom we used to assess the resolution of the LM-CN configuration has three groups of rods of diameters 3.8 mm, 3.5 mm, and 3.2 mm. As seen in Figure 6.17, the 3.2 mm rods are barely resolved and so we concluded that the resolution of this configuration is 3.2 mm.

6.2.4 Summary

We measured the resolution of AdaptiSPECT using 3-segment Derenzo phantoms at 7 different configurations. We found that the resolution ranges from 3.7 mm for the 1.2 magnification configuration (lowest possible magnification) to 0.6 mm for the 11.1 magnification configuration (highest possible magnification). The resolution is slightly better than expected and it is likely that the resolution will improve further when the cameras are repaired.

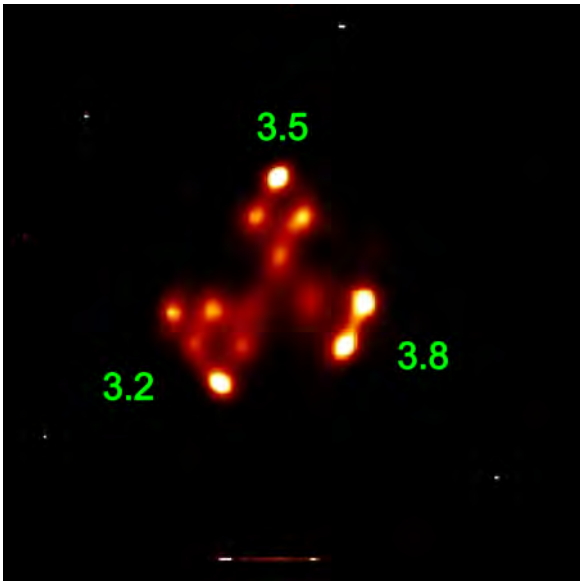

Figure 6.17: Reconstructions of a sparse Derenzo phantom with rods of sizes 3.8 mm, 3.5 mm and 3.2 mm. The phantom was imaged using the lowest magnification configuration of AdaptiSPECT, LM-CN.

6.3 Mouse Imaging

To further demonstrate the imaging capabilities of AdaptiSPECT, we imaged a mouse injected with a bone radiotracer (^{99m}Tc-MDP). The advantage of such a tracer is that it binds to bones in the entire body, making it possible to image a full-body mouse at low resolution and a high resolution region of interest within the same scan. We performed a full body scan using the LM-CM configuration, a closer view on the shoulders using the MM-CM configuration, and finally a high-resolution scan of one shoulder using the HM-CM configuration.

In Figure 6.18 we show the projection of the mouse on one camera, acquired with the LM-CN configuration, which is the lowest magnification possible on AdaptiSPECT. The entire mouse is visible at once, and although the projection is at a low resolution, it is possible to identify key features of the anatomy, such as the spine, shoulders, knees, and bladder. For adaptive SPECT imaging, such a projection could be used as a scout for easy determination and positioning of a region of

interest.

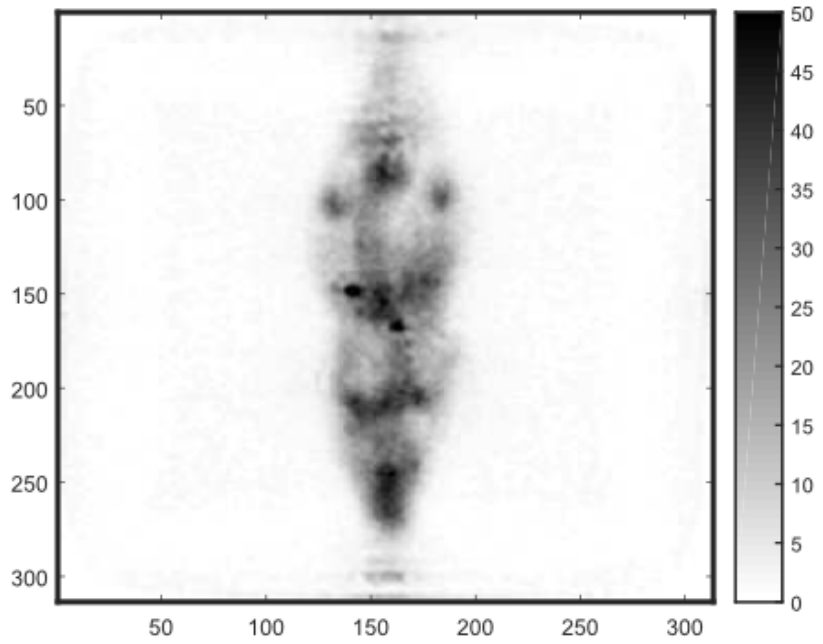

Figure 6.18: Projection of a mouse injected with a bone radiotracer on one camera with the LM-CN configuration. Some key features of the mouse anatomy are distinguishable, making such a projection interesting for a fast selection and positioning of a region of interest.

In Figure 6.19, we show the rendering of the reconstructed full body scan. The scan was performed in the LM-CM configuration using 9 bed positions, translated over the axial axis by 9 mm each. Each dataset was acquired over 7 minutes and was reconstructed using the MLEM algorithm with 50 iterations for each bed position. The 9 datasets were then combined using Amide and a volume rendering was created. The spine, shoulders, knees, and skull are visible in the reconstruction, as well as smaller features such as the legs, arms, and ribs.

From the full body scan, we further increased the magnification with the goal to image the right scapula, and to look at its structure in more detail. In Figure 6.20, we show the rendering of the reconstructed close-up view of the scapulas acquired

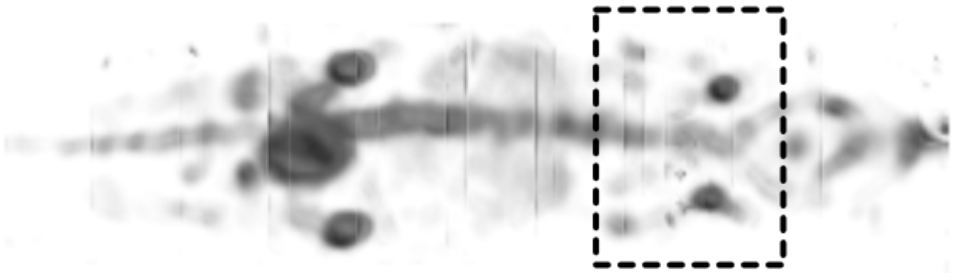

(a) Top view

(b) Side view

Figure 6.19: Full body scan of a mouse injected with a bone radiotracer. The scan was acquired using 9 bed positions translated by 9 mm each on the central axis of the system. This scan was reconstructed using the MLEM algorithm over 50 iterations. The boxed area on the top view materializes the field of view shown in Figure 6.20.

in the MM-CM configuration side by side with one of the LM-CM bed positions for comparison. The base of the skull is now more detailed and it is possible to distinguish individual vertebrae on the spine as well as individual rib attachment locations on the sternum, neither of which were visible in the LM-CM reconstruction.

Finally, we increased the magnification to 8.2 using the HM-CM configuration. The right shoulder was placed in the center of the field of view using the MM-CM configuration and the mouse was not moved after the aperture was changed to the high-magnification ring segment. It is difficult to position a feature of interest using a very small field of view, but it is easy to do in a lower magnification configuration, achieving one of the objectives of AdaptiSPET. In Figure 6.21, we show the rendering of the shoulder acquired at the HM-CM configuration side by side with the rendering of the same shoulder acquired in the MM-CM configuration. Although

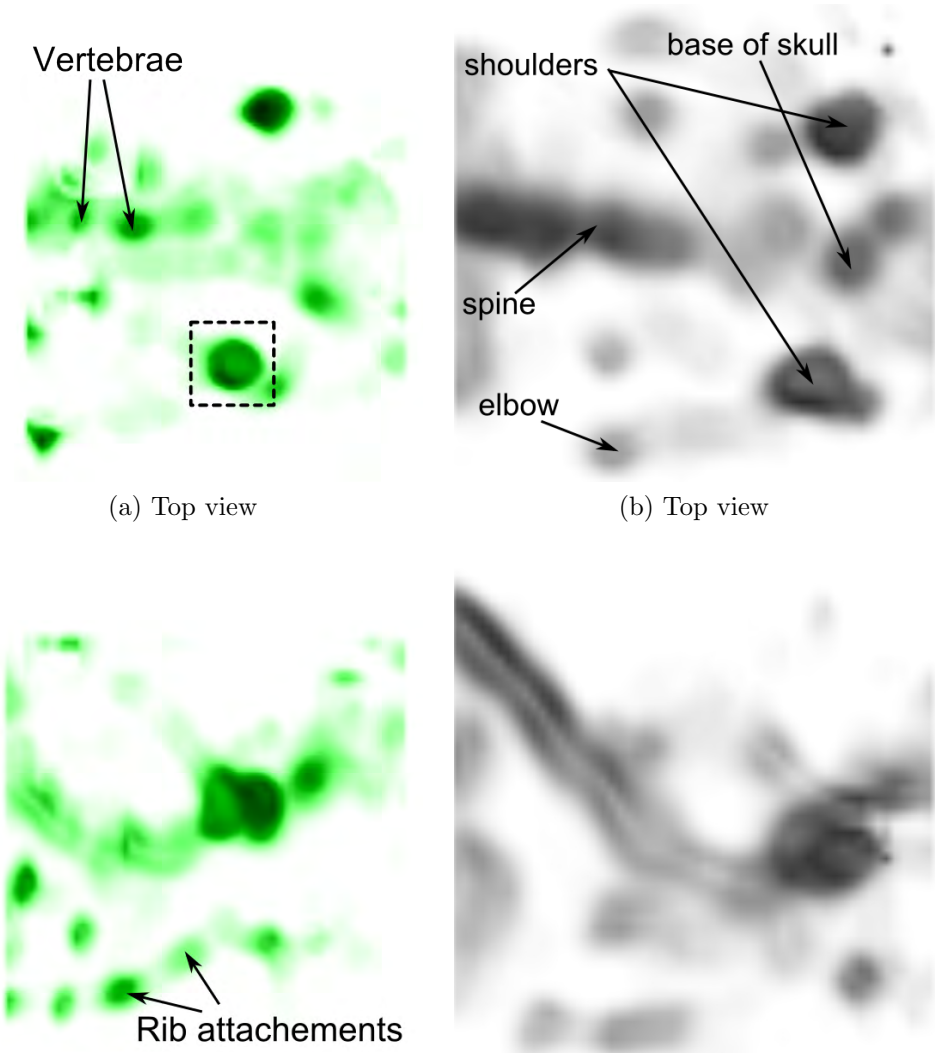

(a) Top view

(b) Top view

(c) Side view

(d) Side view

Figure 6.20: Reconstruction of a mouse injected with a bone radiotracer. (a) and (c) show the top and side view of a volume rendering of the mouse acquired with the MM-CM configuration. (b) and (d) show the same region acquired with the LM-CM configuration. The increased magnification allows for resolving individual vertebrae and individual rib attachment locations on the sternum. The boxed area materializes the field of view shown in Figure 6.21.

the field-of-view at the HM-CM configuration allows for imaging a portion of the spine in addition to the shoulder, we decided to focus on the shoulder in order to see its structure. The increased resolution in the high-magnification image allows

resolution of fine features not present in the low magnification configuration such as the head of the humerus and details of the scapula.

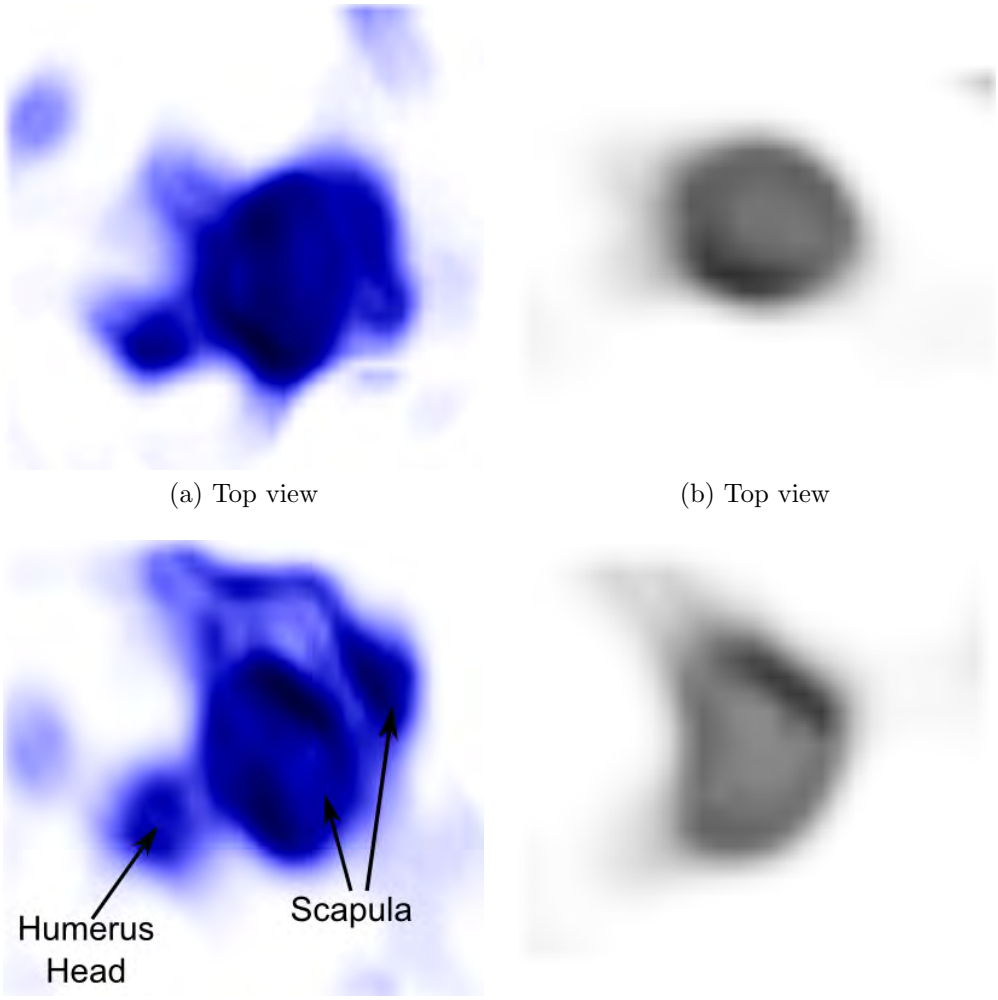

(a) Top view

(b) Top view

(c) Side view

(d) Side view

Figure 6.21: Rendering of a reconstruction of the right shoulder of mouse injected with a bone radiotracer. (a) and (c) show the top and side view of the rendering for the dataset acquired with the HM-CM configuration, (b) and (d) show the same shoulder, acquired with the LM-CM configuration. Increasing the magnification revealed the head of the humerus and details in the scapula.

6.4 Conclusions

We have assessed the imaging capabilities of AdaptiSPECT and the results are summarized in Table 6.4. In the table we also added the expected sensitivity we will achieve with 16 cameras. To summarize, the magnification ranges from 1.2 to 11.1 with a corresponding resolution ranging from 3.2 mm to 0.6 mm. The field of view ranges from 84 mm $\times$ 48 mm to 10 mm $\times$ 5 mm, and the sensitivities, which are satisfactorily uniform over the field of view range from 190 cps/MBq for the low- and mid-magnification configurations to 250 cps/MBq for the high-magnification ring segment.

We performed mouse imaging for a mouse injected with a bone radiotracter and were successful in reconstructing full-body scans, as well as scans performed at higher magnifications. We were also successful in using lower magnification configurations to place the region of interest (the right shoulder) into the center of the field of view for higher magnification configurations.

We also assessed the step sizes and dimensions that are needed to calibrate AdaptiSPECT. While the dimensions we used in this work proved to be adequate, they were not optimal. As we have previously, the LM-CF configuration should be scanned with a 2 mm step, the MM-CF configuration should be scanned with a 1 mm step, and the HM-CF configuration should be scanned with a 0.5 mm step. This will provide for smoother sensitivity maps and likely lead to improvements in the reconstructions.

Imager Configuration	LMag			MMag			HMag		
detector distance (mm)	165.1	241.3	317.5	165.1	241.3	317.5	165.1	241.3	317.5
magnification	1.2	2	3.2	1.7	2.9	4.2	5.3	8.2	11.1
resolution (mm)	3.2	2.0	1.8	-	1.3	-	0.7	0.7	0.6
transaxial FOV (mm)	84	48	28	22	28	11	19	12	10
axial FOV (mm)	40	44	19	12	26	10	9	11	5
sensitivity (cps/MBq)	186	184	184	185	190	167	260	250	248
sensitivity 16 (cps/MBq)	248	245	245	247	253	223	347	334	330

Table 6.4: Measured properties of AdaptiSPECT.

CHAPTER 7

Conclusions and Future Work

In this dissertation, we have developed a new and unique pre-clinical SPECT imaging system that can change its configuration during a scan to adapt to the data it is acquiring. 12 of 16 of the system's detectors are installed and we addressed the problems encountered with crystal yellowing as well as the method we used to process the list-mode data to minimize the resulting artifacts. The key element of AdaptiSPECT is the design and fabrication of the adaptive pinhole aperture. The aperture consists of three axially arranged ring-segments sized for small animal studies, ranging from mice to rats. Selection of the proper ring-segment is done by translating the entire aperture on its axis. The aperture is also comprised of shutter systems to open or close additional pinholes on some sections of the aperture. A control system was developed to drive and adjust the adaptive features. We evaluated the precision and repeatability of the positioning when changing configurations and found that it met tolerances required for imaging. A calibration method used to acquire the set of system matrices necessary for reconstructions, detection and estimation tasks, as well as adaptation methods was described. We proposed a way to extend the calibration method to adaptive systems and evaluated the performance of this method. Finally, we assessed the performance of the system by measuring its sensitivity, resolution, and field-of-view size. Figure 7.1 shows the performance of various AdaptiSPECT configurations in a similar fashion to how we showed the performance of various systems reported in the literature in Chapter 1. To summarize, the resolution ranges from 3.2 mm in the lowest magnification configuration to 0.6 mm in the highest magnification configuration. Likewise, the size of the transaxial field of view ranges from 85 mm in the lowest magnification configuration to 10 mm in the highest magnification configuration. We also performed imaging on a mouse injected with a bone radiotracer using different configurations

and showed that the increase in magnification, and thus resolution, leads to finer bone structures being revealed.

The development of AdaptiSPECT was a success in that we were able to build an adaptive SPECT imaging system as well as to design controllers that drive the autonomous adaptation and achieve reproducibility in the critical positioning parameters.

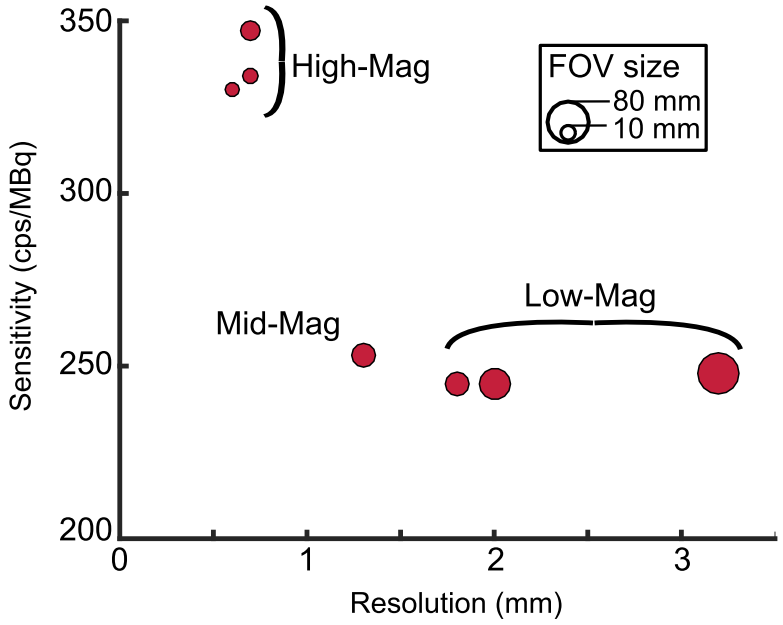

Figure 7.1: Scatter plot of the AdaptiSPECT imaging performances.

7.1 Future work

The first and most obvious item that has to be addressed on AdaptiSPECT is the refurbishing of all yellowed cameras and the installation of the four missing cameras. AdaptiSPECT will also need to be fitted with its lead skin to reduce background counts and improve the imaging of small-animals. In the future, AdaptiSPECT will need to be mated with the adaptive CT system, FaCT [125], to allow for multi-modality imaging [44, 126].

An effort will also have to be devoted to developing an efficient software pack-

age that can communicate with both the adaptation algorithm and the hardware while still performing list-mode acquisitions. To facilate this development, the hardware control software written during this dissertation was implemented using best practice object-oriented design principles. Accordingly, development time for future communication software should be reduced.

Finally, another effort will have to be made to jointly reconstruct multiple datasets acquired at different magnifications.

7.2 Towards autonomous adaptation

AdaptiSPECT is designed to allow various adaptation approaches to be implemented: for the distance of the pinholes to the center of the field of view and the pinhole diameters, the choice is of course reduced to three configuration, but the distance of the detectors to the central axis can vary continuously, and can be different for each projection angle. Therefore, AdaptiSPECT is well suited to implement the different modes of adaptation that have been described in [17]. Here we will describe the three main adaptation schemes that are suitable for adaptive SPECT.

In the single-step adaptation scheme illustrated in Figure 7.2, the adaptive SPECT system acquires a preliminary dataset g_s in a scout configuration $\mathcal{H}_s$. Using the information from this scout dataset, and with knowledge of the task to accomplish, the system will compute the best configuration to achieve maximum performance on the task. The adaptive SPECT system will then reconfigure in its diagnostic configuration $\mathcal{H}_s$ and acquire the dataset used for the diagnostic g_d. This scheme would enable a good implementation of the *choice among known systems* mode of adaptation. On AdaptiSPECT for example, a set of fifteen $\mathbf{H}$ matrices could be measured (five camera positions per ring segment), and during the adaptation step, the $\mathbf{H}$ matrix that provides the highest performance would be selected.

To implement such an adaptation scheme, it is necessary to develop figures of merit that can accurately assess whether one configuration is better than another

for the imaging task. Traditional task-based figures of merit can be very slow to compute and, therefore, surrogate figures of merit that are simpler to compute need to be developed [45, 47].

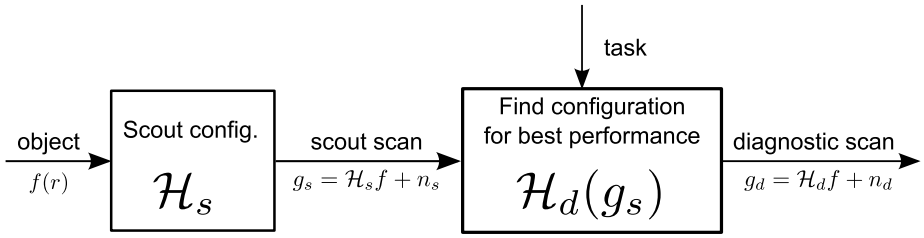

Figure 7.2: Flowchart for single-step adaptation. A scout scan is performed first, the best configuration to achieve maximum performance is computed, and the system is reconfigured before acquiring the diagnostic task.

Instead of having a single adaptation step, the system could also do multiple adaptations, as illustrated in Figure 7.3, and in this case, the adaptation could be near-continuous. For example, every two seconds a decision could be made to move a detector, open a shutter, or move the object given the data that has just been acquired and knowledge of the task to perform. This approach is well suited for adaptive SPECT since the distribution of the radiotracer in the tissue is evolving continuously during the acquisition and the system itself has the ability to perform dynamic studies.

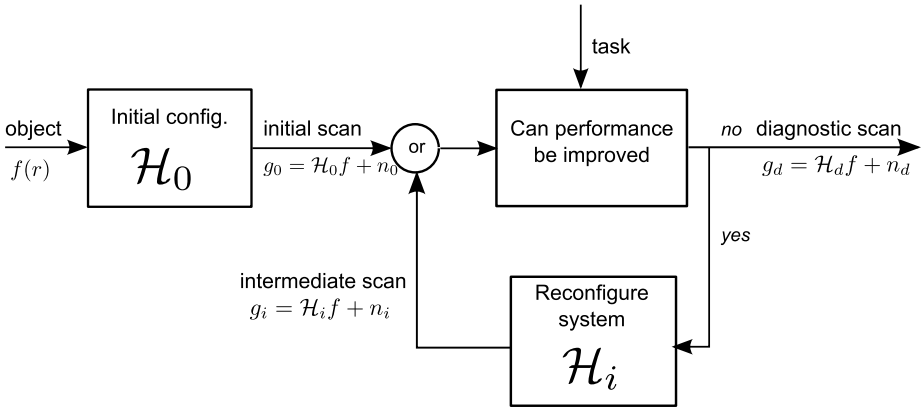

Figure 7.3: Flowchart for single step adaptation.

Finally, all adaptive systems can develop adaptation rules through learning meth-

ods. In this case, the system has to be trained, either through experimentation or through simulations with good models. Furthermore, the system has to keep some sort of memory of the data acquired, the adaptation steps made, and the assessment of the acquisition.

7.3 Final words

In this work, we have brought the concept of an adaptive SPECT imaging system as it was originally described by Barrett *et al.* [17] to life. We have engineered a system that can switch configurations with speed, precision, and repeatability suitable to carry out adaptive imaging studies on small animals, thus opening the door to a new research and medical imaging paradigm in which the imager hardware is adjusted on the fly to maximize task-performance for a specific patient, not, as currently, an ensemble of patients.

REFERENCES

[1] 3D Systems Layerwise, B. (2014). website: http://www.layerwise.com.

[2] Aarsvold, N., H. Barrett, J. Chen, L. Landesman, D. Milster, K. Rowe, M. Strimbu, D. D. Patton, and T. J. Roney (1988). Modular scintillation cameras: a progress report. In *SPIE Medical Imaging II*, volume 914, pp. 319–325.

[3] Accorsi, R., M. Autiero, L. Celentano, M. Chmeissani, R. Cozzolino, a. S. Curion, P. Frallicciardi, P. Laccetti, R. C. Lanza, a. Lauria, M. Maiorino, M. Marotta, G. Mettivier, M. C. Montesi, P. Riccio, G. Roberti, and P. Russo (2007). MediSPECT: Single photon emission computed tomography system for small field of view small animal imaging based on a CdTe hybrid pixel detector. *Nuclear Instruments and Methods in Physics Research, Section A: Accelerators, Spectrometers, Detectors and Associated Equipment*, **571**(1-2 SPEC. ISS.), pp. 44–47. ISSN 01689002. doi:10.1016/j.nima.2006.10.025.

[4] Accorsi, R., F. Gasparini, and R. C. Lanza (2001). Optimal coded aperture patterns for improved SNR in nuclear medicine imaging. *Nuclear Instruments and Methods in Physics Research, Section A: Accelerators, Spectrometers, Detectors and Associated Equipment*, **474**(3), pp. 273–284. ISSN 01689002. doi: 10.1016/S0168-9002(01)01326-2.

[5] Accorsi, R. and S. D. Metzler (2004). Analytic determination of the resolution-equivalent effective diameter of a pinhole collimator. *IEEE transactions on medical imaging*, **23**(6), pp. 750–63. ISSN 0278-0062. doi:10.1109/TMI.2002.803129.

[6] Accorsi, R., J. R. Novak, A. S. Ayan, and S. D. Metzler (2008). Derivation and validation of a sensitivity formula for slit-slat collimation. *IEEE Transactions*

on Medical Imaging, **27**(5), pp. 709–722. ISSN 02780062. doi:10.1109/TMI.2007.912395.

[7] Andringa, G., B. Drukarch, J. G. J. M. Bol, K. de Bruin, K. Sorman, J. B. a. Habraken, and J. Booij (2005). Pinhole SPECT imaging of dopamine transporters correlates with dopamine transporter immunohistochemical analysis in the MPTP mouse model of Parkinson's disease. *NeuroImage*, **26**(4), pp. 1150–8. ISSN 1053-8119. doi:10.1016/j.neuroimage.2005.03.034.

[8] Anger, H. O. (1958). Scintillation camera. *Review of Scientific Instruments*, **29**(1), pp. 27–33. ISSN 00346748. doi:10.1063/1.1715998.

[9] Auricchio, A., P. D. Acton, M. Hildinger, J.-P. Louboutin, K. Plössl, E. O'Connor, H. F. Kung, and J. M. Wilson (2003). In vivo quantitative noninvasive imaging of gene transfer by single-photon emission computerized tomography. *Human gene therapy*, **14**(3), pp. 255–61. ISSN 1043-0342. doi:10.1089/10430340360535805.

[10] Barber, H. and J. Woolfenden (1996). Semiconductor detectors in nuclear medicine: progress and prospects. *Nuclear Medicine*, pp. 168–184.

[11] Barber, H. B., B. A. Apotovsky, F. L. Augustine, H. H. Barrett, E. L. Dereniak, F. P. Doty, J. D. Eskin, W. J. Hamilton, D. G. Marks, K. J. Matherson, J. E. Venzon, J. M. Woolfenden, and E. T. Young (1997). Semiconductor pixel detectors for gamma-ray imaging in nuclear medicine. *Nuclear Instruments & Methods in Physics Research Section a-Accelerators Spectrometers Detectors and Associated Equipment*, **395**(3), pp. 421–428. ISSN 01689002 (ISSN). doi:Doi10.1016/S0168-9002(97)00615-3.

[12] Barber, H. B., D. G. Marks, B. A. Apotovsky, F. L. Augustine, H. H. Barrett, J. F. Butler, E. L. Dereniak, F. P. Doty, J. D. Eskin, W. J. Hamilton, K. J. Matherson, J. E. Venzon, J. M. Woolfenden, and E. T. Young (1996). Progress in developing focal-plane-multiplexer readout for large

CdZnTe arrays for nuclear medicine applications. *Nuclear Instruments and Methods in Physics Research, Section A: Accelerators, Spectrometers, Detectors and Associated Equipment*, **380**(1-2), pp. 262–265. ISSN 01689002. doi: 10.1016/S0168-9002(96)00472-X.

[13] Barrett, H. H. (1990). Objective assessment of image quality: effects of quantum noise and object variability. *Journal of the Optical Society of America. A, Optics and image science*, **7**(7), pp. 1266–78. ISSN 0740-3232.

[14] Barrett, H. H., C. K. Abbey, and E. Clarkson (1998). Objective assessment of image quality . III . ROC and likelihood-generating functions. *Journal of the Optical Society of America*, **15**(6), pp. 1520–1535.

[15] Barrett, H. H., J. L. Denny, R. F. Wagner, and K. J. Myers (1995). Objective assessment of image quality. II. Fisher information, Fourier crosstalk, and figures of merit for task performance. *Journal of the Optical Society of America. A, Optics, image science, and vision*, **12**(5), pp. 834–52. ISSN 1084-7529.

[16] Barrett, H. H., J. Eskin, and H. Barber (1995). Charge Transport in Arrays of Semiconductor Gamma-Ray Detectors. *Physical Review Letters*, **75**(1), pp. 156–159. ISSN 0031-9007. doi:10.1103/PhysRevLett.75.156.

[17] Barrett, H. H., L. R. Furenlid, M. Freed, J. Y. Hesterman, M. a. Kupinski, E. Clarkson, and M. K. Whitaker (2008). Adaptive SPECT. *IEEE transactions on medical imaging*, **27**(6), pp. 775–88. ISSN 1558-254X. doi: 10.1109/TMI.2007.913241.

[18] Barrett, H. H. and F. A. Horrigan (1973). Fresnel zone plate imaging of gamma rays; theory. *Applied optics*, **12**(11), pp. 2686–702. ISSN 0003-6935.

[19] Barrett, H. H. and W. C. J. Hunter (2005). Detecors for Small-Animal SPECT I. In Kupinski, M. A. and H. H. Barrett (eds.) *Small-Animal SPECT Imaging*, chapter 2, pp. 9–48. Springer.

[20] Barrett, H. H., W. C. J. Hunter, B. W. Miller, S. K. Moore, Y. Chen, and L. R. Furenlid (2009). Maximum-Likelihood Methods for Processing Signals From Gamma-Ray Detectors. *IEEE transactions on nuclear science*, **56**(3), p. 725. ISSN 0018-9499.

[21] Barrett, H. H. and K. J. Myers (2003). *Foundations of Image Science*. Wiley-VCH. ISBN 0-471-15300-1.

[22] Barrett, H. H. and W. Swindell (1996). *Radiological imaging: theory of image formation, detection and processing.* New York, NY, academic p edition.

[23] Barrett, H. H., T. White, and L. C. Parra (1997). List-mode likelihood. *Journal of the Optical Society of America. A, Optics, image science, and vision*, **14**(11), pp. 2914–23. ISSN 1084-7529.

[24] Beekman, F. and F. van der Have (2007). The pinhole: gateway to ultra-high-resolution three-dimensional radionuclide imaging. *European journal of nuclear medicine and molecular imaging*, **34**(2), pp. 151–61. ISSN 1619-7070. doi:10.1007/s00259-006-0248-6.

[25] Beekman, F. J., C. Kamphuis, and E. C. Frey (1997). Scatter compensation methods in 3D iterative SPECT reconstruction: a simulation study. *Physics in medicine and biology*, **42**(8), pp. 1619–1632. ISSN 0031-9155. doi:10.1088/0031-9155/42/8/011.

[26] Beekman, F. J., F. van der Have, B. Vastenhouw, A. J. a. van der Linden, P. P. van Rijk, J. P. H. Burbach, and M. P. Smidt (2005). U-SPECT-I: a novel system for submillimeter-resolution tomography with radiolabeled molecules in mice. *Journal of Nuclear Medicine*, **46**(7), pp. 1194–1200. ISSN 0161-5505. doi:46/7/1194[pii].

[27] Bennink, R. J., J. Hamann, K. de Bruin, F. J. W. ten Kate, S. J. H. van Deventer, and A. a. te Velde (2005). Dedicated pinhole SPECT of intestinal neutrophil recruitment in a mouse model of dextran sulfate sodium-induced

colitis. *Journal of nuclear medicine : official publication, Society of Nuclear Medicine*, **46**(3), pp. 526–531. ISSN 0161-5505.

[28] Bequé, D., J. Nuyts, G. Bormans, P. Suetens, and P. Dupont (2003). Characterization of pinhole SPECT acquisition geometry. *IEEE transactions on medical imaging*, **22**(5), pp. 599–612. ISSN 0278-0062. doi:10.1109/TMI.2003.812258.

[29] Booij, J., K. de Bruin, M. M. de Win, C. Lavini, G. J. den Heeten, and J. B. Habraken (2003). Imaging of striatal dopamine transporters in rat brain with single pinhole SPECT and co-aligned MRI is highly reproducible. *Nuclear Medicine and Biology*, **30**(6), pp. 643–649. ISSN 09698051. doi:10.1016/S0969-8051(03)00046-5.

[30] Brzymialkiewicz, C. N., M. P. Tornai, R. L. McKinley, and J. E. Bowsher (2005). Evaluation of fully 3-D emission mammotomography with a compact cadmium zinc telluride detector. *IEEE transactions on medical imaging*, **24**(7), pp. 868–877. ISSN 0278-0062. doi:10.1109/TMI.2005.852501.

[31] Cai, L., G. Fu, J. W. Tan, and L. J. Meng (2010). A very-high resolution SPECT system based on the energy-resolved photon counting CdTe detectors. *IEEE Nuclear Science Symposium Conference Record*, pp. 2788–2792. ISSN 10957863. doi:10.1109/NSSMIC.2010.5874300.

[32] Cao, Z., G. Bal, R. Accorsi, and P. D. Acton (2005). Optimal number of pinholes in multi-pinhole SPECT for mouse brain imaging–a simulation study. *Physics in medicine and biology*, **50**(19), pp. 4609–4624. ISSN 0031-9155. doi:10.1088/0031-9155/50/19/013.

[33] Caucci, L. and H. H. Barrett (2012). Objective assessment of image quality. V. Photon-counting detectors and list-mode data. *Journal of the Optical Society of America. A, Optics, image science, and vision*, **29**(6), pp. 1003–16. ISSN 1520-8532.

[34] Caucci, L., L. R. Furenlid, and H. H. Barrett (2009). Maximum Likelihood Event Estimation and List-mode Image Reconstruction on GPU Hardware. *IEEE Nuclear Science Symposium conference record. Nuclear Science Symposium*, **2009**(1997), p. 4072. ISSN 1095-7863. doi:10.1109/NSSMIC.2009.5402392.

[35] Caucci, L., M. A. Kupinski, M. Freed, L. R. Furenlid, D. W. Wilson, and H. H. Barrett (2008). Adaptive SPECT for tumor necrosis detection. *2008 IEEE Nuclear Science Symposium Conference Record*, pp. 5548–5551. doi:10.1109/NSSMIC.2008.4774505.

[36] Chaix, C., S. Kovalsky, M. Kosmider, H. H. Barrett, and L. R. Furenlid (2013). Integration of AdaptiSPECT: a small-animal adaptive SPECT imaging system. *Proceedings of SPIE*, **8853**, pp. 88530A–88530A–11. doi:10.1117/12.2029768.

[37] Chaix, C., S. Kovalsky, M. A. Kupinski, H. H. Barrett, and L. R. Furenlid (2014). Fabrication of the pinhole aperture for AdaptiSPECT. *Proceedings of SPIE*, **9214**, pp. 921408–921408–9. doi:10.1117/12.2065907.

[38] Chaix, C., J. W. Moore, R. V. Holen, H. H. Barrett, and L. R. Furenlid (2012). The AdaptiSPECT Imaging Aperture. *IEEE Nuclear Science Symposuim & Medical Imaging Conference*, pp. 3564–3567.

[39] Chen, J. (1995). *Modular gamma cameras: improvements in scatter rejection, and characterization and initial clinical application.* Phd dissertation, The University of Arizona. doi:10.16953/deusbed.74839.

[40] Chen, J. C. (1997). Scatter rejection in modular gamma cameras for use in dynamic 3D brain imaging system. *Computerized Medical Imaging and Graphics*, **21**(5), pp. 283–291.

[41] Chen, J. C. and H. H. Barrett (1994). Likelihood Window , Energy Window

, and Bayesian Window for Scatter Rejection in Gamma Cameras. *IEEE*, pp. 1414–1416.

[42] Chen, Y.-C. (2006). *System Calibration and Image Reconstruction for a new Small-Animal SPECT System*. Ph.D. thesis, The University of Arizona.

[43] Chen, Y.-C., L. R. Furenlid, D. W. Wilson, and H. H. Barrett (2005). Calibration of Scintillation Cameras and Pinhole SPECT Imaging Systems. In Kupinski, M. A. and H. H. Barrett (eds.) *Small-Animal SPECT Imaging*, chapter 12, pp. 195–201. Springer US.

[44] Clarkson, B. E., M. A. Kupinski, H. H. Barrett, and L. Furenlid (2008). A Task-Based Approach to Adaptive and Multimodality Imaging. *Proceedings of the IEEE*, **96**(3), pp. 500–511.

[45] Clarkson, E. (2012). Asymptotic ideal observers and surrogate figures of merit for signal detection with list-mode data. *Journal of the Optical Society of America. A, Optics, image science, and vision*, **29**(10), pp. 2204–16. ISSN 1520-8532.

[46] Clarkson, E. and H. Barrett (1997). A bound on null functions for digital imaging systems with positivity constraints. *Optics letters*, **22**(11), pp. 814–5. ISSN 0146-9592.

[47] Clarkson, E. and F. Shen (2010). Fisher information and surrogate figures of merit for the task-based assessment of image quality. *Journal of the Optical Society of America. A, Optics, image science, and vision*, **27**(10), pp. 2313–26. ISSN 1520-8532.

[48] Constantinesco, A., P. Choquet, L. Monassier, V. Israel-Jost, and L. Mertz (2005). Assessment of left ventricular perfusion, volumes, and motion in mice using pinhole gated SPECT. *Journal of nuclear medicine : official publication, Society of Nuclear Medicine*, **46**(6), pp. 1005–1011. ISSN 0161-5505.

[49] de Hevesy, G. (1923). The absorption and translocation of lead by plants. *Biochem. J*, **17**, p. 439.

[50] Defrise, M., C. Vanhove, and J. Nuyts (2008). Perturbative refinement of the geometric calibration in pinhole SPECT. *IEEE transactions on medical imaging*, **27**(2), pp. 204–14. ISSN 0278-0062. doi:10.1109/TMI.2007.904687.

[51] Del Guerra, A. and N. Belcari (2007). State-of-the-art of PET, SPECT and CT for small animal imaging. *Nuclear Instruments and Methods in Physics Research Section A: Accelerators, Spectrometers, Detectors and Associated Equipment*, **583**(1), pp. 119–124. ISSN 01689002. doi:10.1016/j.nima.2007.08.187.

[52] Deleye, S., R. Van Holen, J. Verhaeghe, S. Vandenberghe, S. Stroobants, and S. Staelens (2013). Performance evaluation of small-animal multipinhole μSPECT scanners for mouse imaging. *European journal of nuclear medicine and molecular imaging*, **40**(5), pp. 744–58. ISSN 1619-7089. doi:10.1007/s00259-012-2326-2.

[53] Deprez, K., L. R. V. Pato, S. Vandenberghe, and R. Van Holen (2013). Characterization of a SPECT pinhole collimator for optimal detector usage (the lofthole). *Physics in medicine and biology*, **58**(4), pp. 859–85. ISSN 1361-6560. doi:10.1088/0031-9155/58/4/859.

[54] Deprez, K., S. Vandenberghe, K. Van Audenhaege, J. Van Vaerenbergh, and R. Van Holen (2013). Rapid additive manufacturing of MR compatible multipinhole collimators with selective laser melting of tungsten powder. *Medical physics*, **40**(1), p. 012501. ISSN 0094-2405. doi:10.1118/1.4769122.

[55] Deutscher, S. L., S. D. Figueroa, and S. R. Kumar (2009). Tumor targeting and SPECT imaging properties of an (111)In-labeled galectin-3 binding peptide in prostate carcinoma. *Nuclear medicine and biology*, **36**(2), pp. 137–46. ISSN 0969-8051. doi:10.1016/j.nucmedbio.2008.10.015.

[56] DiFilippo, F. P. and S. Patel (2009). Strategies to reduce artifacts and improve accuracy in multiplexed multi-pinhole small animal SPECT. In *IEEE Nuclear Science Symposium Conference Record*, pp. 3151–3154. ISBN 9781424439621. ISSN 10957863. doi:10.1109/NSSMIC.2009.5401689.

[57] Durko, H. L. (2014). *Anamorphic Preclinical SPECT Imaging with High-Resolution Silicon Double-Sided Strip Detectors*. Ph.D. thesis, The University of Arizona.

[58] Durko, H. L., H. H. Barrett, and L. R. Furenlid (2014). High-resolution anamorphic SPECT imaging. *IEEE Transactions on Nuclear Science*, **61**(3), pp. 1126–1135. ISSN 00189499. doi:10.1109/TNS.2014.2304853.

[59] Ficaro, E. P., J. A. Fessler, P. D. Shreve, J. N. Kritzman, P. A. Rose, and J. R. Corbett (1996). Simultaneous transmission/emission myocardial perfusion tomography. Diagnostic accuracy of attenuation-corrected 99mTc-sestamibi single-photon emission computed tomography. *Circulation*, **93**(3), pp. 463–73. ISSN 0009-7322.

[60] Fisher, R. A. (1925). Theory of statistical estimation. In *Mathematical Proceedings of the Cambridge Philosophical Society*, volume 22, pp. 700–725. Cambridge Univ Press.

[61] Floyd, C. E., R. J. Jaszczak, K. L. Greer, and R. E. Coleman (1986). Inverse Monte Carlo as a unified reconstruction algorithm for ECT. *Journal of nuclear medicine : official publication, Society of Nuclear Medicine*, **27**(10), pp. 1577–1585. ISSN 0018-9499. doi:10.1109/TNS.1985.4336940.

[62] Freed, M., M. A. Kupinski, L. R. Furenlid, D. W. Wilson, and H. H. Barrett (2008). A prototype instrument for single pinhole small animal adaptive SPECT imaging. *Medical physics*, **35**(5), pp. 1912–1925. doi: 10.1118/1.2896072.A.

[63] Furenlid, L. R., Y.-C. Chen, and K. Hyunki (2005). SPECT imager design and data-acquisition systems. In *Small-Animal SPECT Imaging*, pp. 115–138. Springer US.

[64] Furenlid, L. R., J. Y. Hesterman, and H. H. Barrett (2005). Real-time Data Acquisition and Maximum- Likelihood Estimation for Gamma Cameras. *IEEE*, pp. 498–501. doi:10.1109/RTC.2005.1547506.

[65] Furenlid, L. R., J. W. Moore, M. Freed, M. A. Kupinski, and E. Clarkson (2008). Adaptive Small-Animal SPECT/CT. *5th IEEE Int. Symp. Biomed. Imaging: From Nano to Macro*, pp. 1407–1410.

[66] Furenlid, L. R., D. W. Wilson, Y.-C. Chen, H. Kim, P. J. Pietraski, M. J. Crawford, and H. H. Barrett (2004). FastSPECT II: A Second-Generation High-Resolution Dynamic SPECT Imager. *IEEE transactions on nuclear science*, **51**(3), pp. 631–635. ISSN 0018-9499. doi:10.1109/TNS.2004.830975.

[67] Gambini, J. P., P. Cabral, O. Alonso, E. Savio, S. D. Figueroa, X. Zhang, L. Ma, S. L. Deutscher, and T. P. Quinn (2011). Evaluation of 99mTc-glucarate as a breast cancer imaging agent in a xenograft animal model. *Nuclear medicine and biology*, **38**(2), pp. 255–260. ISSN 1872-9614 (Electronic). doi:10.1016/j.nucmedbio.2010.08.002.

[68] Garibaldi, F., R. Accorsi, M. Cinti, E. Cisbani, S. Colilli, F. Cusanno, G. D. Vincentis, A. Fortuna, R. Fratoni, B. Girolami, F. Ghio, F. Giuliani, M. Gricia, R. Lanza, A. Loizzo, S. Loizzo, M. Lucentini, S. Majewski, F. Santavenere, R. Pani, R. Pellegrini, A. Signore, F. Scopinaro, and P. Veneroni (2005). Small animal imaging by single photon emission using pinhole and coded aperture collimation. *IEEE Transactions on Nuclear Science*, **52**(3). ISSN 0018-9499. doi:10.1109/TNS.2005.851428.

[69] Golestani, R., C. Wu, R. a. Tio, C. J. Zeebregts, A. D. Petrov, F. J. Beekman, R. A. Dierckx, H. H. Boersma, and R. H. Slart (2010). Small-animal SPECT

and SPECT/CT: application in cardiovascular research. *European journal of nuclear medicine and molecular imaging*, **37**(9), pp. 1766–77. ISSN 1619-7089. doi:10.1007/s00259-009-1321-8.

[70] Goorden, M. C. and F. J. Beekman (2010). High-resolution tomography of positron emitters with clustered pinhole SPECT. *Physics in medicine and biology*, **55**(5), pp. 1265–1277. ISSN 0031-9155. doi:10.1088/0031-9155/55/5/001.

[71] Gray, R. M. and A. Macovski (1976). Maximum a Posteriori Estimation of Position in Scintillation Cameras. *IEEE Transactions on Nuclear Science*, **23**(1), pp. 849–852.

[72] Havelin, R. J., B. W. Miller, H. H. Barrett, L. R. Furenlid, J. M. Murphy, R. M. Dwyer, and M. J. Foley (2013). Design and performance of a small-animal imaging system using synthetic collimation. *Physics in medicine and biology*, **58**(10), pp. 3397–412. ISSN 1361-6560. doi:10.1088/0031-9155/58/10/3397.

[73] He, Z., G. F. Knoll, D. K. Wehe, and J. Miyamoto (1997). Position-sensitive single carrier CdZnTe detectors. *Nuclear Instruments and Methods in Physics Research A*, **388**, pp. 180–185. ISSN 01689002 (ISSN). doi:10.1016/S0168-9002(97)00318-5.

[74] Helstrom, C. W. (1967). Image Restoration by the Method of Least Squares. *Journal of the Optical Society of America*, **57**(3), p. 297. ISSN 0030-3941. doi:10.1364/JOSA.57.000297.

[75] Hesterman, J. Y. (2007). *The Multi-Module Multi-Resolution SPECT SYSTEM : a tool for variable pinhole imaging*. Ph.D. thesis, The University of Arizona.

[76] Hesterman, J. Y., L. Caucci, M. A. Kupinski, H. H. Barrett, and L. R. Furenlid (2010). Maximum-Likelihood Estimation With a Contracting-Grid Search

Algorithm. *IEEE transactions on nuclear science*, **57**(3), pp. 1077–1084. ISSN 0018-9499. doi:10.1109/TNS.2010.2045898.

[77] Hesterman, J. Y., M. A. Kupinski, E. Clarkson, and H. H. Barrett (2007). Hardware assessment using the multi-module, multi-resolution system (M3R): A signal-detection study. *Medical physics*, **34**(7), pp. 3034–3044.

[78] Hesterman, J. Y., M. A. Kupinski, L. R. Furenlid, D. W. Wilson, and H. H. Barrett (2007). The multi-module, multi-resolution system (M3R): A novel small-animal SPECT system. *Medical Physics*, **34**(3), pp. 987–993.

[79] Holl, I., E. Lorenz, and G. Mageras (1988). *A measurement of the light yield of common inorganic scintillators*, volume 35:1.

[80] Holleman, A. and E. Wiberg (1995). *Inorganic Chemistry*. Berlin, New York, 34 edition.

[81] Hunter, W. C. J. (2007). *Modeling Stochastic Processes in Gamma-Ray Imaging Detectors and Evaluation of a Multi-Anode PMT Scintillation Camera for Use with Maximum-Likelihood Estimation Methods*. Ph.D. thesis, University of Arizona.

[82] Hunter, W. C. J., H. H. Barrett, and L. R. Furenlid (2009). Calibration Method for ML Estimation of 3D Interaction Position in a Thick Gamma-Ray Detector. *IEEE transactions on nuclear science*, **56**(1), pp. 189–196. ISSN 0018-9499. doi:10.1109/TNS.2008.2010704.

[83] Igus Inc, G. (2014). website: http://www.igus.com/.

[84] Jaszczak, R. J., J. Li, H. Wang, and M. R. Zalutsky (1994). Pinhole collimation for ultra-high-resolution, small-field-of-view SPECT. *Physics in medicine and biology*, **39**, pp. 425–437.

[85] Kastis, G., H. Barber, H. Barrett, H. Gifford, I. Pang, D. Patton, J. Sain, G. Stevenson, and D. Wilson (1998). High resolution SPECT imager for three-

dimensional imaging of small animals. *Journal of Nuclear Medicine*, **39**(5), pp. 9–9.

[86] Kastis, G. A., L. R. Furenlid, D. W. Wilson, T. E. Peterson, H. B. Barber, and H. H. Barrett (2004). Compact CT / SPECT Small-Animal Imaging System. *IEEE transactions on nuclear science*, **51**(1), pp. 63–67.

[87] Keyes, W. I. (1975). The fan-beam gamma camera. *Physics in medicine and biology*, **20**(3), p. 489.

[88] Kiessling, F. and B. J. Pichler (2011). *Small Animal Imaging*. ISBN 9783642129445.

[89] Kim, H., L. R. Furenlid, M. J. Crawford, D. W. Wilson, H. B. Barber, T. E. Peterson, W. C. J. Hunter, Z. Liu, J. M. Woolfenden, and H. H. Barrett (2006). SemiSPECT: A small-animal single-photon emission computed tomography (SPECT) imager based on eight cadmium zinc telluride (CZT) detector arrays. *Medical Physics*, **33**(2), p. 465. ISSN 00942405. doi:10.1118/1.2164070.

[90] Lazaro, D., Z. El Bitar, V. Breton, D. Hill, and I. Buvat (2005). Fully 3D Monte Carlo reconstruction in SPECT: a feasibility study. *Physics in medicine and biology*, **50**(16), pp. 3739–54. ISSN 0031-9155. doi:10.1088/0031-9155/50/16/006.

[91] Lecoq, P., A. Annenkov, A. Gektin, M. Korzhik, and C. Pedrini (2006). *Inorganic scintillators for detector systems: physical principles and crystal engineering*. Springer Science.

[92] Lehovich, A. (2005). *List-mode SPECT reconstruction using empirical likelihood*. Ph.D. thesis, The University of Arizona.

[93] Li, J., R. J. Jaszczak, H. Wang, K. L. Greer, and R. E. Coleman (1993). Determination of both mechanical and electronic shifts in cone beam SPECT. *Physics in Medicine and Biology*, **38**(6), pp. 743–54. ISSN 0031-9155.

[94] Li, N. and L.-J. Meng (2011). Adaptive Angular Sampling for SPECT Imaging. *IEEE Transactions on Nuclear Science*, **58**(5), pp. 2205–2218. ISSN 0018-9499. doi:10.1109/TNS.2011.2164935.

[95] Lin, J. (2013). On artifact-free projection overlaps in multi-pinhole tomographic imaging. *IEEE Transactions on Medical Imaging*, **32**(12), pp. 2215–2229. ISSN 02780062. doi:10.1109/TMI.2013.2277588.

[96] Lin, J. and S. R. Meikle (2011). SPECT using asymmetric pinholes with truncated projections. *Physics in medicine and biology*, **56**(13), pp. 4103–4118. ISSN 0031-9155. doi:10.1088/0031-9155/56/13/023.

[97] Liu, Z., M. Zhao, X. Zhu, L. R. Furenlid, Y.-C. Chen, and H. H. Barrett (2007). In vivo dynamic imaging of myocardial cell death using 99mTc-labeled C2A domain of synaptotagmin I in a rat model of ischemia and reperfusion. *Nuclear medicine and biology*, **34**(8), pp. 907–15. ISSN 0969-8051. doi:10.1016/j.nucmedbio.2007.07.013.

[98] Mahmood, S., K. Erlandsson, I. Cullum, and B. Hutton (2011). Experimental results from a prototype slit-slat collimator with mixed multiplexed and non-multiplexed data. *Physics in medicine and biology*, **56**(14), pp. 4311–31. ISSN 1361-6560. doi:10.1088/0031-9155/56/14/007.

[99] Mahmood, S. T., K. Erlandsson, I. Cullum, and B. F. Hutton (2010). The potential for mixed multiplexed and non-multiplexed data to improve the reconstruction quality of a multi-slit-slat collimator SPECT system. *Physics in medicine and biology*, **55**(8), pp. 2247–68. ISSN 1361-6560. doi:10.1088/0031-9155/55/8/009.

[100] Matherson, K. J., H. B. Barber, H. H. Barrett, J. D. Eskin, E. L. Dereniak, D. G. Marks, J. M. Woolfenden, E. T. Young, and F. L. Augustine (1998). Progress in the development of large-area modular 64 x 64 CdZnTe imaging

arrays for nuclear medicine. *Ieee Transactions on Nuclear Science*, **45**(3), pp. 354–358. ISSN 00189499 (ISSN). doi:Doi10.1109/23.682407.

[101] McDonald, B. S. (2010). *Development of the SiliSPECT small-animal imager*. Ph.D. thesis.

[102] Meikle, S. R., P. Kench, M. Kassiou, and R. B. Banati (2005). Small animal SPECT and its place in the matrix of molecular imaging technologies. *Physics in medicine and biology*, **50**(22), pp. R45–61. ISSN 0031-9155. doi:10.1088/0031-9155/50/22/R01.

[103] Meikle, S. R., P. Kench, A. G. Weisenberger, R. Wojcik, M. F. Smith, S. Majewski, S. Eberl, R. R. Fulton, A. B. Rosenfeld, and M. J. Fulham (2002). A prototype coded aperture detector for small animal SPECT. *IEEE Transactions on Nuclear Science*, **49 I**(5), pp. 2167–2171. ISSN 00189499. doi:10.1109/TNS.2002.803802.

[104] Meikle, S. R., P. L. Kench, and J. Lin (2014). Design Considerations of Small-Animal SPECT Cameras. In *Molecular Imaging of Small Animals*, pp. 135–162. Springer New York.

[105] Meikle, S. R., R. Wojcik, A. G. Weisenberger, M. F. Smith, S. Majewski, P. Kench, S. Eberl, R. R. Fulton, M. Lerch, and A. B. Rosenfeld (2003). CoALA-SPECT : A Coded Aperture Laboratory Animal SPECT System for Pre Clinical Imaging. *IEEE*, pp. 1061–1065.

[106] Meng, L. J. (2006). An intensified EMCCD camera for low energy gamma ray imaging applications. *IEEE Transactions on Nuclear Science*, **53**(4), pp. 2376–2384. ISSN 00189499. doi:10.1109/TNS.2006.878574.

[107] Meng, L. J. and N. H. Clinthorne (2004). A modified uniform Cramer-Rao bound for multiple pinhole aperture design. *IEEE Transactions on Medical Imaging*, **23**(7), pp. 896–902. ISSN 02780062. doi:10.1109/TMI.2004.828356.

[108] Meng, L. J., G. Fu, E. J. Roy, B. Suppe, and C. T. Chen (2009). An ultra-high resolution SPECT system for I-125 mouse brain imaging studies. *Nuclear Instruments and Methods in Physics Research, Section A: Accelerators, Spectrometers, Detectors and Associated Equipment*, **600**, pp. 498–505. ISSN 01689002. doi:10.1016/j.nima.2008.11.149.

[109] Metzler, S. D., J. E. Bowsher, K. L. Greer, and R. J. Jaszczak (2002). Analytic determination of the pinhole collimator's point-spread function and RMS resolution with penetration. *IEEE transactions on medical imaging*, **21**(8), pp. 878–887. ISSN 0278-0062.

[110] Metzler, S. D., J. E. Bowsher, M. F. Smith, and R. J. Jaszczak (2001). Analytic determination of pinhole collimator sensitivity with penetration. *IEEE transactions on medical imaging*, **20**(8), pp. 730–41. ISSN 0278-0062. doi:10.1109/42.938241.

[111] Metzler, S. D., K. L. Greer, and R. J. Jaszczak (2005). Determination of mechanical and electronic shifts for pinhole SPECT using a single point source. *IEEE transactions on medical imaging*, **24**(3), pp. 361–70. ISSN 0278-0062. doi:10.1109/TMI.2004.842456.

[112] Metzler, S. D. and R. J. Jaszczak (2006). Simultaneous multi-head calibration for pinhole SPECT. doi:10.1109/TNS.2005.862978.

[113] Metzler, S. D., R. J. Jaszczak, N. H. Patil, S. Vemulapalli, G. Akabani, and B. B. Chin (2005). Molecular imaging of small animals with a triple-head SPECT system using pinhole collimation. *IEEE transactions on medical imaging*, **24**(7), pp. 853–62. ISSN 0278-0062. doi:10.1109/TMI.2005.848357.

[114] Miller, B. W. (2012). *High-resolution gamma-ray imaging with columnar scintillators and CCD/CMOS sensors, and FastSPECT III: A third-generation stationary SPECT imager*. Ph.D. thesis, University of Arizona.

[115] Miller, B. W., H. B. Barber, H. H. Barrett, L. Chen, and S. J. Taylor (2007). Photon-counting gamma camera based on columnar CsI(Tl) optically coupled to a back-illuminated CCD. *Proceedings of SPIE*, **6510**, pp. 1–7. ISSN 0277-786X. doi:10.1117/12.710109.

[116] Miller, B. W., H. B. Barber, L. R. Furenlid, S. K. Moore, and H. H. Barrett (2009). Progress in BazookaSPECT. *Proceedings of SPIE*, **7450**(7450C). ISSN 0277-786X. doi:10.1117/12.843742.

[117] Miller, B. W., J. W. Moore, H. H. Barrett, T. Fryé, and S. Adler (2012). 3D printing in x-ray and Gamma-ray Imaging: A novel method for fabricating high-density imaging apertures. *Nuclear instruments & methods in physics research. Section A, Accelerators, spectrometers, detectors and associated equipment*, **659**(1), pp. 262–268. doi:10.1016/j.nima.2011.08.051.3D.

[118] Miller, B. W., R. Van Holen, H. H. Barrett, and L. R. Furenlid (2012). A System Calibration and Fast Iterative Reconstruction Method for Next-Generation SPECT Imagers. *IEEE Transactions on Nuclear Science*, **59**(5), pp. 1990–1996. ISSN 0018-9499. doi:10.1109/TNS.2012.2198243.

[119] Milster, T. D., J. N. Aarsvold, H. H. Barrett, A. L. Landesman, L. S. Mar, D. D. Patton, T. J. Roney, R. K. Rowe, and R. H. Seacatiii (1990). A Full-Field Modular Gamma Camera. *Journal of Nuclear Medicine*, **31**(4), pp. 632–639.

[120] Milster, T. D., L. A. Selberg, H. H. Barrett, R. L. Easton, G. R. Rossi, J. Arendt, and R. G. Simpson (1984). A modular scintillation camera. *IEEE transactions on nuclear science*, (1), pp. 578–580.

[121] Milster, T. D., L. A. Selberg, H. H. Barrett, A. L. Landesman, and S. R. H (1985). Digital position estimation for the modular scintillation camera. *IEEE transactions on nuclear science*, **NS-32**(1), pp. 748–752.

[122] Mitchell, G. S., S. Sinha, J. R. Stickel, S. L. Bowen, L. J. Cirignano, P. Dokhale, H. Kim, K. S. Shah, and S. R. Cherry (2008). CdTe strip de-

tector characterization for high resolution small animal PET. *IEEE Transactions on Nuclear Science*, **55**(3), pp. 870–876. ISSN 00189499. doi: 10.1109/TNS.2008.922800.

[123] Mok, G. S. P., B. M. W. Tsui, and F. J. Beekman (2011). The effects of object activity distribution on multiplexing multi-pinhole SPECT. *Physics in medicine and biology*, **56**(8), pp. 2635–50. ISSN 1361-6560. doi:10.1088/0031-9155/56/8/019.

[124] Mok, G. S. P., J. Yu, Y. Du, Y. Wang, and B. M. W. Tsui (2012). Evaluation of a multi-pinhole collimator for imaging small animals with different sizes. *Molecular Imaging and Biology*, **14**(1), pp. 60–69. ISSN 15361632. doi:10.1007/s11307-011-0472-8.

[125] Moore, J. W. (2011). *Adaptive X-ray Computed Tomography*. Ph.D. thesis, The University of Arizona.

[126] Moore, J. W., L. R. Furenlid, and H. H. Barrett (2008). Instrumentation design for adaptive SPECT/CT. In *IEEE Nuclear Science Symposium Conference Record*, pp. 5585–5587. ISBN 9781424427154. ISSN 10957863. doi: 10.1109/NSSMIC.2008.4774512.

[127] Moore, S. C., M.-A. Park, D. Xia, and S. D. Metzler (2013). Dual-resolution microSPECT mouse imaging using a triple-head SPECT system. In *2013 IEEE Nuclear Science Symposium and Medical Imaging Conference (2013 NSS/MIC)*, pp. 1–5. ISBN 978-1-4799-0534-8. doi:10.1109/NSSMIC.2013.6829404.

[128] Moore, S. K. (2011). *ModPET : Novel Applications of Scintillation Cameras to Preclinical PET*. Ph.D. thesis, The University of Arizona.

[129] Myers, K. J., J. P. Rolland, H. H. Barrett, and R. F. Wagner (1990). Aperture optimization for emission imaging: effect of a spatially varying background.

Journal of the Optical Society of America. A, Optics and image science, **7**(7), pp. 1279–93. ISSN 0740-3232.

[130] Orlov, S. S. (1975). Theory of three-dimensional reconstruction. II. The recovery operator.

[131] Paix, D. (1967). Pinhole imaging of gamma rays. *Physics in medicine and biology*, **12**(4), pp. 489–500.

[132] Parra, L. and H. H. Barrett (1998). List-mode likelihood: EM algorithm and image quality estimation demonstrated on 2-D PET. *IEEE transactions on medical imaging*, **17**(2), pp. 228–35. ISSN 0278-0062. doi:10.1109/42.700734.

[133] Pato, L. d. R. V., S. Vandenberghe, K. V. Audenhaege, and R. V. Holen (2014). Design and Simulation of a Stationary SPECT Imaging System Based on Axially Varying Tilted Parallel-hole Collimation. *IEEE Nuclear Science Symposium and Medical Imaging Conference, Abstracts. IEEE.*

[134] Peterson, T. E. and L. R. Furenlid (2011). SPECT detectors: the Anger Camera and beyond. *Physics in medicine and biology*, **56**(17), pp. R145–82. ISSN 1361-6560. doi:10.1088/0031-9155/56/17/R01.

[135] Radiation Sensors LLC, Alabama (2015). web-site http://www.radsens.com.

[136] Rizo, P., P. Grangeat, and R. Guillemaud (1994). Geometric calibration method for multiple-head cone-beam SPECT system. *IEEE Transactions on Nuclear Science*, **41**(6), pp. 2748–2757. ISSN 0018-9499. doi: 10.1109/23.340643.

[137] Rodnyi, P. A. (1997). *Physical processes in inorganic scintillators*. CRC press.

[138] Rogulski, M. M., H. B. Barber, H. H. Barrett, R. L. Shoemaker, and J. M. Woolfenden (1993). Ultra-high-resolution brain SPECT imaging: simulation results. *IEEE Transactions on Nuclear Science*, **40**(4), pp. 1123–1129. ISSN 00189499. doi:10.1109/23.256722.

[139] Sain, J. D. and H. H. Barrett (2003). Performance evaluation of a modular gamma camera using a detectability index. *Journal of nuclear medicine : official publication, Society of Nuclear Medicine*, **44**(1), pp. 58–66. ISSN 0161-5505.

[140] Salcin, E. (2015). *Fisher information in x-ray / gamma-ray imaging*. Phd, University of Arizona.

[141] Schramm, N., J. Hoppin, C. Lackas, B. Gershman, J. Norenberg, and M. de Jong (2007). Improving resolution, sensitivity and applications for the NanoSPECT/CT: A high-performance SPECT/CT imager for small-animal research. *J NUCL MED MEETING ABSTRACTS*, **48**(MeetingAbstracts_2), pp. 436P–c.

[142] Schramm, N. U., G. Ebel, U. Engeland, T. Schurrat, M. Béhé, and T. M. Behr (2003). High-Resolution SPECT Using Multipinhole Collimation. *IEEE Transactions on Nuclear Science*, **50**(3), pp. 315–320.

[143] Schramm, N. U., J. W. Hoppin, C. Lackas, F. Forrer, R. Valkema, and M. D. Jong (2006). The NanoSPECT: A high-sensitivity multi-pinhole SPECT system with submillimeter (nanoliter) spatial resolution for imaging small rodents. *Journal of Nuclear Medicine*, **47**, p. 233.

[144] Shepp, L. and Y. Vardi (1982). Maximum Likelihood Reconstruction for Emission Tomography. *IEEE Transactions on Medical Imaging*, **MI-1**(2), pp. 113–122. ISSN 0278-0062. doi:10.1109/TMI.1982.4307558.

[145] Shokouhi, S., M. a. Fritz, B. S. McDonald, M. D. W. Wilson, S. D. Metzler, and T. E. Peterson (2007). Design of a multi-pinhole collimator in a dual-headed, stationary, small-animal SPECT. *IEEE Nuclear Science Symposium Conference Record*, **4**, pp. 2399–2402. ISSN 10957863. doi:10.1109/NSSMIC.2006.354396.

[146] Shokouhi, S., S. D. Metzler, D. W. Wilson, and T. E. Peterson (2009). Multi-pinhole collimator design for small-object imaging with SiliSPECT: a high-resolution SPECT. *Physics in medicine and biology*, **54**(2), pp. 207–25. ISSN 0031-9155. doi:10.1088/0031-9155/54/2/003.

[147] Shokouhi, S., D. W. Wilson, S. D. Metzler, and T. E. Peterson (2010). Evaluation of image reconstruction for mouse brain imaging with synthetic collimation from highly multiplexed SiliSPECT projections. *Physics in medicine and biology*, **55**(17), pp. 5151–5168. ISSN 0031-9155. doi:10.1088/0031-9155/55/17/017.

[148] Siddon, R. L. (1985). Fast calculation of the exact radiological path for a three-dimensional CT array. *Medical physics*.

[149] Smith, M., R. Jaszczak, and H. Wang (1997). Pinhole aperture design for 131I tumor imaging. *IEEE Transactions on Nuclear Science*, **44**(3), pp. 1154–1160. ISSN 00189499. doi:10.1109/23.596980.

[150] Smith, M. F. and R. J. Jaszczak (1998). An analytic model of pinhole aperture penetration for 3D pinhole SPECT image reconstruction. *Physics in medicine and biology*, **43**(4), pp. 761–775. ISSN 0031-9155.

[151] Smith, W. E., R. G. Paxman, and H. H. Barrett (1985). Application of simulated annealing to coded-aperture design and tomographic reconstruction. *IEEE*, pp. 758–761.

[152] Tanaka, E. and T. Iinuma (1976). Image processing for coded aperture imaging and an attempt at rotating slit imaging. *International Journal of Nuclear Medicine and Biology*, **3**(3), pp. 193–196.

[153] Tsui, B. M., E. C. Frey, K. J. LaCroix, D. S. Lalush, W. H. McCartney, M. a. King, and G. T. Gullberg (1998). Quantitative myocardial perfusion SPECT. *Journal of nuclear cardiology : official publication of the American Society of Nuclear Cardiology*, **5**(5), pp. 507–22. ISSN 1071-3581.

[154] Tuy, H. K. (1983). An Inversion Formula for Cone-Beam Reconstruction. doi:10.1137/0143035.

[155] Van Audenhaege, K., R. Van Holen, S. Vandenberghe, C. Vanhove, S. D. Metzler, and S. C. Moore (2015). Review of SPECT collimator selection, optimization, and fabrication for clinical and preclinical imaging. *Medical Physics*, **42**(8), pp. 4796–4813. ISSN 0094-2405. doi:10.1118/1.4927061.

[156] Van Audenhaege, K., C. Vanhove, S. Vandenberghe, and R. Van Holen (2014). The evaluation of data completeness and image quality in multiplexing multi-pinhole SPECT. *IEEE transactions on medical imaging*, **0062**(c), pp. 1–13. ISSN 1558-254X. doi:10.1109/TMI.2014.2361051.

[157] van der Have, F., B. Vastenhouw, R. M. Ramakers, W. Branderhorst, J. O. Krah, C. Ji, S. G. Staelens, and F. J. Beekman (2009). U-SPECT-II: An Ultra-High-Resolution Device for Molecular Small-Animal Imaging. *Journal of nuclear medicine : official publication, Society of Nuclear Medicine*, **50**, pp. 599–605. ISSN 0161-5505. doi:10.2967/jnumed.108.056606.

[158] van der Have, F., B. Vastenhouw, M. Rentmeester, and F. J. Beekman (2008). System calibration and statistical image reconstruction for ultra-high resolution stationary pinhole SPECT. *IEEE transactions on medical imaging*, **27**(7), pp. 960–71. ISSN 1558-254X. doi:10.1109/TMI.2008.924644.

[159] Van Holen, R., J. W. Moore, E. W. Clarkson, L. R. Furenlid, and H. H. Barrett (2010). Design and Validation of an Adaptive SPECT System : AdaptiSPECT inhole distance as can see 1 or 5. In *IEEE Nuclear Science Symposuim & Medical Imaging Conference*, pp. 2539–2544. ISBN 9781424491056.

[160] Vanhove, C., M. Defrise, T. Lahoutte, and A. Bossuyt (2008). Three-pinhole collimator to improve axial spatial resolution and sensitivity in pinhole SPECT. *European Journal of Nuclear Medicine and Molecular Imaging*, **35**(2), pp. 407–415. ISSN 16197070. doi:10.1007/s00259-007-0579-y.

[161] Verger, L., M. C. Gentet, L. Gerfault, R. Guillemaud, C. Mestais, O. Monnet, G. Montemont, G. Petroz, J. P. Rostaing, and J. Rustique (2004). Performance and perspectives of a CdZnTe-based gamma camera for medical imaging. *IEEE Transactions on Nuclear Science*, **51**(6 I), pp. 3111–3117. ISSN 0018-9499. doi:10.1109/TNS.2004.839070.

[162] Vunckx, K., D. Beque, M. Defrise, and J. Nuyts (2008). Single and multipinhole collimator design evaluation method for small animal SPECT. *IEEE transactions on medical imaging*, **27**(1), pp. 36–46. ISSN 0278-0062. doi: 10.1109/TMI.2007.902802.

[163] Vunckx, K., J. Nuyts, B. Vanbilloen, M. D. Saint-hubert, D. Vanderghinste, D. Rattat, F. M. Mottaghy, M. Defrise, and S. Member (2009). Optimized Multipinhole Design for Mouse Imaging. *IEEE transactions on nuclear science*, **56**(5), pp. 2696–2705.

[164] Vunckx, K., P. Suetens, and J. Nuyts (2008). Effect of overlapping projections on reconstruction image quality in multipinhole SPECT. *IEEE transactions on medical imaging*, **27**(7), pp. 972–83. ISSN 1558-254X. doi:10.1109/TMI.2008.922700.

[165] Wagner, R. F. and D. G. Brown (2000). Unified SNR analysis of medical imaging systems. *Physics in Medicine and Biology*, **30**(6), pp. 489–518. ISSN 0031-9155. doi:10.1088/0031-9155/30/6/001.

[166] Wang, Y., S. Luo, J. Lin, L. Qiu, W. Cheng, H. Zhai, B. Nan, W. Ye, and Y. Xia (2011). Animal studies of 99mTc-i-PIDP: A new bone imaging agent. *Applied Radiation and Isotopes*, **69**(9), pp. 1169–1175. ISSN 09698043. doi: 10.1016/j.apradiso.2011.03.045.

[167] Wernick, M. N. and J. N. Aarsvold (2004). *Emission tomography: the fundamentals of PET and SPECT*. Academic Press.

[168] Whitaker, M. K., E. Clarkson, and H. H. Barrett (2008). Estimating random signal parameters from noisy images with nuisance parameters: linear and scanning-linear methods. *Optics express*, **16**(11), pp. 8150–8173. ISSN 1094-4087. doi:10.1364/OE.16.008150.

[169] Wiener, N. (1949). *Extrapolation, interpolation, and smoothing of stationary time series: with engineering applications*, volume 47. ISBN 026223002X. doi:10.2307/2280758.

[170] Wilson, D. W., H. H. Barrett, and E. W. Clarkson (2000). Reconstruction of two- and three-dimensional images from synthetic-collimator data. *IEEE transactions on medical imaging*, **19**(5), pp. 412–22. ISSN 0278-0062. doi: 10.1109/42.870252.

[171] Woolfenden, J. M. and Z. Liu (2005). Biomedical Significance of Small-Animal Imaging. In Kupinski, M. A. and H. H. Barrett (eds.) *Small-Animal SPECT Imaging*, chapter 1, pp. 1–8. Springer.

[172] Zeng, G. L. (2008). A skew-slit collimator for small-animal SPECT. *Journal of nuclear medicine technology*, **36**(4), pp. 207–12. ISSN 0091-4916. doi: 10.2967/jnmt.108.055582.

[173] Zeng, G. L., D. Gagnon, C. G. Matthews, J. a. Kolthammer, J. D. Radachy, and W. G. Hawkins (2002). Image reconstruction algorithm for a rotating slat collimator. *Medical physics*, **29**(7), pp. 1406–1412. ISSN 1082-3654. doi: 10.1109/NSSMIC.2001.1009188.